Czech Technical University in Prague

Faculty of Nuclear Sciences and Physical Engineering

Doctoral thesis

Fluid Dynamical Models for Relativistic Nuclear Collisions

Prague, 2022 **Ing. Jakub Cimerman**

Prehlásenie

Prehlasujem, že som svoju dizertačnú prácu vypracoval samostatne a použil som iba podklady (literatúru, projekty, SW atď) uvedené v priloženom zozname.

Nemám závažný dôvod proti použitiu tohoto školského diela v zmysle § 60 Zákona č. 121/2000 Sb., o práve autorskom, o právach súvisiacich s právom autorským a o zmene niektorých zákonov (autorský zákon).

V Prahe dňa ....

Ing. Jakub Cimerman

Bibliografický záznam

Autor:	Ing. Jakub Cimerman, České vysoké učení technické v Praze, Fakulta jaderná a fyzikálně inženýrská, katedra fyziky
Název práce:	Modely dynamiky tekutin pro relativistické jaderné srážky
Studijní program:	Aplikace přírodních věd
Studijní obor:	Jaderné inženýrství
Školitel:	Prof. Dr. Boris Tomášik, České vysoké učení technické v Praze, Fakulta jaderná a fyzikálně inženýrská, katedra fyziky
Školitel specialista:	Iurii Karpenko, Ph.D., České vysoké učení technické v Praze, Fakulta jaderná a fyzikálně inženýrská, katedra fyziky
Akademický rok:	2022/2023
Počet stran:	123
Klíčová slova:	Kvark-gluonové plazma, hydrodynamika, energie programu Beam-energy scan, hybridní model, 3-tekutinová hydrodynamika, anisotropický tok

Bibliographic Entry

Author:	Ing. Jakub Cimerman, Czech Technical University in Prague, Faculty of Nuclear Sciences and Physical Engineering, Department of Physics
Title of Dissertation:	Fluid Dynamical Models for Relativistic Nuclear Collisions
Degree Programme:	Applications of Natural Sciences
Field of Study:	Nuclear Engineering
Supervisor:	Prof. Dr. Boris Tomášik, Czech Technical University in Prague, Faculty of Nuclear Sciences and Physical Engineering, Department of Physics
Supervisor Specialist:	Iurii Karpenko, Ph.D., Czech Technical University in Prague, Faculty of Nuclear Sciences and Physical Engineering, Department of Physics
Academic Year:	2022/2023
Number of Pages:	123
Keywords:	Quark-gluon plasma, hydrodynamics, beam-energy scan energies, hybrid model, three-fluid hydrodynamics, anisotropic flow

Abstrakt

Snaha objaviť kritický bod fázového diagramu kvantovej chromodynamiky si vyžaduje výskum zrážok ťažkých iónov pri energiách od jednotiek po desiatky GeV na nukleónový pár. Avšak simulácie pri takto nízkych energiách sú oveľa komplexnejšie ako v prípade simulácií pri energiách v rádoch stoviek až tisícok GeV. Je to napríklad kvôli dlhšiemu času vzájomného prieniku jadier či konečnej baryónovej hustote v tekutine. Prvá časť tejto práce skúma možnosti použitia hybridného hydrodynamického modelu vyvinutého pre LHC energie na simulácie pri energiách programu Beam Energy Scan (BES) na urýchľovači RHIC. Pokiaľ rozšírime počiatočný stav do troch rozmerov, tento model dokáže efektívne reprodukovať experimentálne dáta. Druhá časť dizertačnej práce opisuje vývoj moderného hybridného modelu, ktorý dokáže zvládnuť všetky výzvy simulácií pri študovanom rozsahu energií. Základ modelu tvorí nová verzia trojtekutinového hydrodynamického modelu. Na transformáciu tekutiny na častice používame Cooper-Fryeov vzťah a na interakcie v konečnom stave model využíva transportný model Simulating Many Accelerated Strongly-interacting Hadrons (SMASH). Tento hybridný model bol overený porovnaním s existujúcimi dátami z programu BES na RHIC-u.

Abstract

The hunt for finding the critical endpoint of the QCD phase diagram requires a research of heavy-ion collisions at energies ranging from a few to tens of GeV per nucleon-nucleon pair. However, simulations at such low energies are more complex than at energies of the order of hundreds to thousands of GeV, including a longer interpenetration time or a finite baryon density in the fluid. The first part of this work investigates the possibilities of using a hybrid hydrodynamic model built for the LHC energy at energies of the BES program at RHIC. When the initial state is extended to three dimensions, this model can quite effectively reproduce the experimental data. The second part of the dissertation describes the development of a state-of-the-art hybrid model that takes care of all the challenges that occur at the studied energy range. The basis of the model is a novel approach to the three-fluid hydrodynamic simulation. For the fluid-to-particles transition, the Cooper-Frye prescription is used, and for the final-state interactions, the model uses the transport model SMASH. This hybrid model has been validated against the existing results from BES at RHIC.

Contents

List of Figures

List of Tables

List of Acronyms

3FH 3-Fluid Hydrodynamic

AFTER@LHC A Fixed Target Experiment at LHC

AdS/CFT anti-de-Sitter/conformal field theory

ALICE A Large Ion Collider Experiment

AMPT A Multi-Phase Transport

ATLAS A Toroidal LHC ApparatuS

BES Beam Energy Scan

BNL Brookhaven National Laboratory

BRAHMS Broad RAnge Hadron Magnetic Spectrometer

BW Blast-wave

CBM Compressed Baryonic Matter

CEP critical endpoint

CERN European Organisation for Nuclear Research

CFL Courant-Friedrichs-Lewy

CGC Color Glass Condensate

CMS Compact Muon Solenoid

CP-symmetry charge conjugation parity symmetry

DESY Deutsches Elektronen-Synchrotron

DORIS Double Ring Store

DRAGON DRoplet and hAdron Generator for Nuclear collisions

EoS equation of state

EP event-plane

FAIR Facility for Antiproton and Ion Research

FCC Future Circular Collider

Fermilab Fermi National Accelerator Laboratory

GLISSANDO GLauber Initial-State Simulation AND mOre

GMC Glauber Monte Carlo

HBT Hanbury-Brown and Twiss

HKM hydro-kinetic model

HRG Hadronic Resonance Gas

iEBE-VISHNU Event-By-Event Viscous Israel Stewart Hydrodynamics aNd UrQMD

IS initial state

J-PARC Japan Proton Accelerator Research Complex

lattice QCD Quantum Chromodynamics on a lattice

LHC Large Hadron Collider

LHCb LHC beauty

MUSIC MUScl for Ion Collisions

NBD Negative Binomial Distribution

NICA Nuclotron-based Ion Collider fAcility

PHENIX Pioneering High Energy Nuclear Interaction eXperiment

QCD Quantum Chromodynamics

QGP Quark-Gluon Plasma

qQGP quasi-particle QGP

RHIC Relativistic Heavy Ion Collider

SHASTA Sharp And Smooth Transport Algorithm

SLAC Stanford Linear Accelerator Center

SM Standard Model

SMASH Simulating Many Accelerated Strongly-interacting Hadrons

SPH Smoothed Particle Hydrodynamics

SPS Super Proton Synchrotron

STAR Solenoidal Tracker at RHIC

THERMINATOR2 THERMal heavy IoN generATOR version 2

TRENTo Reduced Thickness Event-by-event Nuclear Topology

UrQMD Ultra relativistic Quantum Molecular Dynamics

v-USPhydro viscous Ultrarelativistic Smoothed Particle hydrodynamics

vHLLE viscous Harten–Lax–van Leer–Einfeldt

Chapter 1

Introduction

One of the main objectives of nuclear physics in the last decades is the search for and study of Quark-Gluon Plasma (QGP), which filled the whole universe a few microseconds after the Big Bang. This new state of matter has been successfully created in ultra-relativistic heavy-ion collisions at the Large Hadron Collider (LHC) at European Organisation for Nuclear Research (CERN) in Geneva and also at Relativistic Heavy Ion Collider (RHIC) at Brookhaven National Laboratory (BNL) in New York.

Hydrodynamics is used to describe the evolution of matter produced in heavy-ion collisions since Landau and Bjorken [1, 2]. Comparison of experimental data with phenomenological models leads to the conclusion that the QGP is the most perfect fluid in the universe [3], which supports the motivation to use hydrodynamics. However, pure hydrodynamic models are no longer used to describe heavy-ion collisions. Instead, hybrid models are widely used, because they better describe the hadron phase and freeze-out while using event-by-event initial state (IS).

Most of the hydrodynamic models currently used [4–12] are made for top RHIC and LHC energies. However, the number of lower-energy experiments is increasing. The Beam Energy Scan (BES) program is currently running at RHIC and the NA61/SHINE experiment at CERN. Two other facilities in Dubna and Darmstadt are under construction, and one is planned in Japan.

The main issue of heavy-ion collisions at low energies is that the initial collision takes a long time. During this time, some of the nucleons have already collided, while others still expect their initial interactions.

Thus, we created a hybrid model that deals with all the challenges that come along with low energies. The basis of this model consists of the three-fluid hydrodynamics, which treats the gradual transfer of energy from the incoming nuclei to the fireball fluid. Hydrodynamics includes the shear and bulk viscosities

in the Israel-Stewart framework. The fluid-to-particle transition is handled with the Cooper-Frye prescription, and hadronic sampling with the use of a Monte Carlo procedure.

Chapter 2 offers a quick introduction to the history of particle physics, the discovery of QGP and its properties. Chapter 3 contains information about important observables that connect theoretical models with experimental data and extract information about QGP. Chapter 4 describes the basic hydrodynamic equations together with viscous corrections. In addition, an overview of the hydrodynamic and hybrid models currently used is available in Sect. 4.3. Chapter 5 our extension of the initial state models used for top RHIC energies and above, to moderately lower collision energies $\sqrt{s_{\mathrm{NN}}} = 27$ and $62.4\,\mathrm{GeV}$. Chapter 6 begins with the motivation for our model proposal. The whole model is described, namely the initial conditions, the hydrodynamic evolution, the equation of state (EoS) and the particlization. Chapter 7 shows the main results of our state-of-the-art model. Chapter 8 then summarizes the entire thesis.

This work uses natural units, in which $c = \hbar = k_B = 1$. Therefore, the mass, energy, momentum, and temperature have the same unit, for which GeV will be used. Moreover, this unit system results in time and length having the same unit, and we will use femtometers for both. Finally, multiplying the reduced Planck constant and the speed of light, we obtain $\hbar c = 1$, but in normal units $\hbar c = 0.1973\,\mathrm{GeV}\cdot\mathrm{fm}$. This means that gigaelectronvolts can be converted into femtometers and vice versa using the formula

$$1\,\mathrm{fm} = \frac{1}{0.1973\,\mathrm{GeV}}. \tag{1.1}$$

Chapter 2

Quark-Gluon Plasma

2.1 Brief History of Particle Physics

Nuclear physics began to write its history with the discovery of radioactivity by Henri Becquerel in 1896 [13]. Next year, Thomson discovered the electron [14]. These discoveries indicated that the atom has some non-elementary structure. Because atoms are neutral and electrons have a negative electric charge, atoms have to consist of some other part with a positive electric charge. The first model of the atom was presented by Thomson [15], but his idea of "a number of negatively electrified corpuscles enclosed in a sphere of uniform positive electrification" was disproved by Rutherford's experiment [16]. This experiment showed that atoms have a very small and very dense positively charged nucleus.

Several years later, Rutherford found that the hydrogen nucleus is contained in other nuclei, leading to the discovery of the proton [17]. He also theorized about neutral particles located in the nucleus. Due to its neutral charge, the experimental discovery of the neutron took more than 10 years and was performed by Chadwick [18]. At this point in history, all matter consisted of three elementary particles instead of almost a hundred elements.

2.1.1 Quarks and Gluons

The situation changed during the 1950s when particle accelerators and cosmic ray detectors allowed scientists to study inelastic scattering experiments on protons with energies higher than 100 MeV. These experiments created new particles with unusually long lifetimes. Due to their strange behaviour, they got the name strange particles. Obtaining higher and higher collision energies and improving particle detectors resulted in more and more particle discoveries.

Soon there were almost a hundred elementary particles, and particle physics did not seem to be elementary anymore. This amount of elementary particles started to be called a particle zoo.

In 1961, Murray Gell-Mann created an organizational scheme for particles, based on SU(3) flavour symmetry. He called it the eightfold way [19]. This led to the proposal of the quark model, which was done independently by Murray Gell-Mann [20] and George Zweig [21, 22], both in 1964. Their model involved three flavours of quarks: up, down, and strange. The fourth quark (charm) was suggested in the same year by Bjorken and Glashow [23] and predicted by Glashow, Iliopoulos, and Maiani in 1970 [24]. The last two quarks, top and bottom (also called beauty), were added in 1973 by Kobayashi and Maskawa as a possible explanation for the experimental observation of violation of charge conjugation parity symmetry (CP-symmetry) [25].

Experimental evidence that the proton is indeed not an elementary particle was found in deep-inelastic scattering experiments at the Stanford Linear Accelerator Center (SLAC) in California in 1968 [26, 27]. The results showed that the proton contained point-like objects that were later identified as quarks up and down. These experiments also provided a piece of indirect evidence for the existence of strange quarks. The rest of the quarks were experimentally confirmed during the next several decades.

In 1964, Oscar Greenberg suggested that quarks are parafermions of rank three [28]. This suggestion was similar to assuming that each quark flavour exists in three different colour states and that observed hadrons correspond to neutral colourless combinations. Due to the strong coupling constant and non-Abelian interaction, quarks cannot exist as free particles but are confined inside hadrons. Soon after Greenberg's paper, Yochiro Nambu suggested that the strong force that interacts between quarks is mediated by an octet of gauge fields [29]. The theory of the colour octet gluon was proposed in 1973 [30].

Gluons were experimentally observed for the first time in 1978 at the electron-positron collider Double Ring Store (DORIS) at Deutsches Elektronen-Synchrotron (DESY) in Hamburg [31]. Interpreting the three-gluon decay resulted in the best description of the data. This experiment also confirmed that the gluon has spin 1.

Currently, quarks (up, down, strange, charm, bottom, top), leptons (electron, muon, tauon, and their neutrinos), and intermediate bosons (photon, $W^{\pm}$, Z, gluon, H^{0}) are considered elementary particles, and together they are described by the Standard Model (SM) (Fig. 2.1), the most successful theoretical model so far. The last piece of the puzzle was the Higgs boson, which was discovered in 2012 at the LHC [32]. Despite many successful predictions, there are still prob-

lems this theory cannot explain, e.g. gravity or dark matter.

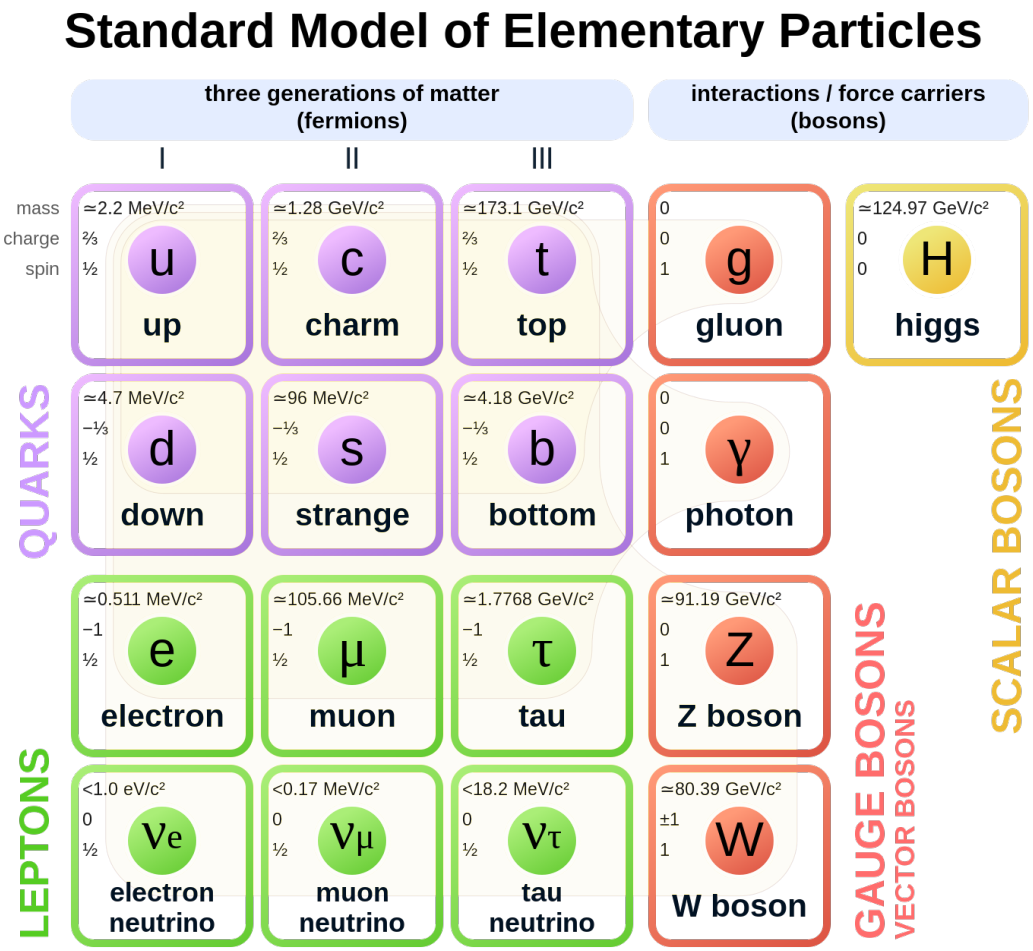

Figure 2.1: Table of elementary particles of Standard Model. Taken from [33].

2.1.2 Discovery of QGP

During the 1970s and 1980s, the theory that predicts the new state of matter was developed from Quantum Chromodynamics (QCD) [34, 35]. In this state of matter, quarks and gluons are freed from hadrons, which is called quark deconfinement. The QGP can be created only under special conditions, such as extremely high temperature and/or baryon density, which can be found in the collapse of massive stars or the cores of neutron stars. It is believed that the QGP filled the whole universe a few microseconds after the Big Bang.

Experiments started looking for QGP in the late 1980s at CERN. During 15 years, 7 experiments (NA44, NA45, NA49, NA50, NA52, WA97, and WA98) have been collecting data until 10 February 2000, when CERN officially announced that they have found "compelling evidence for the existence of a new state of

matter in which quarks, instead of being bound up into more complex particles such as protons and neutrons, are liberated to roam freely" [36]. Their evidence was based on a complex argument that combined observations of different quantities.

Later, clearer evidence was used at RHIC and was based on the jet quenching effect. When two high-momentum partons are creating jets, they have to aim back-to-back in transverse plane because of the momentum conservation. However, in Au+Au collisions the second jet is not visible, which is usually shown by Fig. 2.2. Such energy loss is explained by a parton flying through a densely coloured medium. The second jet is not quenched in small systems, i.e. p+p collisions. Later, the collective flow was observed in p+p collisions. It is still unclear whether the QGP is or is not created in such collision system, and discussions are ongoing [37, 38].

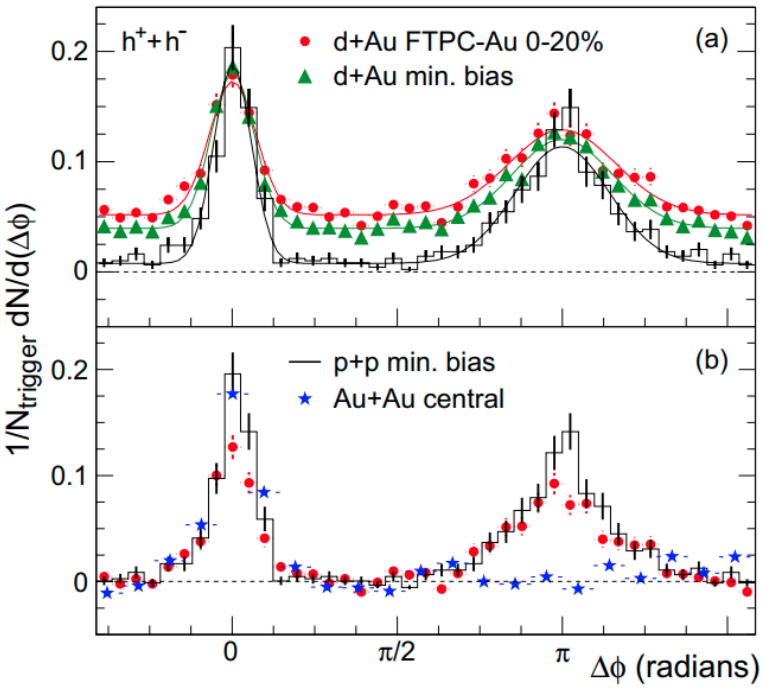

Figure 2.2: (a) Two-particle azimuthal distributions for central d+Au and p+p collisions. (b) Two-particle azimuthal distributions for central d+Au, central Au+Au and p+p collisions. Taken from [39].

2.2 Quark Model

The quark model (as proposed in 1964) can be represented by three quarks forming a triangular pattern. Two directions along the edges of the triangle cor-

respond to constant electric charge Q and constant strangeness S. Antiquarks form another triangular pattern with opposite electric charge and strangeness. These triangular formations are triplets of SU(3). Both triplets are illustrated in Fig. 2.3.

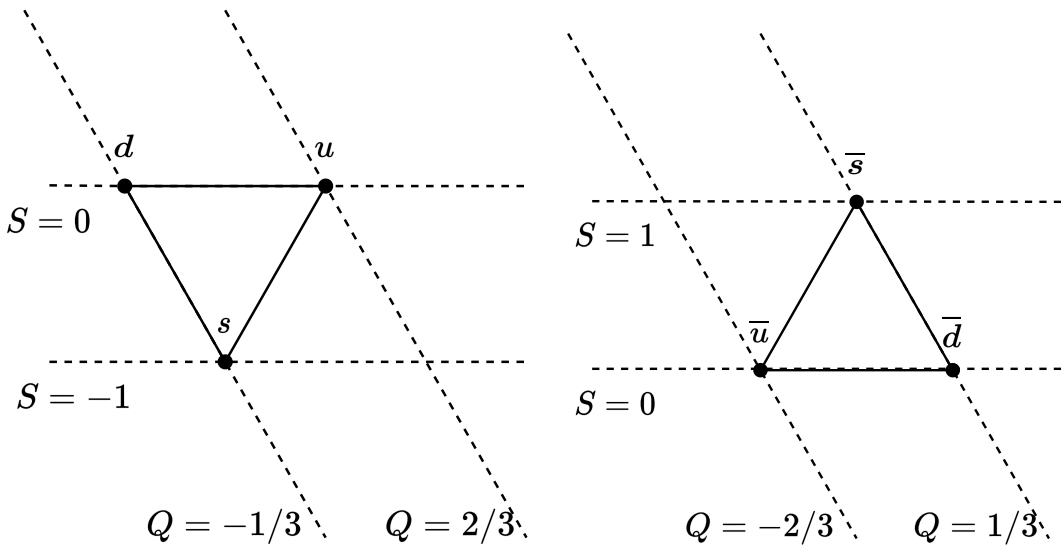

Figure 2.3: Quark (left) and antiquark (right) triplets. Horizontal axis corresponds to third isospin component I_3 and vertical axis corresponds to hypercharge Y.

Mesons are particles consisting of pairs of quarks and antiquarks. Assuming three quark flavours, there are 9 possible combinations of creating a meson. In SU(3), the combinations are grouped into an octet and a singlet:

$$3 \otimes \bar{3} = 8 \oplus 1. \tag{2.1}$$

Since quarks have spin $1/2$, they can actually exist in 6 different states. Therefore, the flavour SU(3) symmetry can be extended into the flavour-spin SU(6) symmetry. The combinations in SU(6) are

$$6 \otimes \bar{6} = 35 \oplus 1, \tag{2.2}$$

where 35-plet can be decomposed with respect to SU(3)$\otimes$SU(2):

$$35 = (8_f \otimes 1_s) \oplus (8_f \otimes 3_s) \oplus (3_f \otimes 1_s), \tag{2.3}$$

where the subscripts f and s correspond to the flavour and spin states, respectively. Moreover, the number of states with spin s is given as

$$n_s = 2s + 1. \tag{2.4}$$

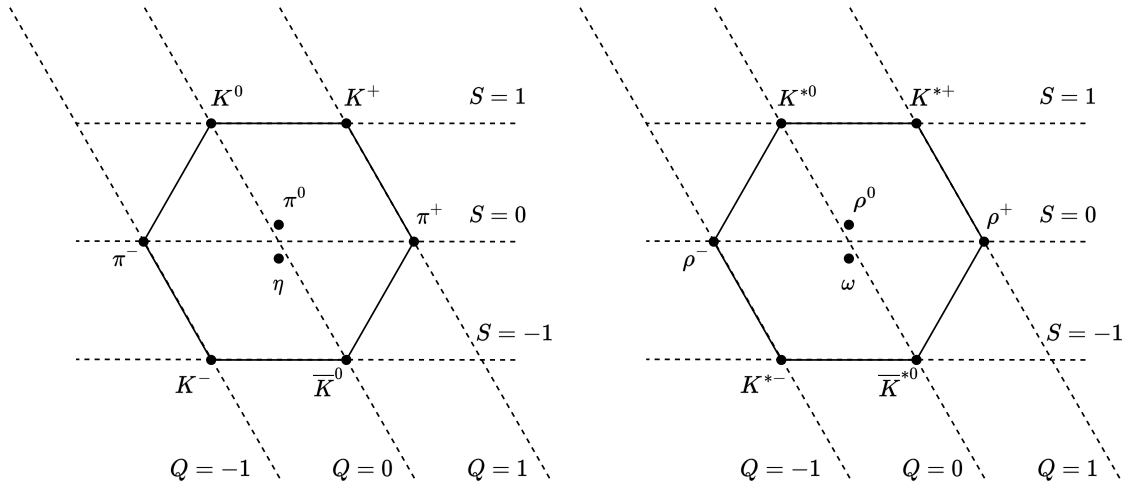

Figure 2.4: Octet of pseudoscalar mesons (left) and octet of vector mesons (right).

This means that there are two octets of mesons: an octet of vector mesons (with spin 1) and an octet of pseudoscalar mesons (with spin 0). Both octets are shown in Fig. 2.4.

Baryons consist of three quarks. They also have baryon number $B = 1$. Since mesons have zero baryon number, it means that quarks have baryon number $B = 1/3$ and antiquarks have opposite baryon number. The combinations of three quarks according to the SU(3) symmetry are

$$3 \otimes 3 \otimes 3 = 1 \oplus 8 \oplus 8 \oplus 10. \tag{2.5}$$

In SU(6) flavour-spin symmetry, the combinations are

$$6 \otimes 6 \otimes 6 = 56 \oplus 70 \oplus 70 \oplus 20. \tag{2.6}$$

The fully symmetric 56-plet can be decomposed into SU(3)$\otimes$SU(2) symmetry:

$$56 = (10_f \otimes 4_s) \oplus (8_f \otimes 2_s). \tag{2.7}$$

This octet and decuplet of baryons are shown in Fig. 2.5.

2.3 Quantum Chromodynamics

Quantum chromodynamics is a theory of strong nuclear interaction. Particles interacting by strong interaction have non-zero colour charge. The range of the interaction is about 10^{-15} m and it is responsible for keeping quarks within

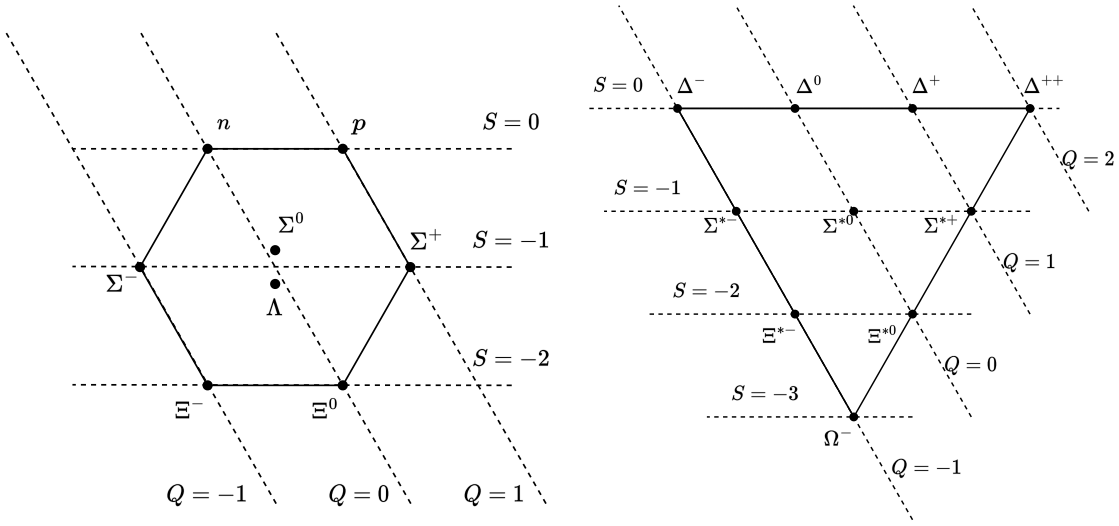

Figure 2.5: Octet of baryons with spin $1/2$ (left) and decuplet of baryons with spin $3/2$ (right).

hadrons, keeping nucleons within nuclei, and for particle production in heavy-ion collisions.

The quark's colour charge can take one of three "signs"[1], and when all three are represented in the hadron, the total colour charge is zero. This is similar to the RGB additive colour model, in which red, green, and blue colours together give white colour. This analogy is why the term colour is used when describing the strong interaction.

The mediator of the strong interaction is the gluon, which is a massless and electrically neutral vector boson. Unlike photons, gluons carry the charge of the interaction they mediate. Each gluon carries a colour and anti-colour charge, which gives 9 possible combinations. However, the strong interaction has colour SU(3) symmetry, and therefore colour and anti-colour charges combine analogously to quark and antiquark:

$$3 \otimes \bar{3} = 8 \oplus 1. \tag{2.8}$$

The singlet state is

$$\frac{r\bar{r} + b\bar{b} + g\bar{g}}{\sqrt{3}}. \tag{2.9}$$

This state is colourless and does not mediate any interaction between colour states. It could interact with another colour singlet; however, gluons cannot exist as free particles and, therefore, they cannot exist in singlet state. On the

[1] Gravity's charge (mass) can take one sign, electric charge can take two opposite signs, which together give zero.

other hand, the colour octet contains eight colour states of gluons:

$$\begin{array}{ll} \frac{r\bar{b}+b\bar{r}}{\sqrt{2}}, & -i\frac{r\bar{b}-b\bar{r}}{\sqrt{2}}, \\ \frac{r\bar{g}+g\bar{r}}{\sqrt{2}}, & -i\frac{r\bar{g}-g\bar{r}}{\sqrt{2}}, \\ \frac{b\bar{g}+g\bar{b}}{\sqrt{2}}, & -i\frac{b\bar{g}-g\bar{b}}{\sqrt{2}}, \\ \frac{r\bar{r}-b\bar{b}}{\sqrt{2}}, & \frac{r\bar{r}+b\bar{b}-2g\bar{g}}{\sqrt{6}}. \end{array}$$

The coupling constant of the strong interaction is defined as

$$\alpha_s = \frac{g_s^2}{4\pi}, \tag{2.10}$$

where g_s is the colour charge of the constituent quark. This coupling constant depends on the transferred momentum and is therefore frequently called running coupling constant. Its value decreases with increasing energy according to

$$\alpha_s(Q) \approx \frac{12\pi}{(11n_c - 2n_f)\ln\left(\frac{Q^2}{\Lambda^2}\right)}, \tag{2.11}$$

where n_c is the number of colour charges, n_f is the number of quark flavours, Q is the transferred momentum, and Λ is a scaling parameter. At low energies, the coupling constant gets the value $\alpha_s \approx 1$. Figure 2.6 shows the momentum dependence of α_s obtained from different measurements combined together.

The logarithmic decrement of the running coupling constant with momentum means that the strong force vanishes inside hadrons and quarks can move freely. This phenomenon is called asymptotic freedom [41, 42]. At larger distances, the strong interaction between quark and antiquark becomes strong enough to produce another quark-antiquark pair. Thus, two quark-antiquark pairs are produced when trying to separate quarks, instead of getting free quarks. This phenomenon is called colour confinement.

Unlike quantum electrodynamics, QCD allows for three- and four-gluon interactions. This is possible because the gauge theory is non-Abelian. All possible interactions between quarks and gluons are contained in the QCD Lagrangian

$$\mathfrak{L}_{\text{QCD}} = \bar{\psi}_i \left(i\gamma^\mu \left(\partial_\mu \delta_{ij} - i\frac{g_s}{2}(\lambda_a)_{ij}\mathcal{A}_\mu^a \right) - m\delta_{ij} \right) \psi_j - \frac{1}{4} G_{\mu\nu}^a G_a^{\mu\nu}. \tag{2.12}$$

Here, ψ_i is the quark field, γ^μ are Dirac gamma matrices, δ_{ij} is Kronecker delta, λ_a are Gell-Mann matrices, $\mathcal{A}_\mu^a$ is the gluon field, m_q is the quark mass and $G_{\mu\nu}^a$ is the gluon field strength tensor defined as

$$G_{\mu\nu}^a = \partial_\mu \mathcal{A}_\nu^a - \partial_\nu \mathcal{A}_\mu^a + g f^{abc} \mathcal{A}_\mu^b \mathcal{A}_\nu^c, \tag{2.13}$$

where f^{abc} are the structure constants of SU(3).

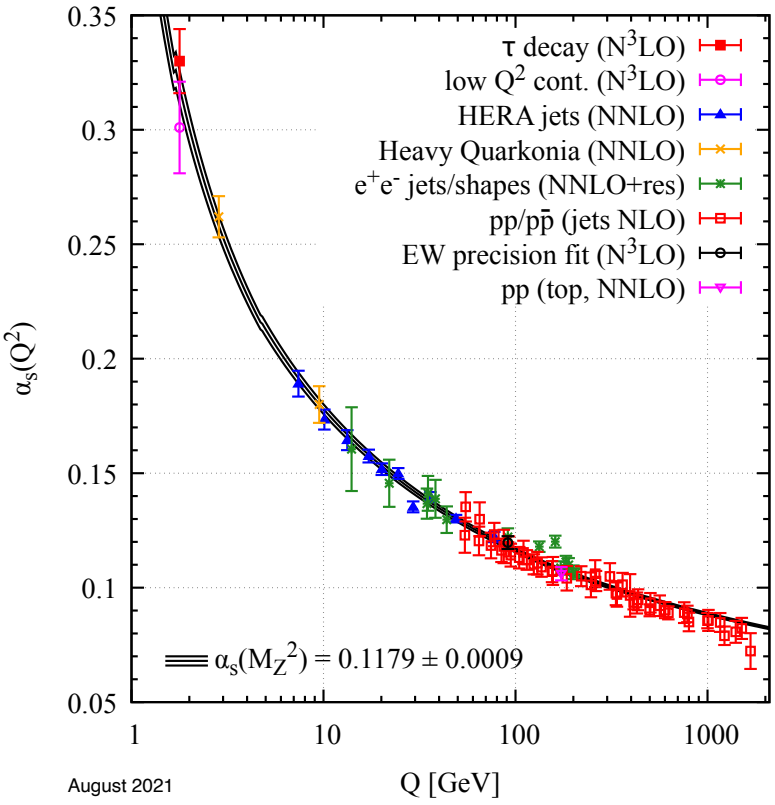

Figure 2.6: Summary of measurements of running coupling constant α_s as a function of the momentum scale Q. Taken from [40].

2.4 Heavy-Ion Collisions

To obtain the QGP in laboratory conditions, it is necessary to create an extremely high energy density. This can be done by accelerating heavy nuclei to ultrarelativistic speed and then colliding them together. This leads to phase transition and the creation of the QGP.

The collisions melt the nucleons and create the QGP filled with asymptotically free and colour-deconfined quarks and gluons. Due to the high energy density gradient, there is also a high pressure gradient, which causes the expansion and cooling of the QGP. The energy density gradually decreases until the quarks recombine to hadrons. The plasma becomes a gas of hadrons. This process is called hadronization. In this phase, the hadrons are still close enough, so two hadrons can interact by exchanging mesons. This fireball continues to expand until the strong interaction between hadrons drops out, and particles are emitted into detectors. First, the inelastic processes of the conversion of hadronic species stop, which is called a chemical freeze-out, and then the elastic processes stop, which is called a kinetic freeze-out. A weaker electromagnetic interaction of charged hadrons lasts for some time after the

freeze-out, and long-lived hadronic resonances decay on the way to the detector. The whole process is sketched in Fig. 2.7.

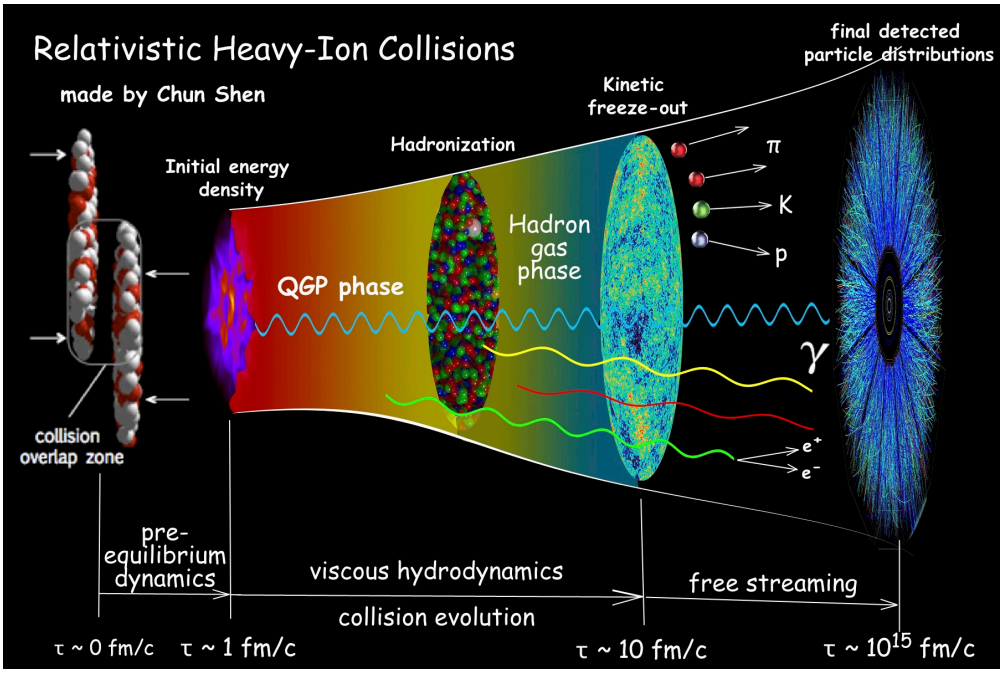

Figure 2.7: The sketch of the evolution of QGP in heavy-ion collisions, which is used worldwide to represent this process. However, as an image of kinetic freeze-out, the figure of relic radiation is used, which has nothing in common with heavy-ion collisions. Taken from [43].

Generally, particle collisions may be performed as either a fixed target experiment, where one beam of particles is accelerated and then collided into stationary particles, or as a collider experiment, where two beams of particles are accelerated oppositely and then collided together. The fixed-target experiment can reach much higher luminosity (rate of interactions) and is easier and cheaper to build. However, in such an experiment, a lot of energy is transferred into the longitudinal momenta of newly created particles. In a collider experiment, the energy is approximately 4 times larger compared to the fixed target experiment with a beam of the same energy, and most of the energy of the incoming particles is available to produce new particles.

The energy of the collision is usually stated using the variable $\sqrt{s_{\mathrm{NN}}}$, which is total center-of-mass energy per nucleon-nucleon pair. This invariant is one of the Mandelstam variables defined as

$$s = (p_1 + p_2)^2, \tag{2.14}$$

where $p_{1,2}$ are the four-momenta of the incoming particles. In the case of the collider experiment with two colliding particles having the same mass, the Man-

delstam s is simply

$$s = 4\left(|\vec{p}|^2 + m^2\right). \tag{2.15}$$

Sometimes, the collision energy is stated via the beam energy in fixed target mode E_{lab}. One can convert between these two energies using

$$\sqrt{s_{\text{NN}}} = \sqrt{2m_N E_{\text{lab}} + 2m_N^2}, \tag{2.16}$$

where $m_N = 0.939\,\text{GeV}$ is the nucleon mass.

2.4.1 Current Heavy-Ion Colliders

Currently, there are two heavy-ion colliders: RHIC and LHC. RHIC reaches energies ranging from a few GeV to the top energy $\sqrt{s_{\text{NN}}} = 200\,\text{GeV}$. It mainly collides gold nuclei. At the moment there is only one operating experiment - STAR (Solenoidal Tracker at RHIC), which is well designed for the study of the collective expansion of the QGP. Another experiment, PHENIX (Pioneering High Energy Nuclear Interaction eXperiment), which focused on direct probes such as electrons, muons, and photons, is now being upgraded to sPHENIX, an experiment that will study jets, jet correlations, and upsilons. Two other experiments, PHOBOS[2] and BRAHMS (Broad RAnge Hadron Magnetic Spectrometer), ended their operation in 2005 and 2006, respectively.

LHC is the largest hadron collider ever built. It reaches energies $\sqrt{s_{\text{NN}}} = 2.76$ and $5.02\,\text{TeV}$ in Pb+Pb collisions and $\sqrt{s_{\text{NN}}} = 13\,\text{TeV}$ in proton-proton collisions. Its major accomplishment was the discovery of the Higgs boson, which was announced in 2012. There are four large experiments at the LHC: ALICE (A Large Ion Collider Experiment), ATLAS (A Toroidal LHC ApparatuS), CMS (Compact Muon Solenoid), and LHCb (LHC beauty). ALICE studies the physics of QGP and quark deconfinement. ATLAS focused on searching for the Higgs boson and now is looking at physics beyond SM. CMS also studies SM and is looking for new physics. LHCb specializes in studying the differences between matter and antimatter using the bottom quark.

Before these two colliders, the accelerator Tevatron located in Fermi National Accelerator Laboratory (Fermilab) played an important role and discovered several new particles, including the top quark [44]. In addition, CERN's Super Proton Synchrotron (SPS) operated as a hadron collider from 1981 to 1991. For the future CERN proposed building Future Circular Collider (FCC), which should reach energy $\sqrt{s_{\text{NN}}} = 100\,\text{TeV}$ in $100\,\text{km}$ long circular accelerator.

[2] not an acronym

2.5 Phase Diagram

The QGP is a new state of matter, which means that there must also be some phase transition between the QGP and the hadron matter. Since the first idea of QGP, its phase diagram (Fig. 2.8) has also been studied.

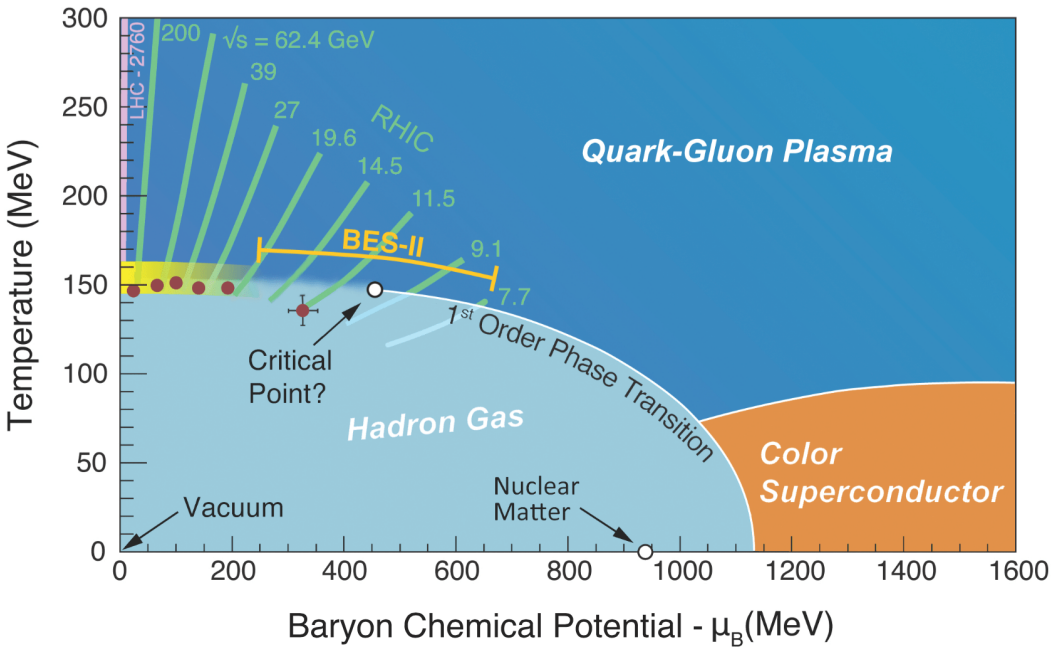

Figure 2.8: The phase diagram of QGP with approximate trajectories corresponding to the matter produced in heavy-ion collisions at different energies and an estimated location of critical endpoint (CEP). Taken from [45].

Thanks to Quantum Chromodynamics on a lattice (lattice QCD) it is possible to make calculations from the first principles at zero baryon chemical potential μ_B. These calculations predict a crossover phase transition between the QGP and the hadron matter at a temperature $T = 154 \pm 9$ MeV [46]. In the crossover phase transition, the system changes radically, but without any discontinuity in the thermodynamic observables (Fig. 2.9), so it occurs in a region of the phase diagram rather than a singular point. At a finite baryon chemical potential, the lattice QCD encounters the so-called sign problem [47], which does not allow for a calculation from the first principles. However, there are methods to obtain QGP properties at a small baryon chemical potential, e.g. Taylor expansion around $\mu_B = 0$ [48] or analytic continuation from imaginary μ_B [49].

At very large μ_B and low temperatures, perturbative QCD may be used to extract information about hadronic matter inside neutron stars and its EoS [53]. Recently, a study of neutron star mergers showed that there is a first-order phase transition between quark and hadronic matter [54].

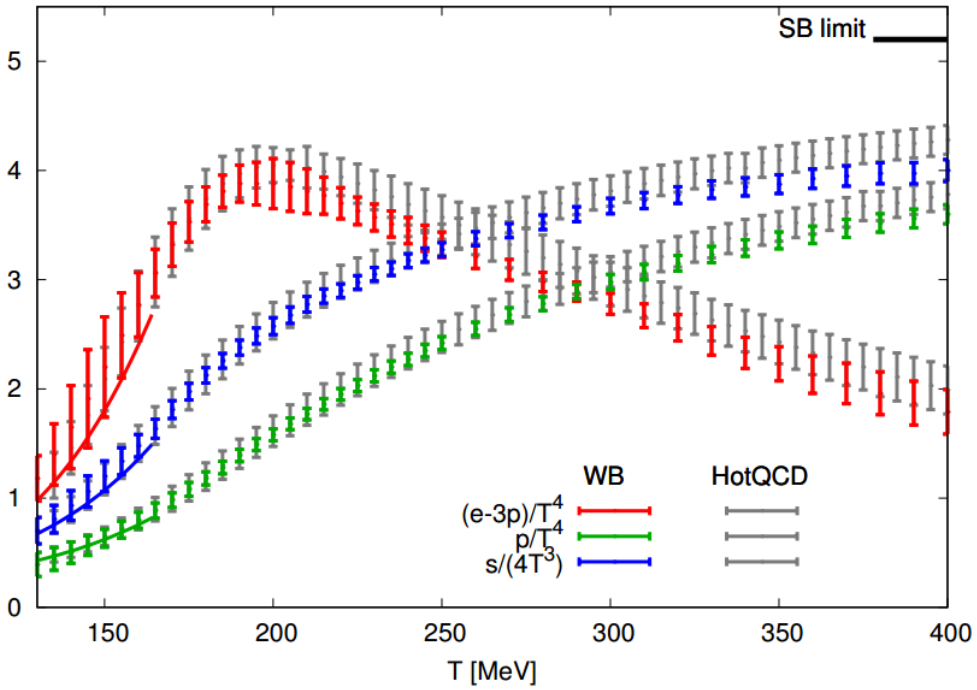

Figure 2.9: Temperature dependence of trace anomaly, entropy density and pressure showing phase transition obtained by lattice QCD. The gray points are from the HotQCD collaboration [50] and coloured points are from Wuppertal-Budapest collaboration [51]. Taken from [52].

The point that separates these two phase transitions is called a critical end-point (CEP) [55] and its location is probably the most interesting question of the QCD these days. However, in heavy-ion collision experiments, it is not known which kind of phase transition the system undergoes, making the task very difficult.

Chapter 3

Observables

Heavy-ion collision experiments can provide us with a lot of information about the properties of the QGP. Unfortunately, these properties cannot be measured directly. Instead, a phenomenological model needs to be constructed that takes the QGP properties as input and returns measurable quantities as output. The properties of QGP are then extracted by comparing the experimental and simulated data. More details on the phenomenology of heavy-ion collisions can be found in [56]. This chapter serves as an overview of the most important observables.

3.1 Milne Coordinates

Before we introduce the observables, it is useful to introduce Milne coordinates. In high-energy heavy-ion collisions, the Lorentz contraction in the beam direction causes the colliding nuclei to look like thin pancakes. In hydrodynamic simulations, the space is divided into a grid, and at the beginning of the simulation the contraction can cause the whole fireball to be contained in one layer of this grid in the longitudinal direction. And the contraction is stronger with higher collision energy. In Milne coordinates, the $t-z$ plane is redefined using the longitudinal proper time τ and the space-time rapidity η_s defined as:

$$\tau = \sqrt{t^2 - z^2}, \tag{3.1a}$$

$$\eta_s = \frac{1}{2} \ln\left(\frac{t+z}{t-z}\right). \tag{3.1b}$$

The transverse coordinates x and y remain unchanged. The Milne coordinate system is natural to describe the flow of matter from an infinitely thin source $z \to 0$ at $t \to 0$, which leads to a scaling flow $v_z = z/t$. In the Milne coordinate frame, this corresponds to a finite initial source size in the η_s direction and $v_{\eta_s} = 0$. From

a practical point of view, the coordinate frame "expands with the expanding medium", which is advantageous for an accurate numerical simulation. It is also useful to write down reversed formulas:

$$z = \tau \sinh \eta_s, \tag{3.2a}$$

$$t = \tau \cosh \eta_s. \tag{3.2b}$$

3.2 Rapidity Distributions

The most elementary observable that can be studied in experimental data is multiplicity, the total number of particles produced in a heavy-ion collision. Since the detection of particles with neutral electric charge is complicated, experimental analysis usually involves only charged particles. It may seem that one number cannot provide us with much information; however, one can study its dependence on the collision energy, centrality, its fluctuations or distributions.

The interesting thing to study is the distribution of the multiplicity along the longitudinal velocity. However, in ultra-relativistic collisions, it is more useful to use rapidity instead of velocity, defined as

$$\mathrm{y} = \frac{1}{2} \ln \left(\frac{E + p_z}{E - p_z} \right) = \frac{1}{2} \ln \left(\frac{1 + v_z}{1 - v_z} \right) = \operatorname{arctanh}(v_z), \tag{3.3}$$

where E is the particle energy, p_z is the longitudinal momentum, and v_z is the longitudinal velocity. Therefore, the rapidity distribution is the number of particles per unit of rapidity at different rapidities. The shape of the rapidity distribution carries information, e.g. about baryon stopping. Using rapidity, the particle four-momentum can be parametrized

$$p = (E, \vec{p}) = (m_T \cosh \mathrm{y}, p_T \cos \phi, p_T \sin \phi, m_T \sinh \mathrm{y}), \tag{3.4}$$

where $p_T = \sqrt{p_x^2 + p_y^2}$ is the transverse momentum, $m_T = \sqrt{m^2 + p_T^2}$ is the transverse mass, and ϕ is the azimuthal angle of the momentum of the particle in the transverse plane.

Similarly to rapidity, one can define the so-called pseudorapidity:

$$\eta = \frac{1}{2} \ln \left(\frac{|\vec{p}| + p_z}{|\vec{p}| - p_z} \right) = - \ln \left(\tan \frac{\theta}{2} \right), \tag{3.5}$$

where θ is the angle between the momentum of the particle and the direction of the beam. From the definitions (3.3) and (3.4) we can write down

$$p_0 = m_T \cosh \mathrm{y}, \qquad p_z = m_T \sinh \mathrm{y}, \tag{3.6a}$$

$$|\vec{p}| = p_T \cosh \eta, \qquad p_z = p_T \sinh \eta. \tag{3.6b}$$

From these equations, it can be seen that rapidity and pseudorapidity become equal in the limit $m/E \to 0$. Since these two quantities are similar for $|p| \gg m$, experiments usually measure pseudorapidity instead of rapidity, because it can be obtained by simply measuring the angle θ.

The relation between rapidity distribution and pseudorapidity distribution is

$$\frac{\mathrm{d}N}{\mathrm{d}\eta} = \sqrt{1 - \frac{m^2}{m_T^2 \cosh^2 \mathrm{y}}} \frac{\mathrm{d}N}{\mathrm{dy}}. \tag{3.7}$$

The difference between these two distributions is illustrated in Fig. 3.1. This figure shows the origin of the two-peak structure in the pseudorapidity distribution seen in the experimental data and is caused by the factor in (3.7).

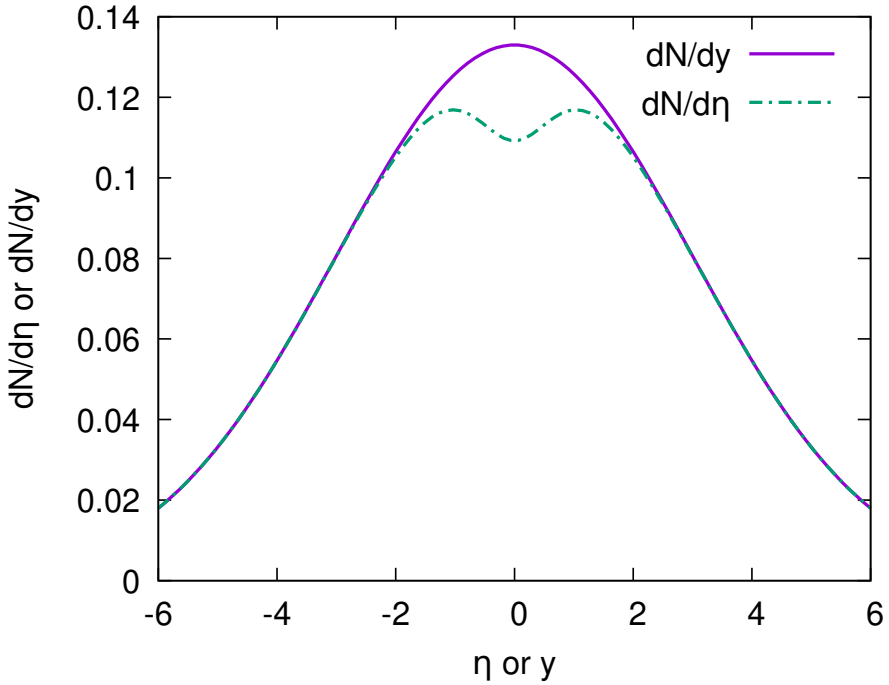

Figure 3.1: Rapidity vs pseudorapidity distribution illustration. For rapidity distribution, simple Gaussian with width $\sigma = 3$ was chosen. Pseudorapidity distribution was calculated using (3.7) for pion with $p_T = 200$ MeV.

The matter produced in the midrapidity region, where $\mathrm{y} \approx \eta \approx 0$, is the least contaminated by the incoming baryon charge and also does not carry any longitudinal momentum, and therefore it carries pure information about the QGP.

The BES program has not yet provided any rapidity distributions; however, there are data from the PHOBOS experiment at RHIC. The paper [57] shows pseudorapidity distributions of charged particles in Au+Au (energies $\sqrt{s_{\mathrm{NN}}} = 19.6$, 62.4, 130 and 200 GeV), Cu+Cu ($\sqrt{s_{\mathrm{NN}}} = 22.4$, 62.4 and 200 GeV), d+Au and p+p collisions.

3.3 Transverse Momentum Spectra

Another way to study multiplicity is to study its momentum dependence. The Lorentz invariant momentum spectrum is defined as $E\mathrm{d}^3N/\mathrm{d}p^3$. The momentum differential can be rewritten using rapidity as

$$\mathrm{d}p^3 = \mathrm{d}p_x\mathrm{d}p_y\mathrm{d}p_z = p_T\mathrm{d}p_T\mathrm{d}\phi E\mathrm{dy}. \tag{3.8}$$

As was mentioned before, the region of main interest is midrapidity and therefore the transverse momentum spectrum is being calculated. When calculating the transverse momentum spectrum, the momenta are integrated over ϕ. Thus, the transverse momentum spectrum is usually written as

$$E\frac{\mathrm{d}^3N}{\mathrm{d}p^3} = \frac{1}{2\pi}\frac{\mathrm{d}N^2}{p_T\mathrm{d}p_T\mathrm{dy}}. \tag{3.9}$$

Similarly, one can also calculate the transverse mass spectrum defined as

$$\frac{1}{2\pi}\frac{\mathrm{d}N^2}{m_T\mathrm{d}m_T\mathrm{dy}}. \tag{3.10}$$

The transverse momentum distribution is a very useful probe of QGP because it has a Boltzmann shape. This allows the system temperature to be extracted from the spectrum slope in a logarithmic plot.

The transverse momentum spectra for identified hadrons (π^+, π^-, K^+, K^-, p, and $\overline{\mathrm{p}}$) are provided by STAR [58–62] in Au+Au collisions at BES energies $\sqrt{s_{\mathrm{NN}}} = 7.7, 11.5, 19.6, 27, 39, 62.4, 130$ and 200 GeV.

3.4 Collective Flow

The transverse momentum spectrum can be integrated along azimuthal angle ϕ. However, the experimentally measured spectrum is not isotropic; it has some structure. The first idea about this structure comes from the pure geometry of non-central collisions (see Fig. 3.2). Such a collision creates a fireball with an elliptic shape and therefore also an anisotropic pressure gradient. The collective behaviour then leads to an azimuthal anisotropy of the final-state particles measured in the detectors. Measuring this elliptic flow, therefore, serves as a test for the collective behaviour of the hot matter [63].

Generally, the azimuthal dependence of the momentum spectrum in an experiment can be a complicated function. This function can be decomposed into Fourier series

$$\frac{\mathrm{d}^3N}{p_T\mathrm{d}p_T\mathrm{dyd}\phi} = \frac{1}{2\pi}\frac{\mathrm{d}^2N}{p_T\mathrm{d}p_T\mathrm{dy}}\left(1 + \sum_{n=1}^{\infty} 2v_n(p_T)\cos\left(n(\phi - \Psi_{RP,n})\right)\right), \tag{3.11}$$

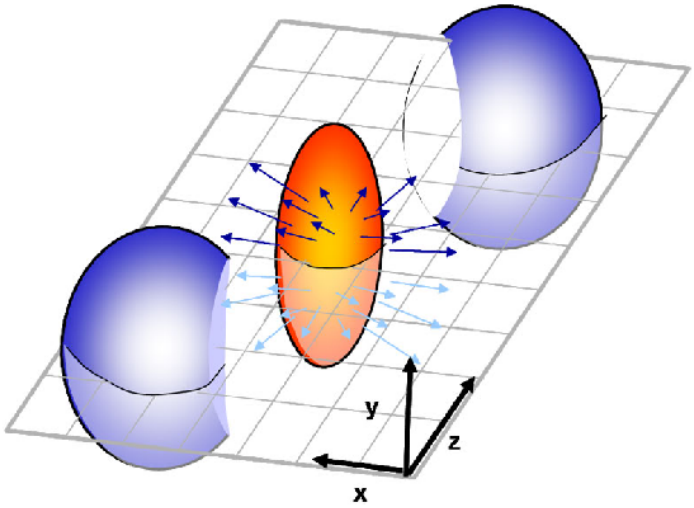

Figure 3.2: Illustration of geometry of non-central heavy-ion collision creating the fireball with elliptic shape. Taken from [64].

where $\Psi_{RP,n}$ is the angle that defines the reaction plane of the n-th order and v_n are the flow coefficients that characterize the momentum anisotropy. In theory and simulations, the reaction plane denotes a plane that is given by the impact vector $\vec{b}$ and the direction of the beam, which in simulations are usually aligned as the axes x and z. In the experiment, the impact vector is not known and therefore the reaction plane is estimated from the azimuthal spectrum (3.11). Moreover, from the azimuthal spectrum one can define also higher-order reaction planes. The flow coefficients can be expressed as

$$v_n(p_T) = \frac{\int_0^{2\pi} \frac{\mathrm{d}^3N}{p_T \mathrm{d}p_T \mathrm{d}y \mathrm{d}\phi} \cos\left(n(\phi - \psi_n)\right) \mathrm{d}\phi}{\int_0^{2\pi} \frac{\mathrm{d}^3N}{p_T \mathrm{d}p_T \mathrm{d}y \mathrm{d}\phi} \mathrm{d}\phi} \equiv \langle \cos\left(n(\phi - \psi_n)\right) \rangle, \tag{3.12}$$

where ψ_n is the angle that characterizes rotation of the n-th harmonic component with respect to the reaction plane. The p_T dependent v_n is called a differential flow. The integrated flow is defined as

$$v_n \equiv \frac{\int_0^{\infty} v_n(p_T) \frac{\mathrm{d}N}{\mathrm{d}p_T} \mathrm{d}p_T}{\int_0^{\infty} \frac{\mathrm{d}N}{\mathrm{d}p_T} \mathrm{d}p_T}. \tag{3.13}$$

The first flow coefficient v_1 is called directed flow. The directed flow describes an increase in hadron production in one direction and a decrease in production in the opposite direction. From the symmetry of the collision at midrapidity, this coefficient should be equal to zero[1]. The situation is more complicated at finite rapidity. Particles produced with some longitudinal velocity are interacting with spectators, which causes them to deflect and create non-zero

[1] Even at midrapidity the directed flow is not exactly zero due to the initial state fluctuations, but it is lower than 0.01 [65].

directed flow. Furthermore, particles with positive and negative rapidities are deflected in opposite directions, which means $v_1(\mathrm{y}) \approx -v_1(-\mathrm{y})$ (see Fig. 3.3).

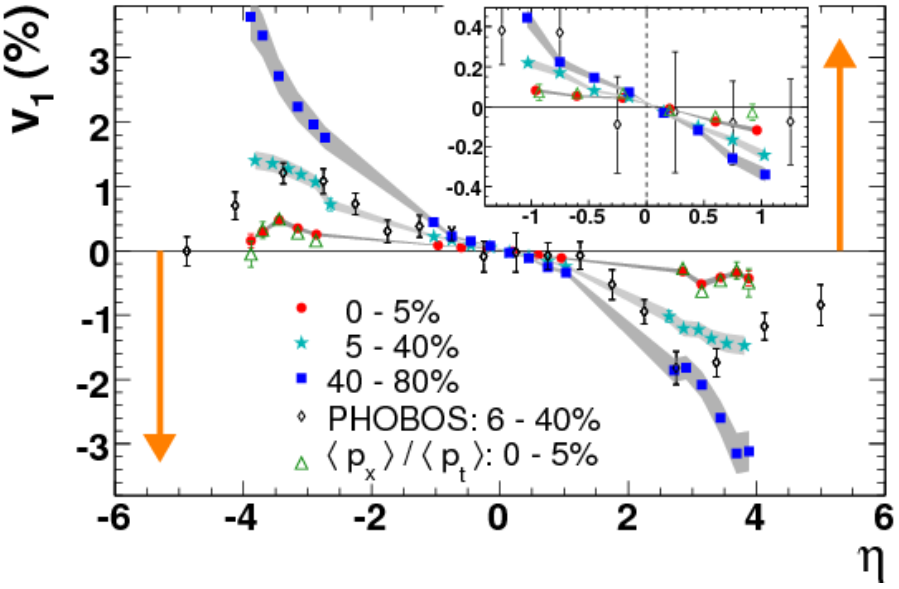

Figure 3.3: The directed flow of charged particles measured in Au+Au collisions at $\sqrt{s_{\mathrm{NN}}} = 200$ GeV by experiment STAR. Taken from [65].

The second flow coefficient v_2 is called the elliptic flow. As was already mentioned, this coefficient's origin is in the geometry of non-central collisions. However, it can also be measured in the most central collisions. The origin of the elliptic flow in the central collision is not geometry anymore, but rather fluctuations of the IS nucleons.

Experimental measurements of the elliptic flow at RHIC [66] confirmed the large v_2 predicted by ideal hydrodynamics. This was used as a signature of the early thermalization of the system and the presence of the strongly interacting QGP.

The third flow coefficient v_3 is called a triangular flow. This and odd higher-order coefficients are results of initial state fluctuations (see Fig. 3.4). This means that simulations with an averaged initial state produce zero odd higher-order flow coefficients because of the symmetry of the collision. To reproduce experimentally measured higher-order coefficients in a hydrodynamic model, one has to use an event-by-event model with fluctuating initial conditions. Triangular flow started to be studied only during the last decade [67].

An important note is that in the initial state the anisotropy is in the geometrical space, whereas in the final state the momentum distribution is anisotropic. Moreover, particle production is higher in the direction where the ellipse is narrower because of a higher pressure gradient. This means that the dynamical evolution of QGP converts geometric anisotropy into momentum anisotropy,

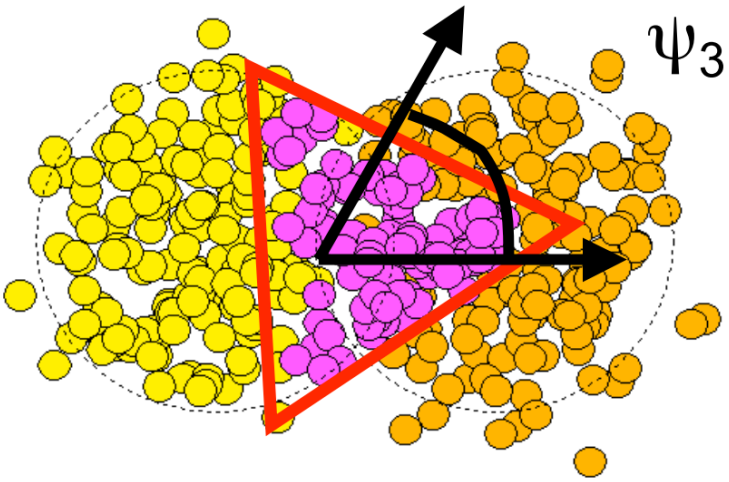

Figure 3.4: Illustration of origin of higher order flow coefficients in heavy-ion collisions from initial state fluctuations in Glauber Monte Carlo model. Taken from [67].

which leads to correlations between the initial state eccentricities and the final state flow coefficients [68].

In the hydrodynamic simulation, the reaction plane is known, and thus it is easy to calculate the elliptic flow. However, in the experiment, the reaction plane has to be determined by some analysis method. To better reproduce the experimental data, it is useful to use the same analysis methods in the simulations. Several methods can be used to calculate flow coefficients from experimental or simulated data. The next sections describe two of these methods: the event-plane (EP) method and the multi-particle cumulants method.

3.4.1 Event-Plane Method

The event-plane method [69] first calculates an estimate of the reaction plane, which is called an event plane. This is done using an event flow vector

$$\vec{Q}_n = \sum_{i=1}^{M} (p_{Ti} \cos(n\phi_i), p_{Ti} \sin(n\phi_i)), \tag{3.14}$$

where M is the multiplicity of the event. The event plane angle is then

$$\psi_n = \frac{\arctan(Q_{n,y}/Q_{n,x})}{n}. \tag{3.15}$$

Then the method calculates the so-called observed flow v_n^{obs} with respect to this event plane

$$v_n^{\text{obs}} = \langle\langle \cos\left(n(\phi - \psi_n)\right)\rangle\rangle_{\text{events}}. \tag{3.16}$$

The mean values denote averaging first over particles in each event and then over all events. One has to be careful to take care of the auto-correlation effect [70]. To do so, the particle being accounted for in the observed flow has to be subtracted from the flow vector, and the event plane angle has to be recalculated.

Due to the limited number of particles in the event, the angle of the event plane has finite resolution. The flow coefficients with respect to the real reaction plane are then

$$v_n = \frac{v_n^{\mathsf{obs}}}{R_n}, \tag{3.17}$$

where R_n is the resolution given by

$$R_n = \langle \mathsf{cos}(n(\psi_n - \psi_n^{\mathsf{R}}))\rangle. \tag{3.18}$$

Here, ψ_n^{R} is the real reaction plane angle. Since it is not known in the experiment, the resolution is determined using the sub-events method. The particles in each event are randomly divided into two sub-events, A and B, and the event plane angles are calculated for each sub-event. The resolution for each of the sub-events is then calculated as

$$R_n^{\mathsf{sub}} = \sqrt{\langle \mathsf{cos}(n(\psi_n^A - \psi_n^{\mathsf{R}}))\rangle\langle \mathsf{cos}(n(\psi_n^B - \psi_n^{\mathsf{R}}))\rangle} = \sqrt{\langle \mathsf{cos}(n(\psi_n^A - \psi_n^B))\rangle}. \tag{3.19}$$

Considering the Gaussian distribution of fluctuations from the real event plane, the resolution can be written as

$$R_n = \frac{\sqrt{\pi}}{2\sqrt{2}}\chi_n \,\mathsf{exp}(-\chi_n^2/4)\left(I_0(\chi_n^2/4) + I_1(\chi_n^2/4)\right), \tag{3.20}$$

where $\chi_n \propto \sqrt{N}$ is the resolution parameter and I_0 and I_1 are modified Bessel functions. Since R_n^{sub} is already calculated and the full event contains twice more particles than sub-events, one can numerically calculate χ_n^{sub} and the full resolution is then calculated by substituting $\sqrt{2}\chi_n^{\mathsf{sub}}$ into Eq. (3.20).

3.4.2 Multi-particle Cumulants Method

The multi-particle cumulant method [71] uses azimuthal correlations between particles to calculate the anisotropic flow. The 2-particle azimuthal correlator can be written as

$$\langle \mathsf{cos}(n(\phi_1 - \phi_2))\rangle = \langle e^{in(\phi_1 - \phi_2)}\rangle = \langle v_n^2\rangle + \delta_n, \tag{3.21}$$

where v_n corresponds to anisotropic flow and δ_n is the contribution not related to the initial-state geometry, which is called non-flow contribution.

To obtain the correlator in Eq. (3.21), one needs to calculate the mean value over all possible pairs of particles. The four-particle correlator requires the calculation of the mean value over all possible four-particle combinations. This would consume enormous computing power. Therefore, it was suggested [72] to calculate the correlations using the flow vector. Unlike the EP method, the flow vector used in this method does not include the weight by the transverse momentum:

$$\vec{Q}_n = \sum_{i=1}^{M}(\cos(n\phi_i), \sin(n\phi_i)) = \sum_{i=1}^{M} e^{in\phi_i}. \tag{3.22}$$

The definitions of 2- and 4-particle azimuthal correlations in single event are

$$\langle 2\rangle \equiv \langle e^{in(\phi_1-\phi_2)}\rangle \equiv \frac{(M-2)!}{M!}\sum_{\substack{i,j=1\\ i\neq j}}^{M} e^{in(\phi_i-\phi_j)}, \tag{3.23a}$$

$$\langle 4\rangle \equiv \langle e^{in(\phi_1+\phi_2-\phi_3-\phi_4)}\rangle \equiv \frac{(M-4)!}{M!}\sum_{\substack{i,j,k,l=1\\ i\neq j\neq k\neq l}}^{M} e^{in(\phi_i+\phi_j-\phi_k-\phi_l)}. \tag{3.23b}$$

The conditions below sums denote that all indices must be different for each element of the sum. Analogously, one can define even higher-order particle correlations.

To obtain the correlations directly from the flow vector, one needs to express respective power of the magnitude of the flow vector. For the second-order cumulant, it is

$$|Q_n|^2 = \sum_{i,j=1}^{M} e^{in(\phi_i-\phi_j)} = M + \sum_{\substack{i,j=1\\ i\neq j}}^{M} e^{in(\phi_i-\phi_j)}. \tag{3.24}$$

From this equation, the 2-particle correlation can be written as

$$\langle 2\rangle = \frac{|Q_n|^2 - M}{M(M-1)}. \tag{3.25}$$

Analogously, for the 4-particle correlation one obtains

$$\langle 4\rangle = \frac{|Q_n|^4 + |Q_{2n}|^2 - 2\mathfrak{Re}|Q_{2n}Q_n^*Q_n^*| - 4(M-2)|Q_n|^2 - 2M(M-3)}{M(M-1)(M-2)(M-3)}. \tag{3.26}$$

The event-averaged correlations are defined as

$$\langle\langle 2\rangle\rangle \equiv \langle\langle e^{in(\phi_1-\phi_2)}\rangle\rangle \equiv \frac{\sum_{\text{events}} W_{2,i}\langle 2\rangle_i}{\sum_{\text{events}} W_{2,i}}, \tag{3.27a}$$

$$\langle\langle 4\rangle\rangle \equiv \langle\langle e^{in(\phi_1+\phi_2-\phi_3-\phi_4)}\rangle\rangle \equiv \frac{\sum_{\text{events}} W_{4,i}\langle 4\rangle_i}{\sum_{\text{events}} W_{4,i}}, \tag{3.27b}$$

where the weights are given by the number of combinations in the event with multiplicity M

$$W_2 = M(M-1), \tag{3.28a}$$

$$W_4 = M(M-1)(M-2)(M-3). \tag{3.28b}$$

The second- and fourth-order cumulants are then defined as

$$c_n\{2\} = \langle\langle 2\rangle\rangle, \tag{3.29a}$$

$$c_n\{4\} = \langle\langle 4\rangle\rangle - 2\cdot\langle\langle 2\rangle\rangle^2. \tag{3.29b}$$

The integrated anisotropic flow can be calculated using cumulants of different order

$$v_n\{2\} = \sqrt{c_n\{2\}}, \tag{3.30a}$$

$$v_n\{4\} = \sqrt[4]{-c_n\{4\}}. \tag{3.30b}$$

It is important to note that these two equations calculate the same coefficient v_n, but they use cumulants of different order to do it.

To obtain the differential flow (e.g. the flow as a function of transverse momentum), the procedure is more complicated. First, the reduced 2- and 4-particle azimuthal correlations are defined:

$$\langle\langle 2'\rangle\rangle \equiv \langle\langle e^{in(\psi_1-\phi_2)}\rangle\rangle \equiv \frac{1}{m(M-1)}\sum_{i=1}^{m}\sum_{j=1}^{M} e^{in(\psi_i-\phi_j)}, \tag{3.31a}$$

$$\begin{aligned}\langle\langle 4'\rangle\rangle &\equiv \langle\langle e^{in(\psi_1+\phi_2-\phi_3-\phi_4)}\rangle\rangle \equiv \\ &\equiv \frac{1}{m(M-1)(M-2)(M-3)}\sum_{i=1}^{m}\sum_{j,k,l=1}^{M} e^{in(\psi_i+\phi_j-\phi_k-\phi_l)},\end{aligned} \tag{3.31b}$$

where m is the number of particles with transverse momentum (or rapidity) in the interval of interest and ψ_i is the azimuthal angle of such a particle. Since the particles of interest are a subset of all particles, they are in both sums. Again, each element of the sum must contain all different particles.

Once again, these correlations can be expressed using the flow vector. But now also a flow vector composed only of particles of interest is needed

$$q_n = \sum_{i=1}^{m} e^{in\psi_i}. \tag{3.32}$$

Using this q-vector, the 2- and 4-particle azimuthal correlations can be calculated as

$$\langle\langle 2'\rangle\rangle = \frac{q_n Q_n^* - m}{m(M-1)}, \tag{3.33a}$$

$$\begin{aligned}\langle\langle 4'\rangle\rangle =& \big[q_n Q_n Q_n^* Q_n^* - q_{2n} Q_n^* Q_n^* - q_n Q_n Q_{2n}^* - 2m|Q_n|^2 + (9-2M) q_n Q_n^* - \\ &- Q_n q_n^* + q_{2n} Q_{2n}^* + 2m(M-3)\big]\cdot\big[m(M-1)(M-2)(M-3)\big]^{-1}.\end{aligned} \tag{3.33b}$$

Analogously, the event-averaged correlations are as follows

$$\langle\langle 2'\rangle\rangle = \frac{\sum_{\text{events}} w_{2',i}\langle 2'\rangle_i}{\sum_{\text{events}} w_{2',i}}, \tag{3.34a}$$

$$\langle\langle 4'\rangle\rangle = \frac{\sum_{\text{events}} w_{4',i}\langle 4'\rangle_i}{\sum_{\text{events}} w_{4',i}}, \tag{3.34b}$$

where the weights are defined as

$$w_{2'} = m(M-1), \tag{3.35a}$$

$$w_{4'} = m(M-1)(M-2)(M-3). \tag{3.35b}$$

All of this leads to differential second- and fourth-order cumulants:

$$d_n\{2\} = \langle\langle 2'\rangle\rangle, \tag{3.36a}$$

$$d_n\{4\} = \langle\langle 4'\rangle\rangle - 2\cdot\langle\langle 2'\rangle\rangle\langle\langle 2\rangle\rangle. \tag{3.36b}$$

Finally, the differential flow at a given interval of interest is given by

$$v_n'\{2\} = \frac{d_n\{2\}}{\sqrt{c_n\{2\}}}, \tag{3.37a}$$

$$v_n'\{4\} = -\frac{d_n\{4\}}{(-c_n\{4\})^{3/4}}. \tag{3.37b}$$

A detailed derivation of these equations can be found in [71].

3.4.3 Comparison of Both Methods

Both EP and the cumulant methods are biased by non-flow correlations. The non-flow effects include quantum statistics effects, resonance decays, momentum conservation, jets, strong and Coulomb interactions, and so on. These effects can be mistaken for correlations caused by anisotropic flow. A simple way to deal with the non-flow correlations is to compute their effect and subtract it to isolate the anisotropic flow. However, one cannot be sure to know all sources of non-flow correlations. A better way is to use the four-particle cumulant method, where the bias from the non-flow effects is smaller than at the two-particle level. On the other hand, the statistical uncertainty increases with higher-order cumulants.

Figure 3.5 shows the comparison of both methods in the results from STAR at BES energies [73]. These plots confirm that the 4-particle cumulant method has the largest statistical uncertainties, but also produces lower elliptic flow, freed from non-flow correlations. The same paper also shows v_2 as a function of transverse momentum, centrality, and pseudorapidity for the energies $\sqrt{s_{\text{NN}}} = 7.7, 11.5, 19.6, 27$ and 39 GeV.

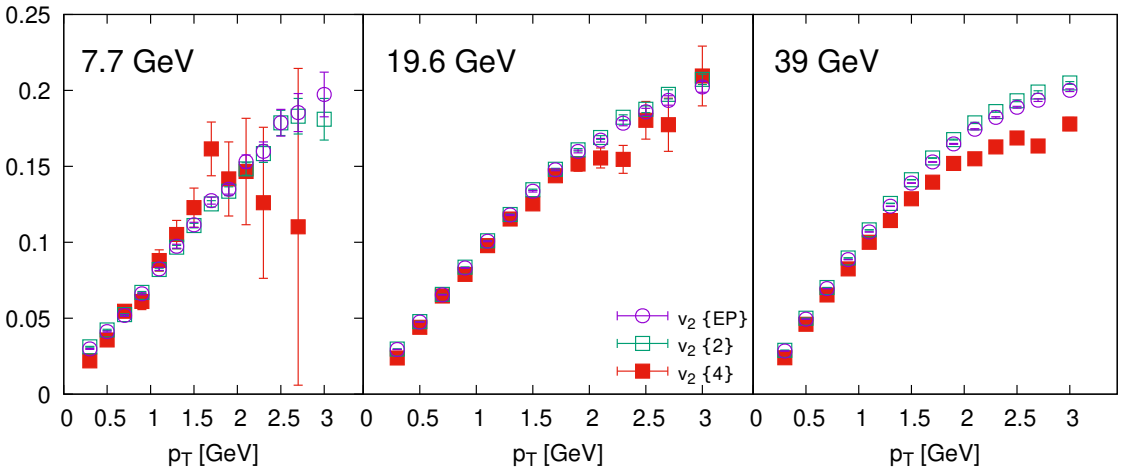

Figure 3.5: Comparison of event-plane method, 2- and 4-particle cumulant methods for calculating elliptic flow in Au+Au collisions at $\sqrt{s_{\mathrm{NN}}} = 7.7, 19.6$ and 39 GeV at centrality $20 - 30$% measured by STAR experiment. The data are taken from [73].

3.5 Correlations

Correlations between produced hadrons are a very important probe of the hot matter. Conservation laws, symmetrization of the wave functions, interactions between particles, or Bose-Einstein statistics, all these effects take place during the evolution of the hot matter and create correlations between particles measured in detectors. Therefore, studying correlations can bring new information about the properties of the hot matter. A long-established method of studying pion correlations caused mainly by Bose-Einstein statistics to measure the size of the homogeneity region in the hot matter is called femtoscopy, or HBT interferometry, developed by Hanbury-Brown and Twiss (HBT) [74, 75]. The multi-particle cumulant method described in Sec. 3.4.2 uses correlations in the transverse plane to calculate anisotropic flow. This section outlines the lesser-used correlations of anisotropic flow in the longitudinal direction. Studying the longitudinal structure of the anisotropic flow can help to understand the transport properties of the hot matter [76].

Due to the symmetry, one could assume that the flow should be fully correlated along the longitudinal direction. In other words, the flow at η and $-\eta$ should be the same. In reality, the interactions in collision may cause the decorrelation of the anisotropic flow. This decorrelation using the factorization ratio defined as

$$r_n(\eta) = \frac{\langle q_n(-\eta) q_n^*(\eta_{\mathrm{ref}}) \rangle}{\langle q_n(\eta) q_n^*(\eta_{\mathrm{ref}}) \rangle}. \tag{3.38}$$

This factorization ratio calculates the ratio of correlations of the flow vector q_n between the reference bin η_{ref} and $\pm\eta$. The brackets $\langle \dots \rangle$ denote the averaging over events. This is illustrated in Fig. 3.6. The flow vector is calculated using only particles in the examined pseudorapidity interval

$$q_n(\eta) = \frac{1}{m}\sum_{i=1}^{m} e^{in\phi_i}. \tag{3.39}$$

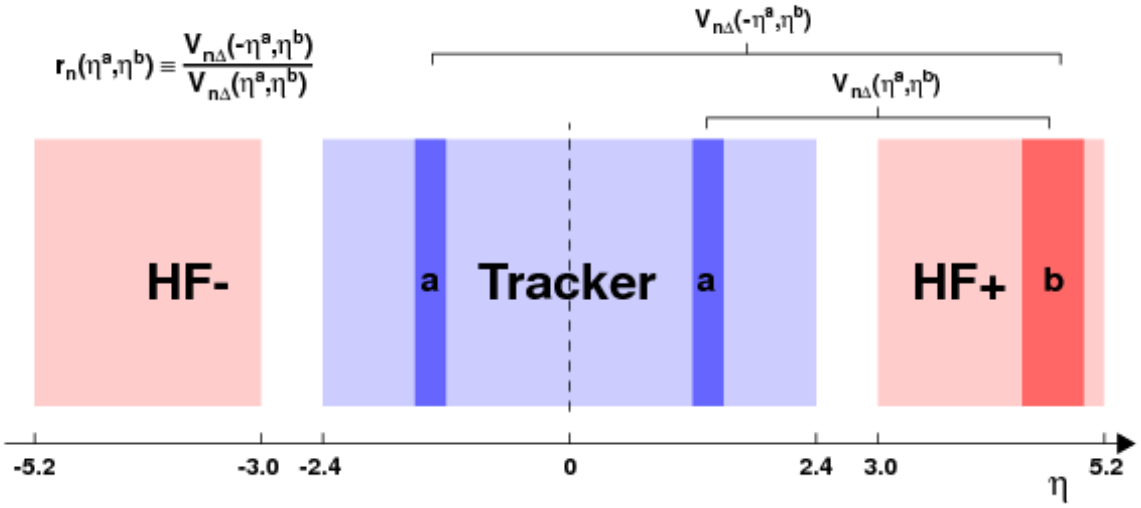

Figure 3.6: The scheme of the experimental measurement of the longitudinal decorrelation of anisotropic flow. Taken from [77].

The flow vector can be rewritten as

$$q_n(\eta) = v_n(\eta)e^{in\psi_n(\eta)}. \tag{3.40}$$

Using this equation, the factorization ratio can be rewritten as

$$r_n(\eta) = \frac{\langle v_n(-\eta)v_n(\eta_{\text{ref}})\cos[n(\psi_n(-\eta) - \psi_n(\eta_{\text{ref}}))]\rangle}{\langle v_n(\eta)v_n(\eta_{\text{ref}})\cos[n(\psi_n(\eta) - \psi_n(\eta_{\text{ref}}))]\rangle}. \tag{3.41}$$

This equation demonstrates, that the decorrelation may be caused either by the flow magnitude v_n decorrelation or the flow angle ψ_n decorrelation. The illustration of these two types of decorrelation is shown in Fig. 3.7. To study these effects individually, one can define the magnitude and angle factorization ratios:

$$r_n^v(\eta) = \frac{\langle v_n(-\eta)v_n(\eta_{\text{ref}})\rangle}{\langle v_n(\eta)v_n(\eta_{\text{ref}})\rangle}, \tag{3.42a}$$

$$r_n^\psi(\eta) = \frac{\langle \cos[n(\psi_n(-\eta) - \psi_n(\eta_{\text{ref}}))]\rangle}{\langle \cos[n(\psi_n(\eta) - \psi_n(\eta_{\text{ref}}))]\rangle}. \tag{3.42b}$$

To date, longitudinal decorrelation measurements have been published only at LHC energies [77, 79, 80]. However, preliminary results from STAR have been published showing the longitudinal decorrelation at BES energies [81, 82].

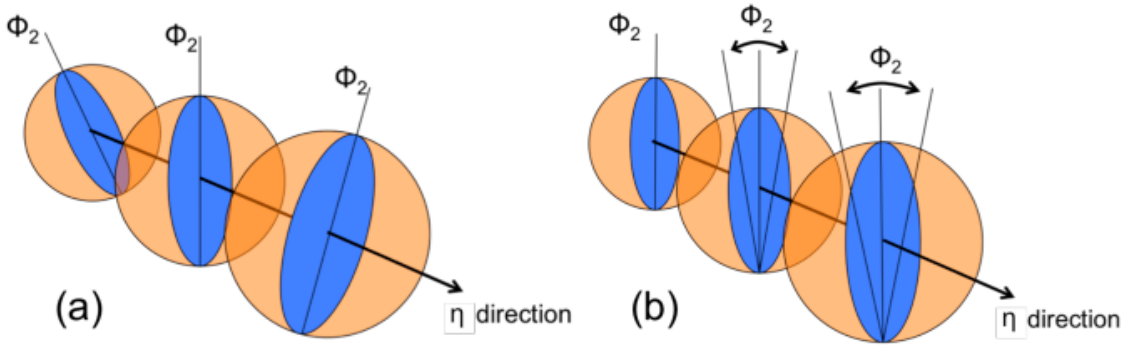

Figure 3.7: Two possible origins for flow decorrelation - decorrelation of the flow magnitude (a) and decorrelation of the flow angle (b). Taken from [78].

Chapter 4

Fluid Dynamical Description of QGP

Relativistic hydrodynamics has been used to describe QGP in heavy-ion collisions since the 1950s. The first work, in which the particle production was predicted, was done by Landau [1]. His work was based on the pre-hydrodynamic Fermi statistical model [83, 84]. The Landau model is a perfect-fluid model in which the matter after collision creates a compressed disk. This disk then undergoes a one-dimensional expansion along the collision axis according to the fluid equations.

However, the Landau model misses the fact that in high-energy collisions fast particles are produced later and further away from the collision center. Bjorken tried to solve this by introducing special initial conditions [2]. This has led to the assumption that the hydrodynamic expansion is longitudinally boost-invariant. The Bjorken model is also a perfect-fluid model.

It is generally considered that the Landau model works better for low-energy collisions, while the Bjorken model produces better results for the high-energy collision.

4.1 Hydrodynamic Equations of Motion

The hydrodynamic equations are formulated in terms of the energy-momentum tensor $T^{\mu\nu}$. The energy-momentum tensor for a perfect fluid in the local rest-frame is given by

$$T^{\mu\nu} = \mathrm{diag}(\varepsilon, P, P, P), \tag{4.1}$$

where ε is the energy density and P is the pressure. In the global frame, the fluid cell moves with four-velocity u^μ and so in local equilibrium, the energy-momentum tensor has a form

$$T^{\mu\nu}_{eq} = (\varepsilon + P)u^\mu u^\nu - P g^{\mu\nu}, \tag{4.2}$$

where $g^{\mu\nu}$ is the metric tensor. The equations of motion are then hidden by the conservation laws

$$\partial_\mu T^{\mu\nu}_{eq} = 0. \tag{4.3}$$

In order to extract the equations of motion, it is necessary to project the Eqs. (4.3) in the direction parallel and perpendicular to u^μ. The former projection is given by

$$u_\nu \partial_\mu T^{\mu\nu}_{eq} = \partial_\mu(\varepsilon + P)u^\mu - u^\mu \partial_\mu P = u^\mu \partial_\mu \varepsilon + (\varepsilon + P)\partial_\mu u^\mu \overset{!}{=} 0. \tag{4.4}$$

The latter projection can be obtained by acting with the operator $\Delta^{\mu\nu} = g^{\mu\nu} - u^\mu u^\nu$, which projects on the space orthogonal to u^μ:

$$\Delta^\alpha{}_\nu \partial_\mu T^{\mu\nu}_{eq} = \Delta^\alpha{}_\nu (\varepsilon + P)u^\mu \partial_\mu u^\nu - \Delta^{\mu\alpha}\partial_\mu P = (\varepsilon + P)u^\mu \partial_\mu u^\alpha - \Delta^{\mu\alpha}\partial_\mu P \overset{!}{=} 0. \tag{4.5}$$

At this point, shorthand notation is usually introduced

$$D \equiv u^\mu \partial_\mu, \tag{4.6a}$$

$$\nabla^\nu \equiv \Delta^{\mu\nu}\partial_\mu. \tag{4.6b}$$

The equations of motion for a relativistic perfect fluid then take the form

$$D\varepsilon + (\varepsilon + P)\partial_\mu u^\mu = 0, \tag{4.7a}$$

$$(\varepsilon + P)Du^\alpha - \nabla^\alpha P = 0. \tag{4.7b}$$

4.2 Viscous Hydrodynamics

4.2.1 The Relativistic Navier-Stokes Equation

Since QGP is not a perfect fluid, it is necessary to add a dissipative term $\Pi^{\mu\nu}$ to the energy-momentum tensor

$$T^{\mu\nu} = T^{\mu\nu}_{eq} + \Pi^{\mu\nu}. \tag{4.8}$$

The dissipative term is usually decomposed as

$$\Pi^{\mu\nu} = \pi^{\mu\nu} + \Pi\Delta^{\mu\nu}, \tag{4.9}$$

where Π is the bulk viscous pressure and $\pi^{\mu\nu}$ is the shear stress tensor, which is traceless, symmetric, and orthogonal to u^μ. The bulk pressure is according to the Navier-Stokes theory proportional to the divergence of the flow vector

$$\Pi = -\zeta \partial_\mu u^\mu, \tag{4.10}$$

where ζ is the bulk viscosity coefficient. The same is true for the shear stress tensor

$$\pi^{\mu\nu} = 2\eta\sigma^{\mu\nu}, \tag{4.11}$$

where η is the shear viscosity coefficient and $\sigma^{\mu\nu}$ is the shear flow tensor given by

$$\sigma^{\mu\nu} = \Delta^{\mu\nu}_{\alpha\beta}\partial^{\alpha}u^{\beta}. \tag{4.12}$$

Here, the projection operator $\Delta^{\mu\nu}_{\alpha\beta}$ is

$$\Delta^{\mu\nu}_{\alpha\beta} = \frac{1}{2}\left(\Delta^{\mu}{}_{\alpha}\Delta^{\nu}{}_{\beta} + \Delta^{\mu}{}_{\beta}\Delta^{\nu}{}_{\alpha}\right) - \frac{1}{3}\Delta^{\mu\nu}\Delta_{\alpha\beta}. \tag{4.13}$$

The full energy-momentum tensor can then be written as

$$T^{\mu\nu} = (\varepsilon + P)u^{\mu}u^{\nu} - Pg^{\mu\nu} + 2\eta\sigma^{\mu\nu} - \zeta\Delta^{\mu\nu}\partial_{\alpha}u^{\alpha}, \tag{4.14}$$

which can be considered as an expansion of the tensor to terms of the first order in gradients of u^{μ}.

4.2.2 Müller-Israel-Stewart Theory

The definition of the bulk pressure and the shear stress tensor according to the Navier-Stokes theory leads to parabolic differential equations and an infinite speed of propagation of the signal, which is in contradiction with the principle of causality. This problem was solved by Müller, Israel, and Stewart [85–87] by promoting the bulk pressure and the shear stress tensor to independent dynamic variables. These variables are governed by two differential equations

$$D\Pi + \frac{\Pi}{\tau_{\Pi}} = -\beta_{\Pi}\partial_{\alpha}u^{\alpha}, \tag{4.15a}$$

$$D\Delta^{\mu\nu}_{\alpha\beta}\pi^{\alpha\beta} + \frac{\pi^{\mu\nu}}{\tau_{\pi}} = 2\beta_{\pi}\sigma^{\mu\nu}. \tag{4.15b}$$

Parameters τ_{Π} and τ_{π} are relaxation times, and coefficients β_{Π} and β_{π} must satisfy $\eta = \beta_{\pi}\tau_{\pi}$ and $\zeta = \beta_{\Pi}\tau_{\Pi}$. The hydrodynamic models used to describe heavy-ion collisions actually use a form of these equations with additional terms, which are chosen so that the second law of thermodynamics is fulfilled, specifically [88]

$$D\Pi = -\frac{1}{\tau_{\Pi}}\left[\Pi + \zeta\partial_{\alpha}u^{\alpha} + \Pi\zeta T\partial_{\mu}\left(\frac{\tau_{\Pi}u^{\mu}}{2\zeta T}\right)\right], \tag{4.16a}$$

$$D\Delta^{\mu\nu}_{\alpha\beta}\pi^{\alpha\beta} = -\frac{1}{\tau_{\pi}}\left[\pi^{\mu\nu} - 2\eta\sigma^{\mu\nu} + \pi^{\mu\nu}\eta T\partial_{\lambda}\left(\frac{\tau_{\pi}u^{\lambda}}{2\eta T}\right)\right]. \tag{4.16b}$$

4.2.3 Limits of the Shear Viscosity

One of the most interesting results of viscous hydrodynamics is certainly the phenomenological extraction of the shear viscosity from the experimental data. The first estimate of the shear viscosity over entropy density ratio η/s was made based on the anti-de-Sitter/conformal field theory (AdS/CFT) [89] and led to the limit

$$\frac{\eta}{s} \geq \frac{1}{4\pi}. \tag{4.17}$$

The viscous hydrodynamic simulations were successful in describing the bulk evolution of heavy-ion collisions and also the elliptic flow data from LHC. Comparison of the phenomenological simulation with precise experimental measurements leads to even tighter limits on the shear viscosity. The results from 2012 [3] found that the shear viscosity limits are given by

$$\frac{1}{4\pi} < \left(\frac{\eta}{s}\right)_{\text{QGP}} < \frac{2.5}{4\pi}. \tag{4.18}$$

This result indicates that although QGP is an imperfect fluid, it is the most perfect fluid in the universe [90]. Due to the increasing precision of models and measurements, current results include the temperature dependence of the limits of η/s and ζ/s [91, 92]. The timeline of the boundaries for the ratio η/s is shown in Figure 4.1. The Figure 4.2 shows the comparison of the fluid imperfection, defined as the specific shear viscosity η/s normalized by factor $\frac{1}{4\pi}\frac{\hbar}{k_B}$, as a function of the temperature for four different physical systems.

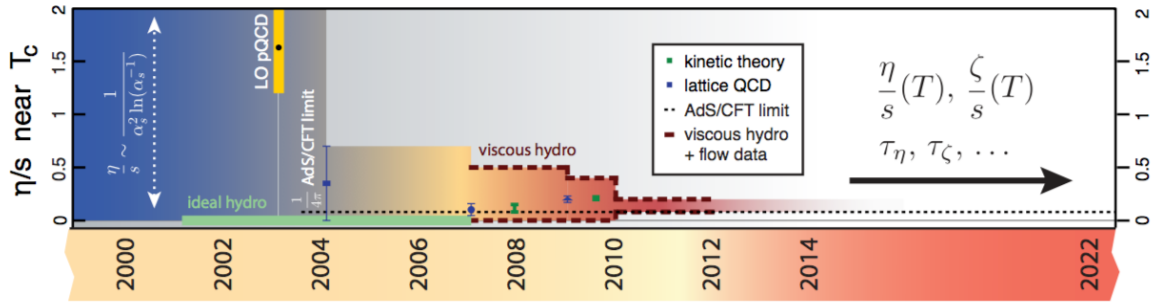

Figure 4.1: Timeline of increasing the precision of the shear viscosity to entropy density ratio. Taken from [93].

4.3 An Overview of Hydrodynamic Models

There are several hydrodynamic models currently used to calculate various predictions of different observables. Older models based on ideal hydrodynamics include, for example, the model by Heinz and Kolb [94], model using

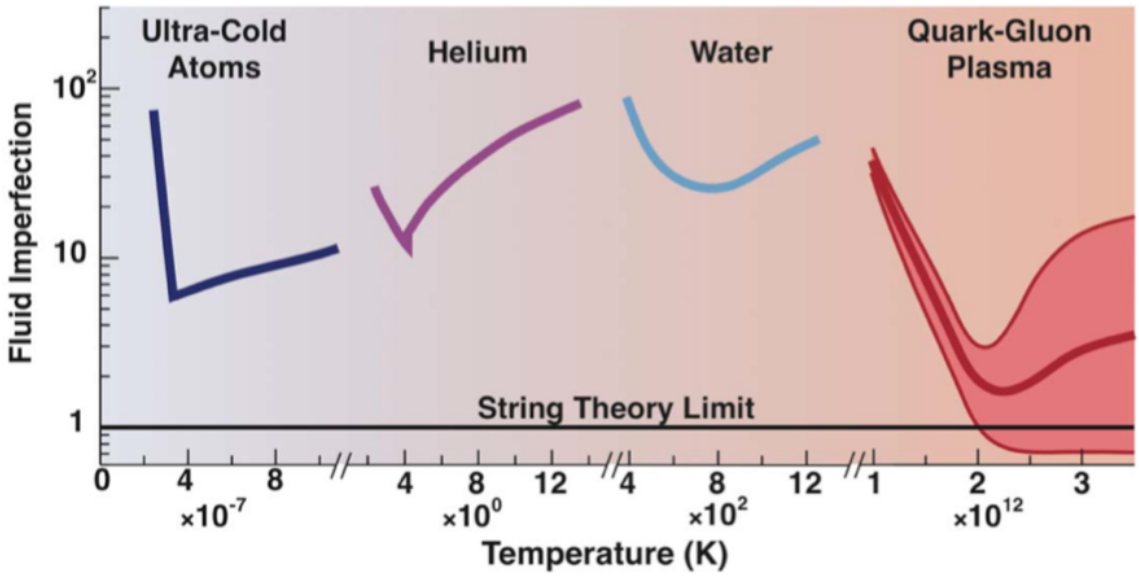

Figure 4.2: The comparison of the fluid imperfection of various fluids as a function of the temperature. The figure shows that the QGP is the most perfect fluid. Taken from [93].

Sharp And Smooth Transport Algorithm (SHASTA) by Rischke [95, 96], Hirano [97, 98], or Nonaka [99]. Andrade et al. created a hydrodynamic code NeXSPheRIO [9] by merging NeXus [100], which computes the initial conditions, and SPheRIO, which computes the hydrodynamic evolution based on Smoothed Particle Hydrodynamics (SPH). Ivanov [101] developed ideal 3-fluid hydrodynamic model. From the newer models, the notable one is Schenke's model MUSCl for Ion Collisions (MUSIC) [4], which uses the Kurganov-Tadmor algorithm for relativistic (3+1)-dimensional fluid dynamics, and was later extended to include viscosity [102]. Other viscous hydrodynamic models were developed by Romatschke [103], or Song and Heinz [104]. Pang and Petersen developed the code CLVisc [6], which uses the A Multi-Phase Transport (AMPT) model [105] for initial conditions and the Cooper-Frye formula for freeze-out. Noronha-Hostler et al. developed a 2+1 Lagrangian hydrodynamic code called viscous Ultrarelativistic Smoothed Particle hydrodynamics (v-USPhydro) [8], which solves hydrodynamic equations using the SPH Lagrangian algorithm [106]. The new conceptual development called HYDRO+ [12], which extends the hydrodynamics with a parametric slowing down, is also interesting.

During the last decade, scientists have been developing hybrid models, which combine the Monte Carlo fluctuating initial state and the fluid dynamical evolution of hot and dense matter. This combination allows event-by-event hydrodynamic simulations to be performed. Shen et al. created the model Event-

By-Event Viscous Israel Stewart Hydrodynamics aNd UrQMD (iEBE-VISHNU) [5], which uses a Monte Carlo generator called superMC for initial conditions, VISHN [104] for (2+1)-dimensional viscous hydrodynamics, hadron sampler called iSS for Cooper-Frye freeze-out [107] and hadron cascade from Ultra relativistic Quantum Molecular Dynamics (UrQMD) [108, 109]. Karpenko uses UrQMD for the initial state and the hadron cascade and viscous Harten–Lax–van Leer–Einfeldt (vHLLE) [110] for the hot and dense stage [7]. Bożek in [10] uses GLauber Initial-State Simulation AND mOre (GLISSANDO) [111] for the initial conditions to (3+1)-dimensional viscous hydrodynamics and THERMal heavy IoN generATOR version 2 (THERMINATOR2) [112] for particle emission and resonance decay. Werner et al. [11] apply the flux tube approach (EPOS) for the initial state in ideal hybrid model. Karpenko and Sinyukov modified an ideal hydro-kinetic model (HKM) [113] to include resonance decays and calculate local EoS [114].

Chapter 5

Preliminary Studies of the Initial Conditions in Hybrid Model

Same hydrodynamic equations are applied to simulate heavy-ion collisions at vastly different collision energies, from few GeV to few TeV. However, the initial state at the BES energies is more complex than at the LHC and top RHIC energies. The complexity of the initial state can be solved using the three-fluid hydrodynamics model [101]. However, an interesting question is whether functionally simple initial state models, based on Glauber picture and developed for LHC and top RHIC energies, could reproduce the basic observables at BES energies. Therefore, we studied how different initial-state models affect basic observables in a 3-dimensional event-by-event viscous hydrodynamic model at energies $\sqrt{s_{\mathrm{NN}}} = 27, 62.4$, and 200 GeV.

5.1 Model

For the study, we used the hybrid model [7] consisting of four stages (Fig. 5.1). In the first stage, initial conditions are generated. For this stage, we used three different models: UrQMD, GLISSANDO 2, and Reduced Thickness Event-by-event Nuclear Topology (TRENTo). In all cases, the transition from the initial state to the hydrodynamic stage takes place at $\tau = \tau_0$. The second stage is the evolution of the QGP performed with the 3-dimensional relativistic viscous hydrodynamic code vHLLE. The third stage is called particlization, and it samples particles from freeze-out hypersurface using the Cooper-Frye formula. The last stage takes care of final-state interactions between particles, such as rescatterings and resonance decays, using the UrQMD cascade. This section describes the individual stages in detail.

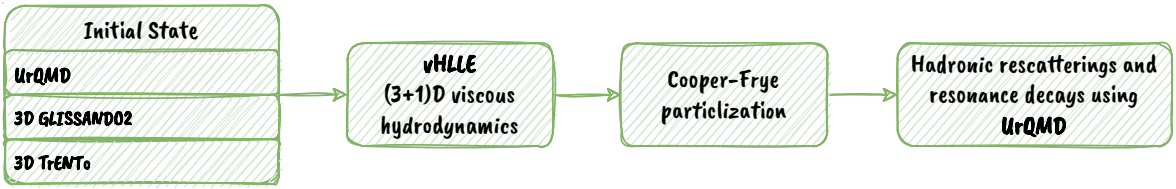

Figure 5.1: Diagram of the hybrid model.

5.1.1 Initial State

`UrQMD`

The `UrQMD` [108] is a microscopic transport model. It uses `PYTHIA6` [115] to simulate the initial nucleon-nucleon scatterings through string formation and subsequent string break-up. This produces hadrons that are able to rescatter. At the proper time $\tau = \tau_0$, the process called hydrodynamization takes place, during which each hadron deposits its energy and momentum into a few neighbouring cells of the hydrodynamic grid with a weight given by the Gaussian distribution

$$w \propto \exp\left(-\frac{(x_h - x_c)^2}{R_T^2} - \frac{(y_h - y_c)^2}{R_T^2} - \gamma^2\tau_0^2\frac{(\eta_{s,h} - \eta_{s,c})^2}{R_\eta^2}\right), \tag{5.1}$$

where the coordinates with subscript h are those of hadrons, the coordinates with subscript c are those of the centre of hydrodynamic cells, and R_T and R_η are widths of the distribution of energy and momentum deposition. The time of hydrodynamization τ_0 depends on the energy of the collision, but its ballpark value is defined by the time for the two nuclei to completely pass through each other

$$\tau_0 = \frac{2R}{\gamma v_z}, \tag{5.2}$$

where γ is the u^0 corresponding to the velocity of the incoming nucleus. The values of the parameters R_T, R_η, and τ_0 were taken from [7]. During hydrodynamization, the hadron coordinates need to be transformed from Cartesian to Milne coordinates, since `UrQMD` uses the former and vHLLE the latter. During all of these processes, energy, momentum, baryon number, and electric charge are conserved.

`GLISSANDO 2`

`GLISSANDO 2` [116] is a Monte Carlo implementation of the Glauber model [117]. The code generates the positions of nucleons in the transverse plane us-

ing the deformed Woods-Saxon formula [118]:

$$\rho(x,y,z) = \frac{\rho_0}{1+\exp\left(\frac{r-R(1+\beta_2 Y_{20}+\beta_4 Y_{40})}{a}\right)}, \tag{5.3}$$

where β_2 and β_4 are the deformation parameters, Y_{20} and Y_{40} are the spherical harmonics, a is the diffuseness, and R is the nuclear radius. For heavy nuclei ($A > 16$), the model calculates the nuclear radius using a function

$$R = \left(1.1A^{1/3} - 0.656A^{-1/3}\right)\,\text{fm} \tag{5.4}$$

and uses the value $a = 0.459\,\text{fm}$. The deformation parameters for gold nucleus are $\beta_2 = -0.13$ and $\beta_4 = -0.03$, the parameters for other nuclei are listed in [119].

Next, the model calculates binary collisions. The participant nucleons are then sources of entropy depositions. The entropy density is distributed according to [120, 121] as:

$$s(x,y,\eta_s) = \kappa \sum_i f_\pm(\eta_s)\left[(1-\alpha) + N_i^{\text{coll}}\alpha\right] \exp\left(-\frac{(x-x_i)^2+(y-y_i)^2}{2\sigma^2}\right), \tag{5.5}$$

where the sum goes through all participant nucleons i, N_i^{coll} is the number of binary collisions of the participant i, $\sigma = 0.4\,\text{fm}$ is the Gaussian smearing width, α is the mixing parameter, and κ is the normalization parameter that ensures that the total energy deposited during the hydrodynamization process will be equal to the total energy of wounded nucleons N_{W}:

$$\tau_0 \int \epsilon \cosh\eta \,\mathrm{d}x\mathrm{d}y\mathrm{d}\eta = \frac{N_{\text{W}}}{2}\sqrt{s_{\text{NN}}}. \tag{5.6}$$

Since the Glauber model provides distributions only in the transverse plane, we extended the model to the longitudinal direction following [120, 121] using functions

$$f_\pm(\eta_s) = \frac{\eta_{\text{M}} \pm \eta_s}{2\eta_{\text{M}}} H(\eta_s) \qquad \text{for } |\eta_s| < \eta_{\text{M}}, \tag{5.7}$$

which create a triangular shape of the entropy deposition of forward ($+$) and backward ($-$) participants. The parameter η_{M} is the parameter of the Bialas-Czyz-Bozek model taken from [116] and the profile function $H(\eta_s)$ is defined as

$$H(\eta_s) = \exp\left(-\frac{(|\eta_s|-\eta_0)^2\Theta(|\eta_s|-\eta_0)}{2\sigma_\eta^2}\right). \tag{5.8}$$

Here, η_0 and σ_η are parameters that describe the shape of the profile and $\Theta(x)$ is the Heaviside step function.

At higher energies, the baryon density may be neglected. However, at energies lower than the top RHIC energy ($\sqrt{s_{\text{NN}}} = 200\,\text{GeV}$) it plays an important

role. Therefore, in addition to entropy, nucleons deposit also their baryon number and electric charge into the fluid. The baryon number deposition is given by the equation

$$n_B(x,y,\eta_s) = \kappa_B \sum_i \exp\left(-\frac{(\eta_B \pm \eta_s)^2}{2\sigma_B^2}\right) \exp\left(-\frac{(x-x_i)^2+(y-y_i)^2}{2\sigma^2}\right), \quad (5.9)$$

where n_B is the baryon density, η_B and σ_B are the profile parameters. This ansatz assumes that forward-going participants deposit their baryon number around space-time rapidity $+\eta_B$ and backward-going participants around $-\eta_B$. The parameter κ_B is the normalization parameter and again checks that the total deposited baryon number is equal to the number of wounded nucleons:

$$\tau_0 \int n_B \mathrm{d}x\mathrm{d}y\mathrm{d}\eta = N_{\mathrm{W}}. \quad (5.10)$$

The electric charge deposition is then simply

$$n_Q = 0.4 n_B, \quad (5.11)$$

following the ratio of protons to nucleons in heavy nuclei. Parameters η_B, σ_B, η_0, σ_η, and η_{M} were obtained by tuning the rapidity distributions and the p_T spectra from simulations against the experimental data [57–59]. Since each hydrodynamic simulation requires a large CPU time, it would be quite time-consuming to obtain χ^2-optimized values of the parameters. Instead, parameters were adjusted based on the visual correspondence with the data. The values of these parameters used in our simulations along with the values of α are listed in Table 5.1.

$\sqrt{s_{\mathrm{NN}}}$ [GeV]	α	η_0	σ_η	η_{M}	η_B	σ_B
27	0.123	$0.89 - 0.2\chi$	$1.09 + 0.2\chi$	1.0	$1.33 - 0.32\chi$	$0.79 - 0.21\chi$
62.4	0.132	1.8	0.7	1.8	2.2	1.0
200	0.145	1.5	1.4	3.36		

Table 5.1: Default values of the parameters of the GLISSANDO model: mixing parameter and parameters for the longitudinal profile for $\sqrt{s_{\mathrm{NN}}} = 27$, 62.4 and 200 GeV. At $\sqrt{s_{\mathrm{NN}}} = 27$ GeV the tuning process resulted in centrality-dependent values of the parameters; therefore, the centrality measure $\chi = N_{\mathrm{W}}/(2A)$ is introduced. At $\sqrt{s_{\mathrm{NN}}} = 200$ GeV the baryon number is not deposited into the fluid.

TRENTo

The third model, TRENTo [122], introduces a generalized ansatz for the entropy deposition from the participant nucleons using the reduced thickness

function defined as

$$T_R(p; T_A, T_B) = \left(\frac{T_A^p + T_B^p}{2} \right)^{1/p}, \tag{5.12}$$

where $T_{A,B}$ are the thickness profiles of participant nucleons defined as

$$T_{A,B}(x, y) = \int \mathrm{d}z \rho_{A,B}(x, y, z), \tag{5.13}$$

and p is a dimensionless parameter that interpolates between the minimum and maximum of T_A and T_B:

$$T_R = \begin{cases} \max(T_A, T_B) & p \to +\infty, \\ (T_A + T_B)/2 & p = +1 \text{ (arithmetic mean)}, \\ \sqrt{T_A T_B} & p = 0 \text{ (geometric mean)}, \\ 2T_A T_B/(T_A + T_B) & p = -1 \text{ (harmonic mean)}, \\ \min(T_A, T_B) & p \to -\infty. \end{cases} \tag{5.14}$$

The value $p = 1$ corresponds to a Monte Carlo wounded nucleon model, and the value $p = 0$ corresponds to the IP-Glasma model [123]. However, the parameter p is continuous and can have any real value. In this work we present results obtained with $p = 0$, since those results provide best description of p_T spectra and elliptic flow.

To obtain three-dimensional initial state, we extended the TRENTo analogously to GLISSANDO. The only difference is absence of the tilt in the energy density deposition from forward- and backward-going participants, as the contributions from them are merged in the output table from TRENTo. The three-dimensional entropy density is obtained by multiplying the two-dimensional entropy density generated using TRENTo and the longitudinal profile $H(\eta_s)$ defined in Eq. (5.8). The profile is then normalized according to Eq. (5.6). For the baryon number deposition, a simple symmetric double Gaussian profile has been chosen:

$$\exp\left(-\frac{(|\eta_s| - \eta_B)^2}{2\sigma_B^2} \right). \tag{5.15}$$

The deposited baryon number is also normalized according to Eq. (5.10). The longitudinal structure parameters used for the simulations were the same as in the case of GLISSANDO IS (see Table 5.1).

Centrality

For all three IS models, the centrality classes are defined in the same way, as fixed ranges of the number of wounded nucleons N_W (Table 5.2). The ranges were obtained by running a large set of minimum-biased events using GLISSANDO. The resulting ranges are consistent with the classes defined by the STAR collaboration [73].

$\sqrt{s_{\mathrm{NN}}}$ [GeV]	centrality [%]	0	5	10	20	30	40	50
27	N_{W}	394	321	272	196	138	93	60
62.4	N_{W}	394	327	274	197	139	95	62
200	N_{W}	394	330	283	201	142	99	63

Table 5.2: The upper limits on the number of wounded nucleons for given centrality percentiles for energies $\sqrt{s_{\mathrm{NN}}} = 27$, 62.4, and 200 GeV obtained from GLISSANDO.

5.1.2 Hydrodynamics

For the hot and dense phase of the collision, our model uses a 3-dimensional relativistic viscous hydrodynamic code vHLLE [110]. The code solves the conservation of the energy-momentum tensor $T^{\mu\nu}$ and the conserved charges N_c:

$$\partial_\nu T^{\mu\nu} = 0, \tag{5.16a}$$

$$\partial_\nu N_c^\nu = 0. \tag{5.16b}$$

The code is written in Milne coordinates (Sect. 3.1) which have the metric tensor

$$g^{\mu\nu} = \mathrm{diag}(1, -1, -1, -1/\tau^2). \tag{5.17}$$

In Milne coordinates, ordinary derivatives must be replaced by covariant derivatives

$$\nabla_\nu T^{\mu\nu} = 0, \tag{5.18a}$$

$$\nabla_\nu N_c^\nu = 0. \tag{5.18b}$$

Then, the hydrodynamic equations take the form:

$$\partial_\nu T^{\tau\nu} + \tau T^{\eta\eta} + \frac{1}{\tau} T^{\tau\tau} = 0, \tag{5.19a}$$

$$\partial_\nu T^{x\nu} + \frac{1}{\tau} T^{x\tau} = 0, \tag{5.19b}$$

$$\partial_\nu T^{y\nu} + \frac{1}{\tau} T^{y\tau} = 0, \tag{5.19c}$$

$$\partial_\nu T^{\eta\nu} + \frac{3}{\tau} T^{\eta\tau} = 0, \tag{5.19d}$$

$$\partial_\nu N_c^\nu + \frac{1}{\tau} N_c^\tau = 0. \tag{5.19e}$$

The vHLLE uses a clever trick here to avoid scaling the terms with $1/\tau$. By combining terms and multiplying equations by τ (and η component by τ^2), the equa-

tions take the form:

$$\partial_\nu(\tau T^{\tau\nu}) + \tau^2 T^{\eta\eta} = 0, \tag{5.20a}$$
$$\partial_\nu(\tau T^{x\nu}) = 0, \tag{5.20b}$$
$$\partial_\nu(\tau T^{y\nu}) = 0, \tag{5.20c}$$
$$\partial_\nu(\tau T^{\tau\nu}) + \tau^2 T^{\eta\eta} = 0, \tag{5.20d}$$
$$\partial_\nu(\tau N_c^\nu) = 0. \tag{5.20e}$$

Moreover, by redefining the energy-momentum tensor as follows:

$$T^{\mu\nu} = \tilde{T}^{\mu\nu}, \quad \mu,\nu \neq \eta, \tag{5.21a}$$
$$T^{\mu\eta} = \tilde{T}^{\mu\eta}/\tau, \quad \mu \neq \eta, \tag{5.21b}$$
$$T^{\eta\eta} = \tilde{T}^{\eta\eta}/\tau^2, \tag{5.21c}$$
$$N_c^\eta = \tilde{N}_c^\eta/\tau, \tag{5.21d}$$

and with:

$$\tilde{\partial}_\mu \equiv \left\{ \frac{\partial}{\partial\tau}, \frac{\partial}{\partial x}, \frac{\partial}{\partial y}, \frac{1}{\tau}\frac{\partial}{\partial\eta} \right\}, \tag{5.22}$$

the Eqs. (5.20) can be rewritten as:

$$\tilde{\partial}_\nu(\tau\tilde{T}^{\tau\nu}) + \frac{1}{\tau}(\tau\tilde{T}^{\eta\eta}) = 0, \tag{5.23a}$$
$$\tilde{\partial}_\nu(\tau\tilde{T}^{x\nu}) = 0, \tag{5.23b}$$
$$\tilde{\partial}_\nu(\tau\tilde{T}^{y\nu}) = 0, \tag{5.23c}$$
$$\tilde{\partial}_\nu(\tau\tilde{T}^{\tau\nu}) + \frac{1}{\tau}(\tau\tilde{T}^{\eta\eta}) = 0, \tag{5.23d}$$
$$\tilde{\partial}_\nu(\tau\tilde{N}_c^\nu) = 0. \tag{5.23e}$$

These are the equations that the code solves.

The viscous corrections are added within the Müller-Israel-Stewart theory described in Sect. 4.2.2. Similarly to the energy-momentum tensor, the factor $1/\tau$ is removed from the shear stress tensor as

$$\pi^{\mu\eta} = \tilde{\pi}^{\mu\eta}/\tau, \tag{5.24a}$$
$$\pi^{\eta\eta} = \tilde{\pi}^{\eta\eta}/\tau^2, \tag{5.24b}$$
$$u^\eta = \tilde{u}^\eta/\tau. \tag{5.24c}$$

Using these definitions, the differential equations describing the evolution of viscous coefficients can be rewritten as follows

$$\begin{aligned}\tilde{\gamma}\left(\partial_\tau + \tilde{v}^i\tilde{\partial}_i\right)\tilde{\pi}^{\mu\nu} = &-\frac{\tilde{\pi}^{\mu\nu} - \tilde{\pi}^{\mu\nu}_{\mathsf{NS}}}{\tau_\pi} - \frac{4}{3}\tilde{\pi}^{\mu\nu}\tilde{\partial}_{;\gamma}\tilde{u}^\gamma - \\ &- \left[\tilde{u}^\nu\tilde{\pi}^{\mu\beta} + \tilde{u}^\mu\tilde{\pi}^{\nu\beta}\right]\tilde{u}^\lambda\tilde{\partial}_{;\lambda}\tilde{u}_\beta - I^{\mu\nu}_{\pi,G},\end{aligned} \tag{5.25a}$$

$$\tilde{\gamma}\left(\partial_\tau + \tilde{v}^i\tilde{\partial}_i\right)\Pi = -\frac{\Pi - \Pi_{\mathsf{NS}}}{\tau_\Pi} - \frac{4}{3}\Pi\tilde{\partial}_{;\gamma}\tilde{u}^\gamma, \tag{5.25b}$$

where $\tilde{\gamma} = u^0$, $\tilde{v}^i = \tilde{u}^i/u^0$, the subscript NS is for the Navier-Stokes limit case values given by Eqs. (4.10, 4.11) and $\tilde{\partial}_{;\mu}$ denotes the covariant derivative. The last term $I^{\mu\nu}_{\pi,G}$ denotes geometrical source terms given by

$$\begin{aligned} I^{\tau\tau}_{\pi,G} &= 2\tilde{u}^\eta\tilde{\pi}^{\tau\eta}/\tau, & I^{\eta x}_{\pi,G} &= \tilde{u}^\eta\tilde{\pi}^{\tau x}/\tau, \\ I^{\tau x}_{\pi,G} &= \tilde{u}^\eta\tilde{\pi}^{\eta x}/\tau, & I^{\eta y}_{\pi,G} &= \tilde{u}^\eta\tilde{\pi}^{\tau y}/\tau, \\ I^{\tau y}_{\pi,G} &= \tilde{u}^\eta\tilde{\pi}^{\eta y}/\tau, & I^{\eta\eta}_{\pi,G} &= 2\tilde{u}^\eta\tilde{\pi}^{\tau\eta}/\tau, \\ I^{\tau\eta}_{\pi,G} &= \tilde{u}^\eta\left(\tilde{\pi}^{\tau\tau} + \tilde{\pi}^{\eta\eta}\right)/\tau, & I^{xx}_{\pi,G} &= I^{xy}_{\pi,G} = I^{yy}_{\pi,G} = 0. \end{aligned}$$

In practice, the hydrodynamic code evolves the Q vector instead of the energy-momentum tensor

$$Q^\mu = T^{0\mu}. \tag{5.26}$$

The algorithm calculating the evolution of the QGP has three steps which occur at each timestep:

1. The ideal part of the energy-momentum tensor is evolved using the Godunov-type method,
2. Israel-Stewart equations (5.25) are solved to propagate the bulk viscosity and the shear stress tensor for the next timestep,
3. ideal part of the energy-momentum tensor is updated according to the viscous fluxes between cells.

For this study we used temperature-independent values of the shear viscosity to entropy density ratio $\eta/s = 0.12$ for $\sqrt{s_{\mathrm{NN}}} = 27\,\mathrm{GeV}$ and $\eta/s = 0.08$ for the two higher energies. The bulk viscosity was set to zero. For the relaxation time of the shear stress tensor, we used ansatz

$$\tau_\pi = 5\eta/(sT). \tag{5.27}$$

For EoS we used the chiral model [124]. This EoS includes correct degrees of freedom and thus works for both high (quarks) and low (hadrons) temperature limits. It has a crossover phase transition between hadronic and partonic phases for all values of the baryon chemical potential μ_B. Its results are in agreement with the lattice QCD data at $\mu_B = 0$.

5.1.3 Particlization and Final-State Interactions

The particlization occurs at a freeze-out hypersurface with fixed energy density $\varepsilon_{\mathrm{crit}} = 0.5\,\mathrm{GeV/fm^3}$. This hypersurface is reconstructed using the `Cornelius` subroutine [125]. The subroutine iterates over all possible 4-dimensional hypercubes of neighbouring cells[1] and from the energy density values at the vertices

[1] neighbouring both in time and space

it finds out whether the freeze-out hypersurface intersects the hypercube and, if so, where is the intersection.

From the freeze-out hypersurface, a Cooper-Frye prescription [107] is used to sample hadrons. Their formula says that the number of particles N, which are emitted on the freeze-out hypersurface Σ, is given by

$$N = \int \frac{\mathrm{d}^3 p}{E_p} \int \mathrm{d}\Sigma_\mu(x) p^\mu f(p, T(x), \mu_i(x)), \tag{5.28}$$

where $f(p, T(x), \mu_i(x))$ is the particle distribution function. Instead of calculating the integrals, our hybrid model samples the hadrons using Monte Carlo procedure to better reproduce the experimental setup. Moreover, the sampling procedure also contains an ansatz for viscous corrections. The overall formula that samples hadrons for each element of the freeze-out hypersurface $\Delta\Sigma_\mu$ separately is the following

$$\frac{\mathrm{d}^3 \Delta N_i}{\mathrm{d}p^* \mathrm{d}(\cos\theta)\mathrm{d}\phi} = \frac{\Delta\Sigma^*_\mu p^{*\mu}}{p^{*0}} p^{*2} f_{\mathsf{eq}}(p^{*0}; T, \mu_i) \left[1 + (1 \mp f_{\mathsf{eq}}) \frac{p^*_\mu p^*_\nu \pi^{*\mu\nu}}{2T^2(\varepsilon + P)}\right]. \tag{5.29}$$

Here, P is the pressure, and the $*$ superscript refers to quantities in the local fluid rest frame. The sampling procedure has the following steps:

1. Calculate the average number of each hadron species N_i,
2. randomly generate the total number of particles to be created N_{tot} according to a Poisson distribution with mean value $\sum_i N_i$,
3. for each generated particle, the type is randomly chosen with probability N_i/N_{tot},
4. randomly generate momentum in the rest frame of the local fluid according to the isotropic part of Eq. (5.29),
5. apply the viscous correction from Eq. (5.29) using rejection sampling,
6. boost the particle momentum to the center of mass frame of the system,
7. the transverse and time coordinates are set to the centroid of the corresponding hypersurface element, and the space-time rapidity is uniformly generated within the longitudinal size of the element volume.

After the particlization, the sampled hadrons are passed to the `UrQMD` cascade, which simulates hadronic rescatterings and resonance decays.

To increase the statistics, we generated a few hundred events from each hydrodynamic simulation. This procedure is called oversampling. These events

are then passed separately into the UrQMD cascade. For this study, we generated 3.000 hydrodynamic simulations. From each corresponding hypersurface, we generated 500 events for each IS setup, resulting in a total of 1.500.000 events to be analyzed.

5.2 Rapidity Distributions

As was mentioned in Sect. 3.2, the rapidity distributions are the most basic observables. Therefore, we used this observable to fine-tune the parameters of the longitudinal structure of the initial models. In an experiment, it is difficult to cover the whole rapidity interval. As a consequence, there is limited experimental data on rapidity distributions.

Figures 5.2 and 5.3 show the pseudorapidity distribution of charged hadrons calculated with GLISSANDO and UrQMD IS, respectively. The T_RENTo IS has a longitudinal structure similar to GLISSANDO and thus its pseudorapidity distribution is very similar. Our results are compared to the experimental data measured by the PHOBOS experiment. Due to missing data at $\sqrt{s_{\mathrm{NN}}} = 27$ GeV we show experimental data at $\sqrt{s_{\mathrm{NN}}} = 19.6$ and 62.4 GeV and our calculated results at $\sqrt{s_{\mathrm{NN}}} = 27$ GeV are expected to be between these energies (and closer to 19.6 GeV). One can see that at pseudorapidity $\eta \sim \pm 2$, the UrQMD IS produces a little larger $\mathrm{d}N/\mathrm{d}\eta$, which is balanced by smaller tails compared to GLISSANDO IS.

At BES energies, the baryon number plays an important role. To study the impact of baryon number in the initial state, we may use net protons - protons minus antiprotons. Figures 5.4 and 5.5 show the rapidity distribution of net protons in Au+Au collisions at $\sqrt{s_{\mathrm{NN}}} = 27$ and 62.4 GeV compared to the experimental data. Again, available experimental data are very limited, so we compared the results at energy 27 GeV with the NA49 measurements at 17.2 GeV. At $\sqrt{s_{\mathrm{NN}}} = 62.4$ GeV the experimental data were taken from the BRAHMS experiment. At both energies, the simulated centrality was unavailable, and thus we compared it to the closest centrality bin. The longitudinal profiles of the baryon density in GLISSANDO and T_RENTo IS were tuned by the parameters η_B and σ_B using these data. In UrQMD IS the initial baryon density profile is fixed and results in a narrower final-state net proton rapidity distribution.

5.3 Transverse Momentum Spectra

The transverse momentum spectra of identified hadrons at mid-rapidity are shown in Figs. 5.6 for energy 27 GeV and 5.7 for energy 62.4 GeV, compared to

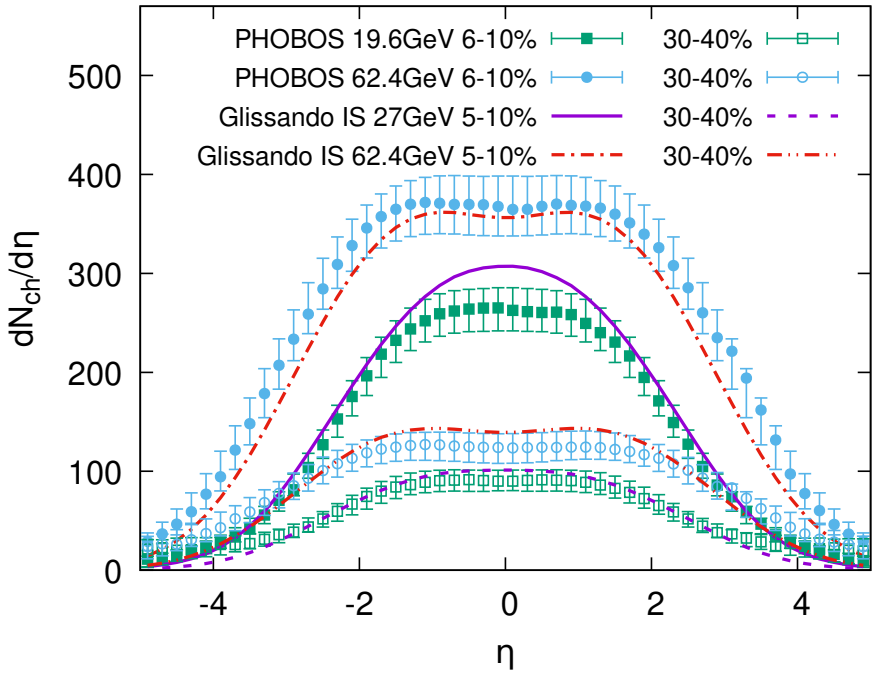

Figure 5.2: Pseudorapidity distributions of charged hadrons in Au+Au collisions at $\sqrt{s_{\mathrm{NN}}} = 27$ and 62.4 GeV obtained from hybrid model `GLISSANDO+vHLLE+UrQMD`. Since there are no experimental data for pseudorapidity distributions at $\sqrt{s_{\mathrm{NN}}} = 27$ GeV, we compared our results to experimental data at $\sqrt{s_{\mathrm{NN}}} = 19.6$ GeV. The experimental data points are from PHOBOS collaboration [57].

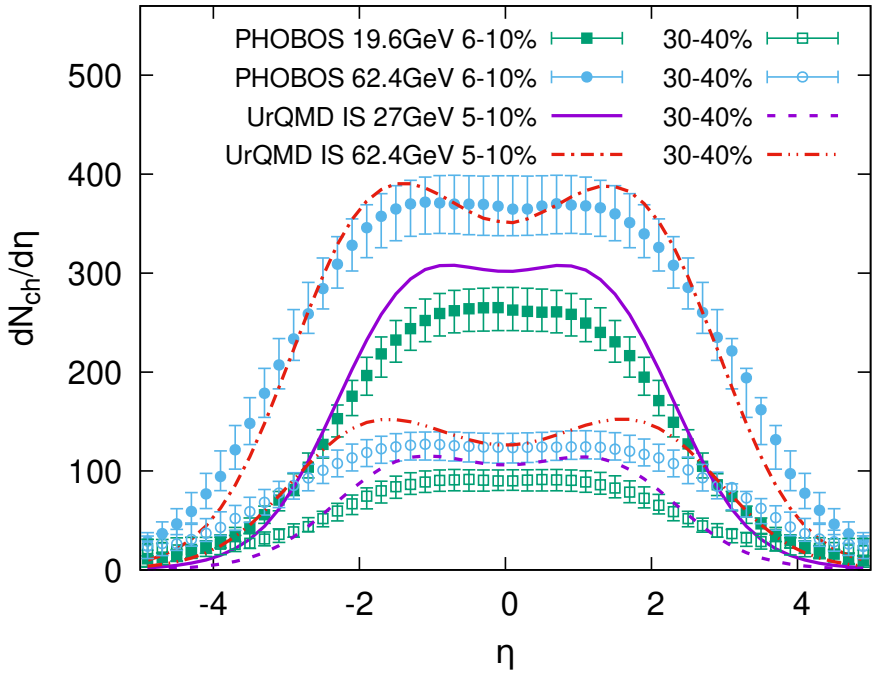

Figure 5.3: Same as Fig. 5.2, but with `UrQMD` IS.

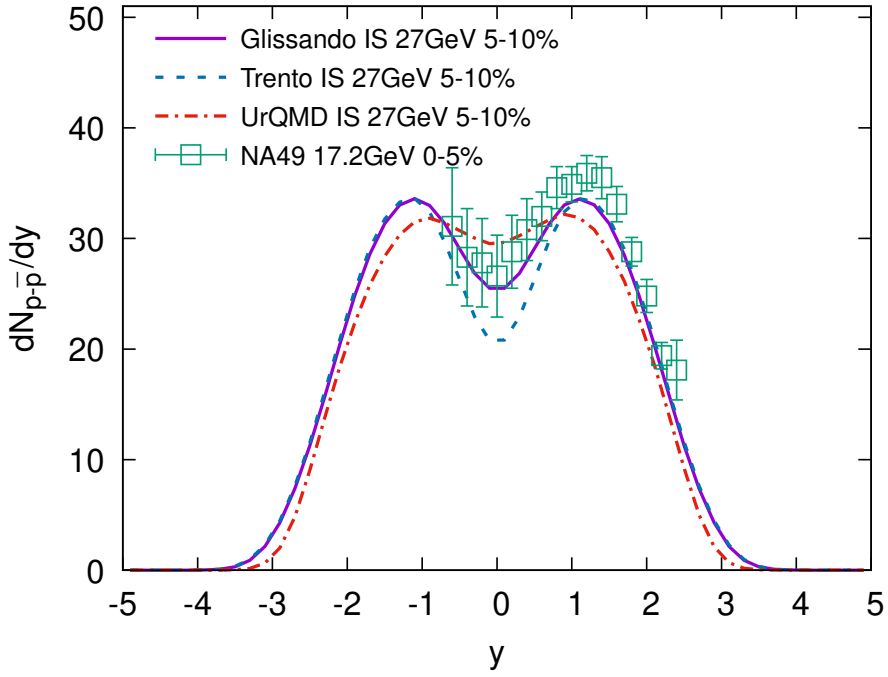

Figure 5.4: Rapidity distribution of net protons in Au+Au collisions at $\sqrt{s_{\mathrm{NN}}} = 27\,\mathrm{GeV}$ obtained from hybrid model vHLLE+UrQMD with GLISSANDO, TRENTo and UrQMD IS. Since there are no experimental data at $\sqrt{s_{\mathrm{NN}}} = 27\,\mathrm{GeV}$, we compared our results to experimental data at $\sqrt{s_{\mathrm{NN}}} = 17.2\,\mathrm{GeV}$. The experimental data points are from NA49 collaboration [126].

experimental data from STAR. In these plots, the spectra of kaons and protons are scaled by the factor of 2 and 10, respectively, to be able to show all three spectra in one plot. The most noticeable difference between the three initial states is in the magnitude of the proton spectrum and slightly different slopes of pion (visible mostly at large p_T) and proton spectra. The former is a consequence of a larger baryon density at mid-rapidity with UrQMD IS as compared to GLISSANDO IS, whereas the latter is a result of a slightly smaller radial flow developed with UrQMD IS as compared to TRENTo IS. From these differences, we may conclude that UrQMD IS overestimates the proton spectra. On the other hand, TRENTo IS provides the best-combined description of all three spectra at both energies.

To examine the p_T spectra across all centralities, we analyzed the centrality dependence of the mean transverse momentum. Figures 5.8 and 5.9 show the mean p_T of positively charged pions, kaons, and protons as functions of centrality in Au+Au collisions at $\sqrt{s_{\mathrm{NN}}} = 27$ and $62.4\,\mathrm{GeV}$, respectively. At $\sqrt{s_{\mathrm{NN}}} = 27\,\mathrm{GeV}$, the simulated data agree with the experimental data from STAR within errorbars for kaons and pions for all three IS, however, our model overestimates the

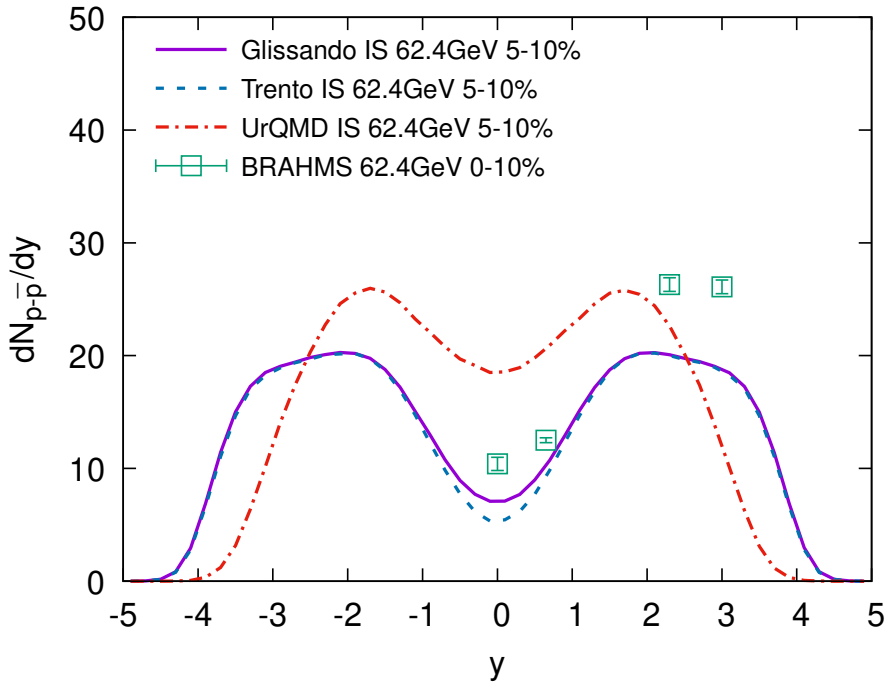

Figure 5.5: Same as Fig. 5.4, but for $\sqrt{s_{\mathrm{NN}}} = 62.4$ GeV Au+Au collisions. The experimental data points are from BRAHMS collaboration [127].

mean p_T of the protons, which is again a result of slightly stronger radial flow in the fluid stage with TRENTo IS. Unlike the p_T spectra, in this case, the results with TRENTo IS are the furthest from the experimental data. At $\sqrt{s_{\mathrm{NN}}} = 62.4$ GeV we observe the same hierarchy between the three IS, but our model now underestimates the mean p_T of protons. Also, at this energy, even the kaon mean p_T is overestimated in the most central bin. As for the mean p_T, the best combined results are provided by GLISSANDO IS.

5.4 Elliptic and Triangular Flow

Next, we focused on elliptic and triangular flow. We computed elliptic and triangular flows as functions of transverse momentum using the 2-particle cumulant method (Sect. 3.4.2) in 20-30% central Au+Au collisions at $\sqrt{s_{\mathrm{NN}}} = 27$ (Fig. 5.10) and 62.4 GeV (Fig. 5.11). Unfortunately, the triangular flow measurements have been published only for energy $\sqrt{s_{\mathrm{NN}}} = 200$ GeV [128] and not yet for BES energies. Furthermore, the elliptic flow data at $\sqrt{s_{\mathrm{NN}}} = 62.4$ GeV are not available. From the comparison with STAR data at $\sqrt{s_{\mathrm{NN}}} = 27$ GeV, one may notice that at $p_T < 1$ GeV the calculations with TRENTo and UrQMD IS can reproduce the data, while GLISSANDO IS underestimates the elliptic flow. With increasing p_T all three IS models start to underestimate the elliptic flow. In both elliptic and

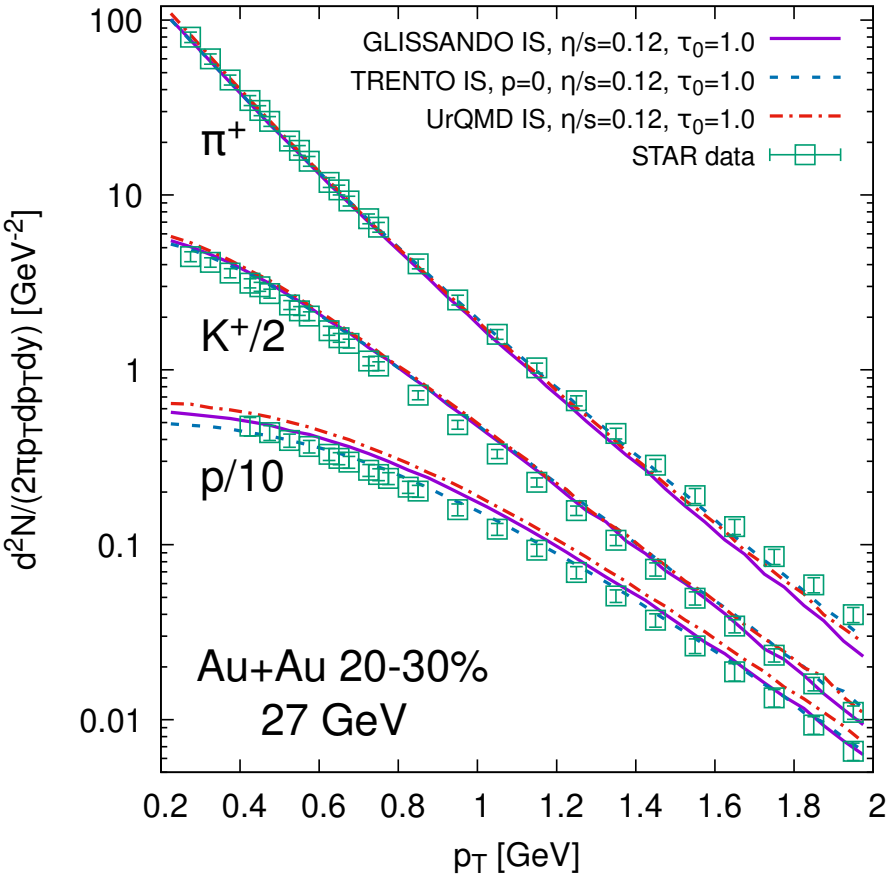

Figure 5.6: Transverse momentum spectra of positively charged pions, kaons and protons in 20-30% central Au+Au collisions at $\sqrt{s_{\mathrm{NN}}} = 27$ GeV obtained from hybrid model vHLLE+UrQMD with GLISSANDO, TRENTo and UrQMD IS. The experimental data points are from STAR collaboration [58].

triangular flow at both energies we may see the same hierarchy: the TRENTo IS produces the largest flow, while GLISSANDO IS produces the smallest flow. The only exception is elliptic flow at $\sqrt{s_{\mathrm{NN}}} = 27$ GeV at high p_T.

Figures 5.12 and 5.13 show p_T-integrated elliptic and triangular flow as functions of centrality computed using the cumulant method for Au+Au collisions at $\sqrt{s_{\mathrm{NN}}} = 27$ and 62.4 GeV, respectively. The first thing to notice is that again the IS models follow the same hierarchy of the flow at all centralities. At $\sqrt{s_{\mathrm{NN}}} = 62.4$ GeV the TRENTo IS reproduces the STAR data perfectly, while the other two IS models underestimate the data. At lower energy, TRENTo IS even overestimates the elliptic flow for centralities 5-10% and 10-20%, but again reproduces the experimental data for more peripheral collisions. Figure 5.14 shows the same observable, but calculated using the EP method (Sect. 3.4.1). This figure quantitatively shows the same result as the calculation with the cumulant method.

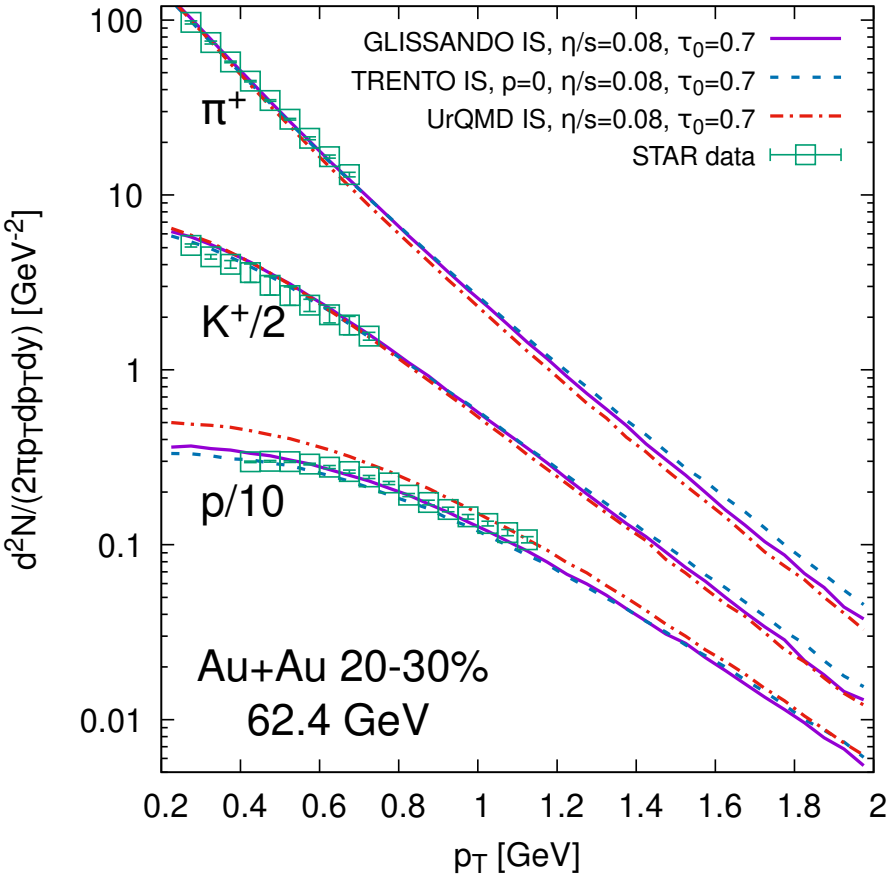

Figure 5.7: Same as Fig. 5.6, but for $\sqrt{s_{\mathrm{NN}}} = 62.4$ GeV Au+Au collisions. The experimental data points are from STAR collaboration [59].

Surprisingly, the calculation of the hybrid model with TRENTo IS provides the best description of the experimental data of the elliptic flow even though it was developed to work at much higher energies.

As was already mentioned in Sect. 3.4, the final-state anisotropic flow is strongly correlated with initial-state eccentricity anisotropies. This causes the difference between results from various IS models. To illustrate this, we plot the mean eccentricity ε_2 and ε_3 defined via

$$\varepsilon_n e^{in\Psi_n} = \frac{\int e^{in\phi} r^n \rho(\vec{r}) \mathrm{d}\phi r \mathrm{d}r}{\int r^n \rho(\vec{r}) \mathrm{d}\phi r \mathrm{d}r} \tag{5.30}$$

as a function of centrality (Fig. 5.15). This figure shows the reason why TRENTo IS produces the largest elliptic flow. However, UrQMD and GLISSANDO show a reverse hierarchy (although quite close), which means that their difference in elliptic flow is rooted in the hydrodynamic evolution.

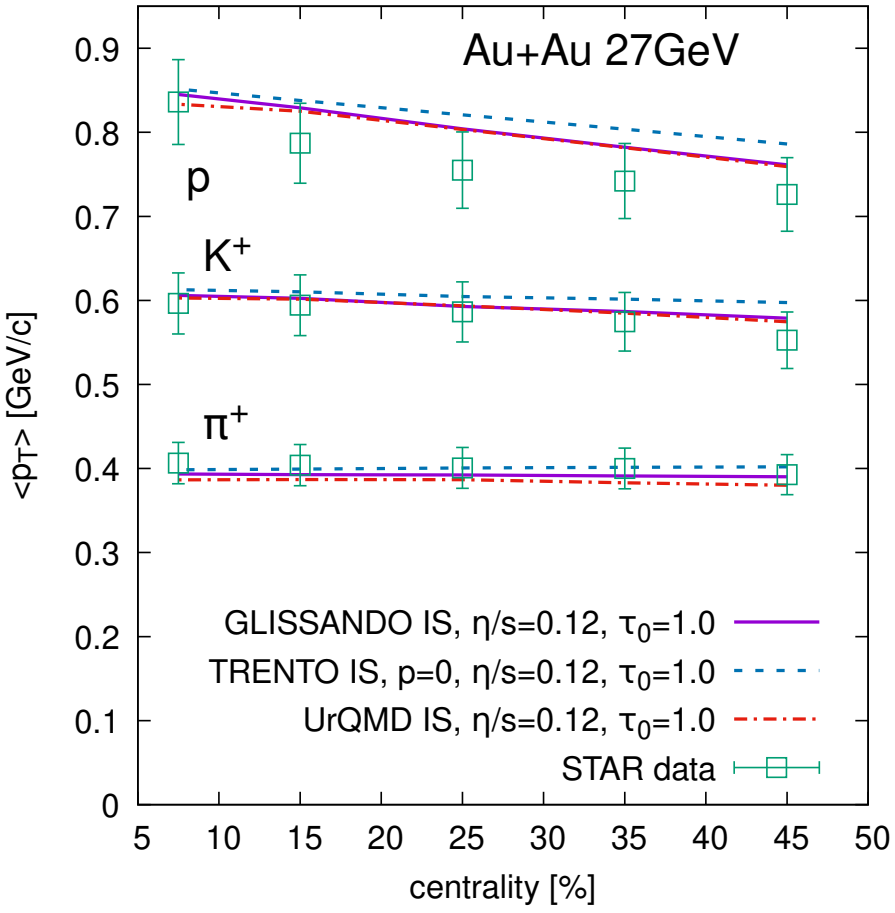

Figure 5.8: Mean transverse momentum of positively charged pions, kaons and protons as a function of centrality in Au+Au collisions at $\sqrt{s_{\mathrm{NN}}} = 27$ GeV obtained from hybrid model `vHLLE+UrQMD` with `GLISSANDO`, `TRENTo` and `UrQMD` IS. The experimental data points are from STAR collaboration [58].

5.5 Longitudinal Structure of Elliptic Flow

While most studies of the collective flow focus on the midrapidity region, the longitudinal structure of the flow starts to be researched as well. Early studies focused on fluctuations along the longitudinal direction [130, 131]. Later, a linear twist of the EP angle Ψ_n along the longitudinal direction has been suggested in Color Glass Condensate (CGC) model [132, 133] and in the Monte-Carlo wounded nucleon model [134]. So far, phenomenology groups studied longitudinal decorrelation only for top RHIC and LHC energies, using the (3+1)D viscous hydrodynamic model with `AMPT` IS model [6, 76, 135, 136] or Monte Carlo Glauber IS [137–139] and also using the pure `AMPT` model [78, 140, 141].

First, we computed pseudorapidity-dependent elliptic flow using the EP method, which is shown in Fig. 5.16 for $\sqrt{s_{\mathrm{NN}}} = 27$ GeV and in Fig. 5.17 for $\sqrt{s_{\mathrm{NN}}} = 200$ GeV. At $\sqrt{s_{\mathrm{NN}}} = 27$ GeV all models reproduce the overall magnitude of the

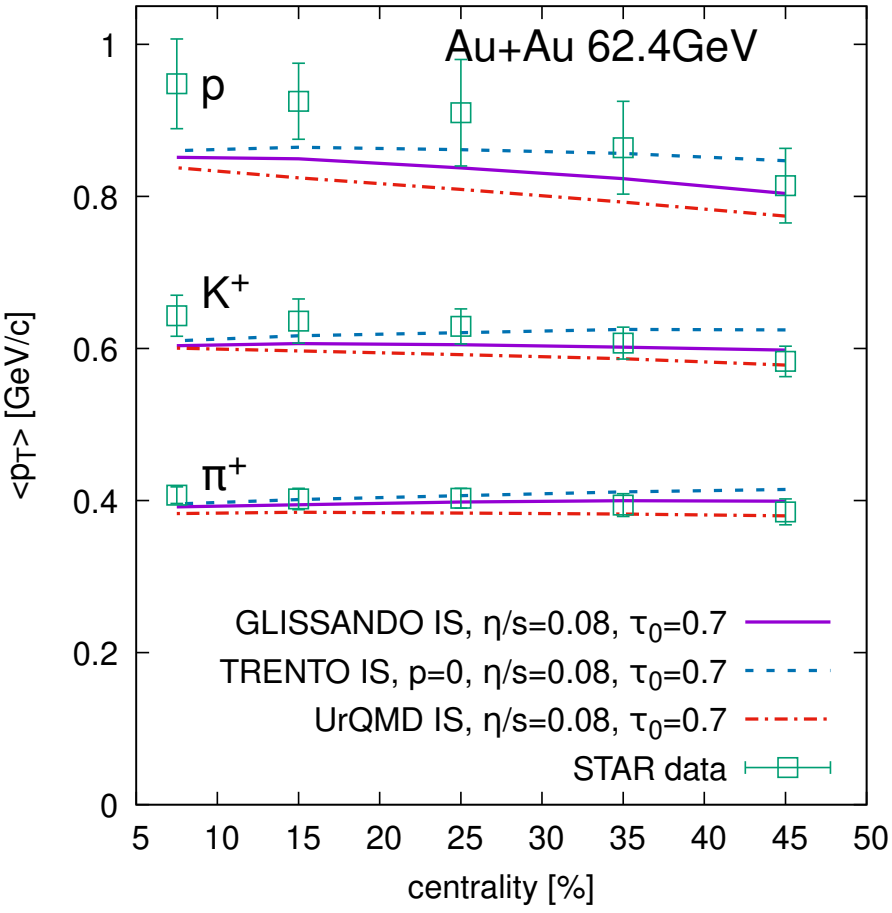

Figure 5.9: Same as Fig. 5.8, but for $\sqrt{s_{\mathrm{NN}}} = 62.4$ GeV Au+Au collisions. The experimental data points are from STAR collaboration [59].

flow, but UrQMD and TRENTo IS underestimate its value at midrapidity, which is consistent with the previous section. At $\sqrt{s_{\mathrm{NN}}} = 200$ GeV the experimental data show a triangular dependence that neither of the IS models can describe. A similar shape can also be seen in older PHOBOS data [142].

Figures 5.18 and 5.19 show the factorization ratio r_2 defined in Eq. (3.38) characterizing longitudinal decorrelation of the elliptic flow compared to STAR preliminary data. For these calculations, we excluded TRENTo IS, because its longitudinal structure does not include the tilt defined by Eq. (5.7) and therefore no decorrelation can be seen in those results. For the comparison with the preliminary data, we used the same pseudorapidity reference bin ($2.1 < \eta_{\mathrm{ref}} < 5.1$ for $\sqrt{s_{\mathrm{NN}}} = 27$ GeV, $2.5 < \eta_{\mathrm{ref}} < 4$ for $\sqrt{s_{\mathrm{NN}}} = 200$ GeV) and p_T cut for charged hadrons ($0.4 < p_T < 4$ GeV). At $\sqrt{s_{\mathrm{NN}}} = 27$ GeV the UrQMD IS model predicts a much stronger decorrelation than the one seen in the preliminary data. The GLISSANDO IS overestimates the decorrelation just slightly at this energy. At $\sqrt{s_{\mathrm{NN}}} = 200$ GeV UrQMD IS still provides a stronger decorrelation, while GLISSANDO

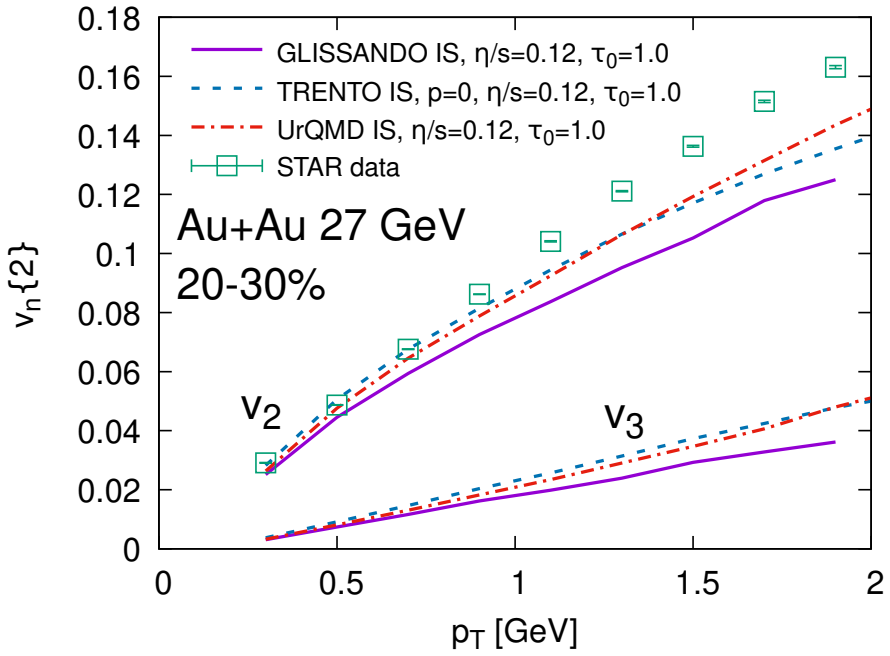

Figure 5.10: Elliptic and triangular flows as functions of transverse momentum p_T in 20-30% central Au+Au collisions at $\sqrt{s_{\rm NN}} = 27$ GeV obtained from hybrid model `vHLLE+UrQMD` with `GLISSANDO`, `TRENTo` and `UrQMD` IS. The experimental data points are from STAR collaboration [73].

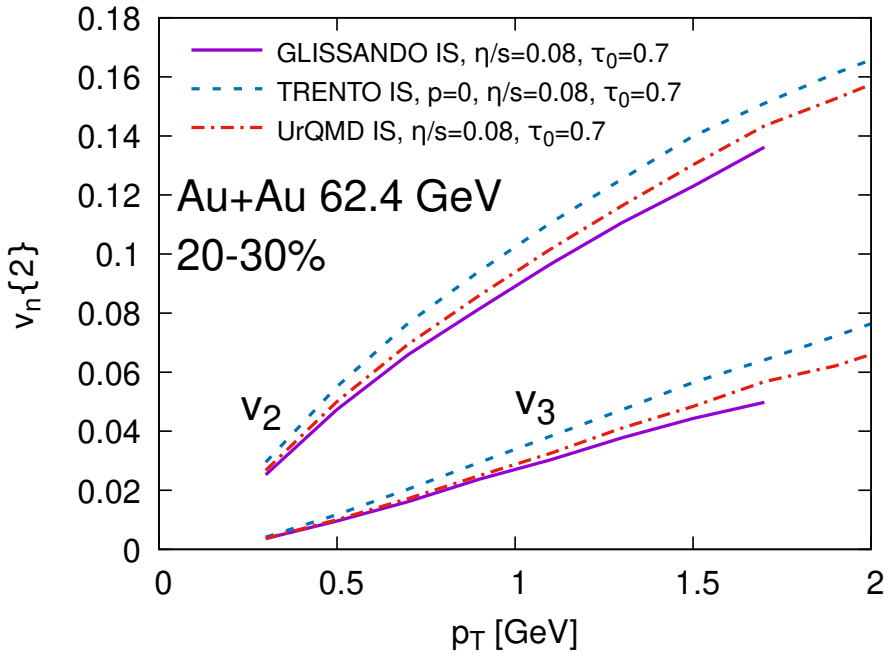

Figure 5.11: Same as Fig. 5.10, but for $\sqrt{s_{\rm NN}} = 62.4$ GeV Au+Au collisions.

IS in this case predicts a weaker decorrelation. At both energies, `GLISSANDO` IS can describe the data within the uncertainties limits.

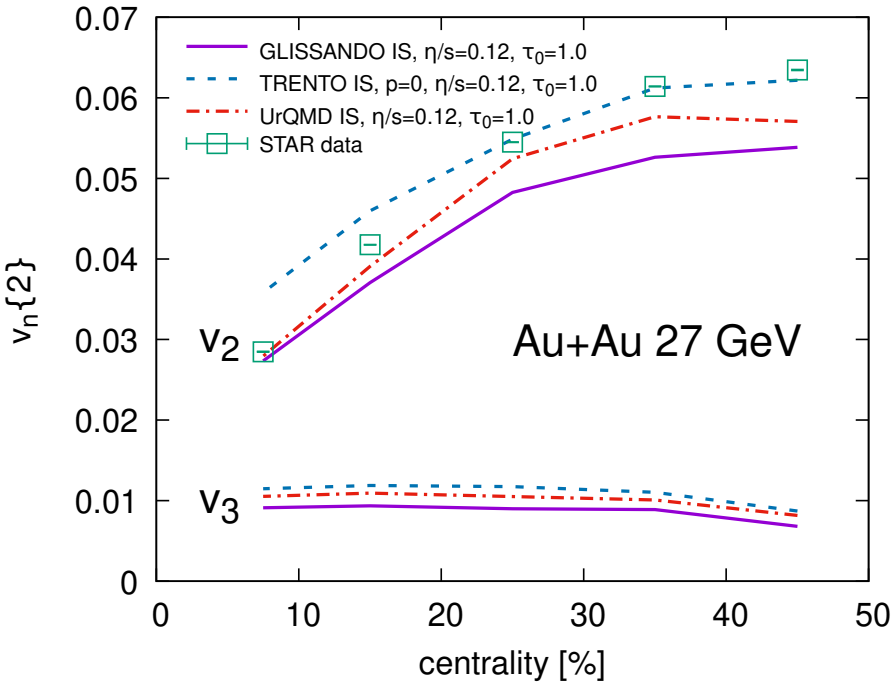

Figure 5.12: Elliptic and triangular flows as functions of centrality in Au+Au collisions at $\sqrt{s_{\mathrm{NN}}} = 27$ GeV obtained from hybrid model vHLLE+UrQMD with GLISSANDO, TRENTo and UrQMD IS. The experimental data points are from STAR collaboration [73].

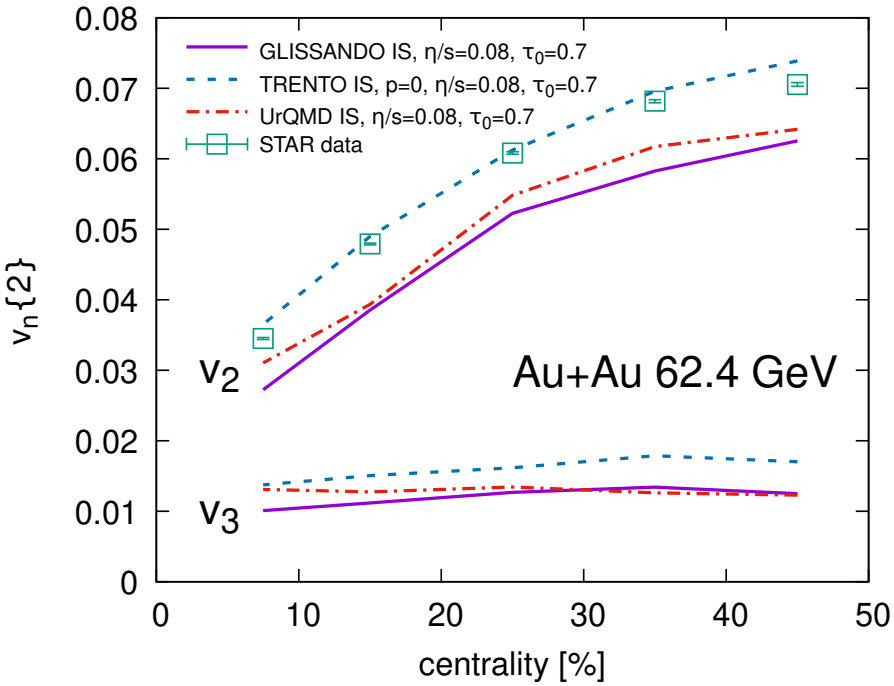

Figure 5.13: Same as Fig. 5.12, but for $\sqrt{s_{\mathrm{NN}}} = 62.4$ GeV Au+Au collisions. The experimental data points are from STAR collaboration [129].

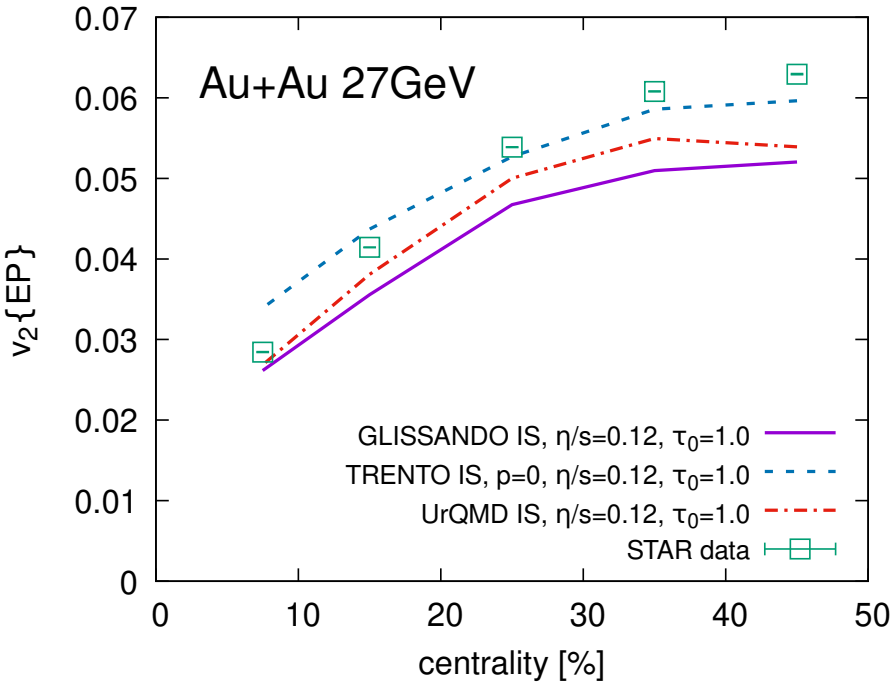

Figure 5.14: Same as Fig. 5.12, but calculated using EP method. The experimental data points are from STAR collaboration [73].

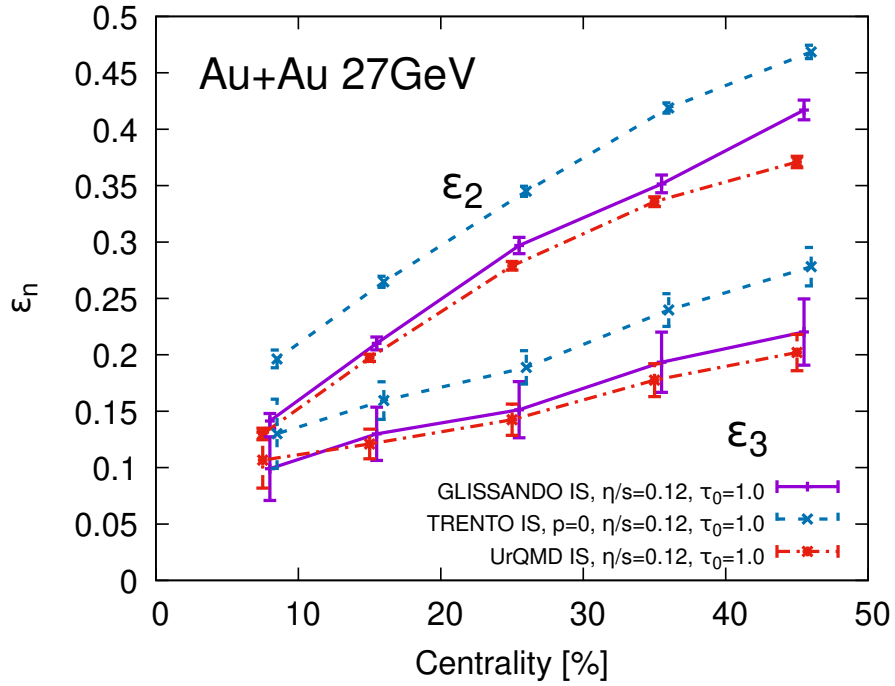

Figure 5.15: Average eccentricities of the initial state energy density as functions of the centrality in Au+Au collisions at $\sqrt{s_{\mathrm{NN}}} = 27\,\mathrm{GeV}$ obtained from GLISSANDO, TRENTo and UrQMD IS models.

To understand the origin of the decorrelation, we computed the contributions to the factorization ratio from the flow angle and the flow magnitude us-

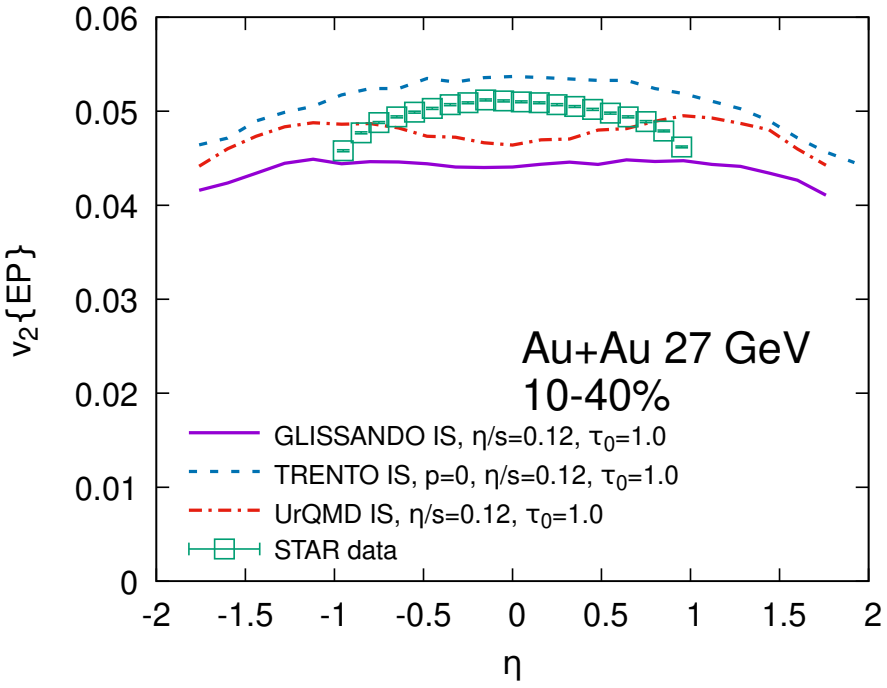

Figure 5.16: Elliptic flow as a function of pseudorapidity in 10-40% central Au+Au collisions at $\sqrt{s_{\rm NN}} = 27$ GeV obtained from hybrid model vHLLE+UrQMD with GLISSANDO, TRENTo and UrQMD IS. The experimental data points are from STAR collaboration [73].

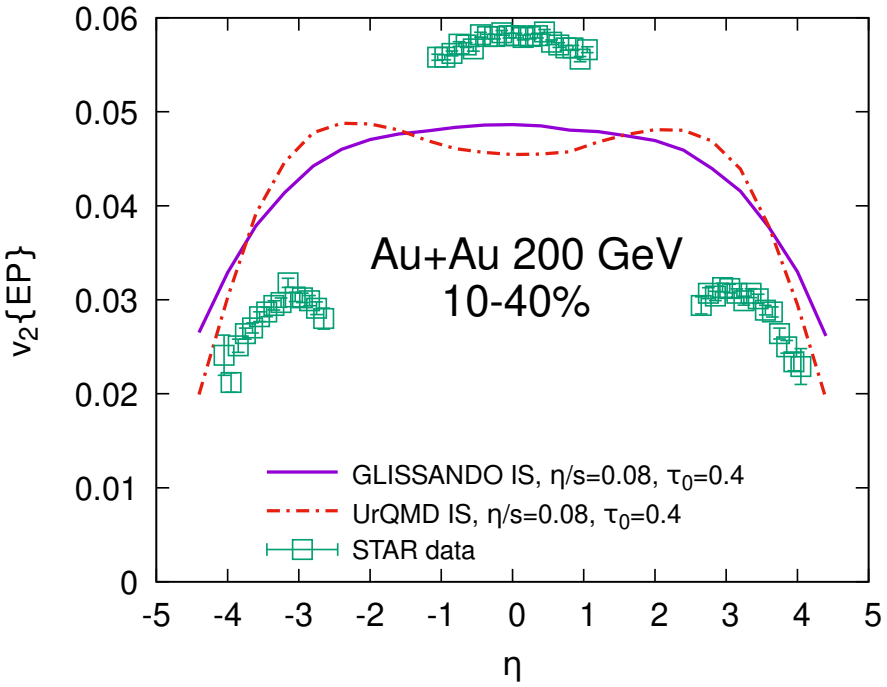

Figure 5.17: Same as Fig. 5.16, but for $\sqrt{s_{\rm NN}} = 200$ GeV Au+Au collisions. The experimental data points are from STAR collaboration [143].

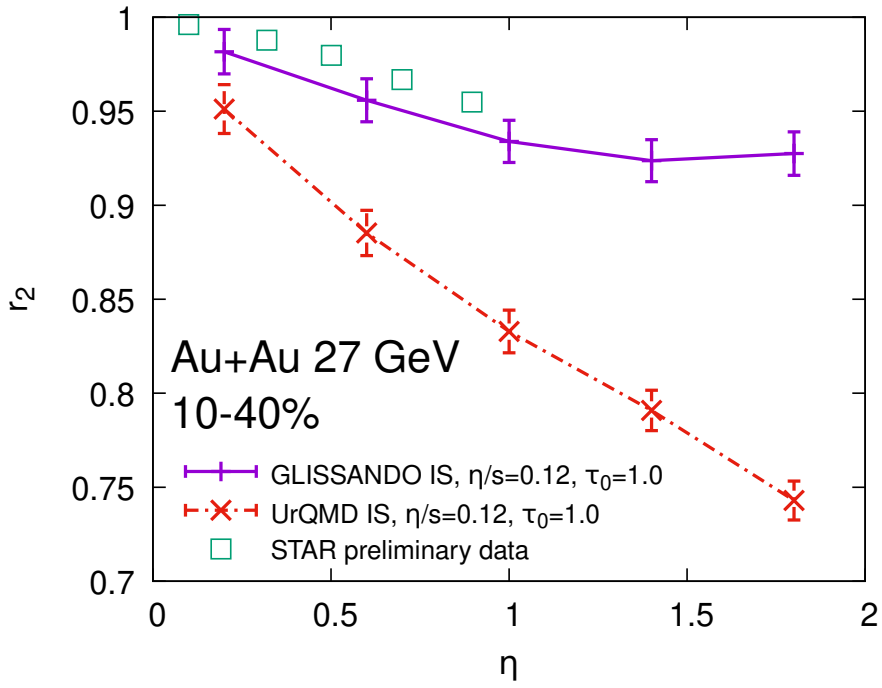

Figure 5.18: Factorization ratio r_2 as a function of pseudorapidity in 10-40% central Au+Au collisions at $\sqrt{s_{\mathrm{NN}}} = 27$ GeV obtained from hybrid model `vHLLE+UrQMD` with `GLISSANDO` and `UrQMD` IS. The preliminary experimental data points are from STAR collaboration [81].

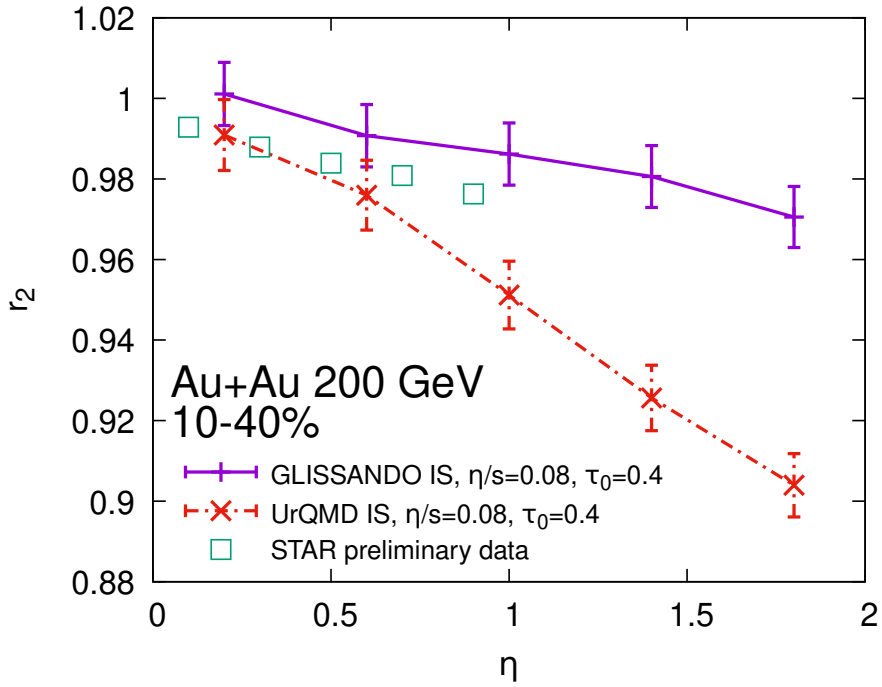

Figure 5.19: Same as Fig. 5.18, but for $\sqrt{s_{\mathrm{NN}}} = 200$ GeV Au+Au collisions. The preliminary experimental data points are from STAR collaboration [82].

ing Eqs. (3.42). These contributions are shown in Fig. 5.20 for $\sqrt{s_{\mathrm{NN}}} = 27\,\mathrm{GeV}$ and in Fig. 5.21 for $\sqrt{s_{\mathrm{NN}}} = 200\,\mathrm{GeV}$. It can be seen that both models at both energies predict the same result; the flow angle decorrelation plays a more important role than the flow magnitude decorrelation. The same result has been observed in calculations at LHC energies [139].

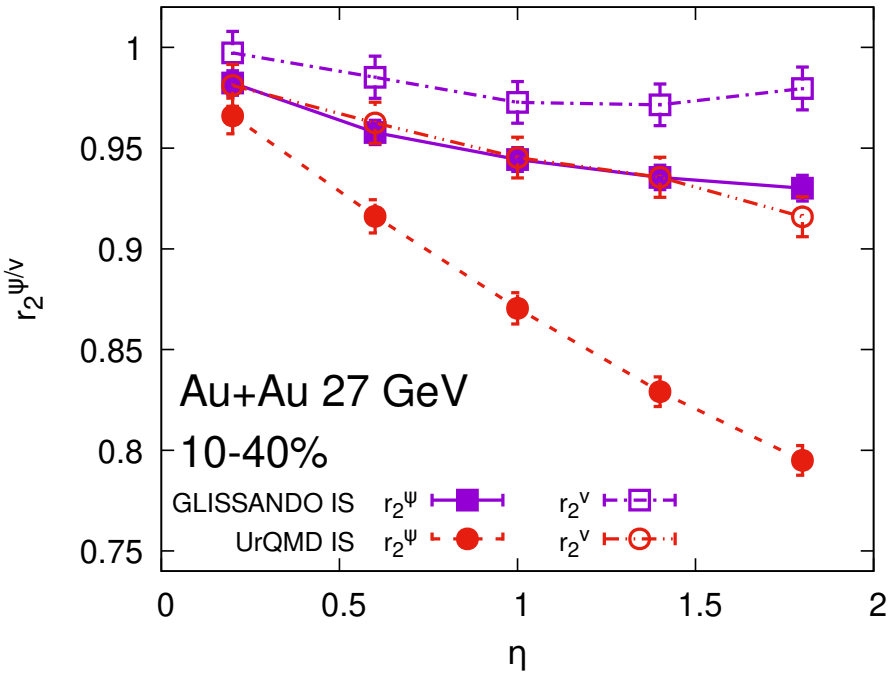

Figure 5.20: The flow magnitude decorrelation r_2^v and the flow angle decorrelation r_2^ψ as functions of pseudorapidity in 10-40% central Au+Au collisions at $\sqrt{s_{\mathrm{NN}}} = 27\,\mathrm{GeV}$ obtained from hybrid model `vHLLE+UrQMD` with `GLISSANDO` and `UrQMD` IS.

To understand the big difference between IS models, we define the factorization ratio of the initial-state eccentricity.

$$r_n^\varepsilon(\eta_s) = \frac{\langle \varepsilon_n(-\eta_s)\varepsilon_n(\eta_{s,\mathrm{ref}})\cos[n\,(\Psi_n(-\eta_s) - \Psi_n(\eta_{s,\mathrm{ref}}))]\rangle}{\langle \varepsilon_n(\eta_s)\varepsilon_n(\eta_{s,\mathrm{ref}})\cos[n\,(\Psi_n(\eta_s) - \Psi_n(\eta_{s,\mathrm{ref}}))]\rangle}. \tag{5.31}$$

This observable demonstrates the decorrelation of the anisotropy in the initial state. For the calculations, we use the same intervals of η_s as for pseudorapidity. Figures 5.22 and 5.23 show the factorization ratio r_2^ε as a function of the space-time rapidity at $\sqrt{s_{\mathrm{NN}}} = 27$ and $200\,\mathrm{GeV}$, respectively. When comparing these graphs with the factorization ratio r_2 in Figs. 5.18 and 5.19, one can notice that r_2 and r_2^ε almost quantitatively agree. More interestingly, r_2^ε is a coordinate-space characteristic of the initial state, while r_2 is a momentum-space characteristic of the final state. Their agreement means that decorrelation of the anisotropic flow origins in the initial state and is transferred to the final state via hydro-

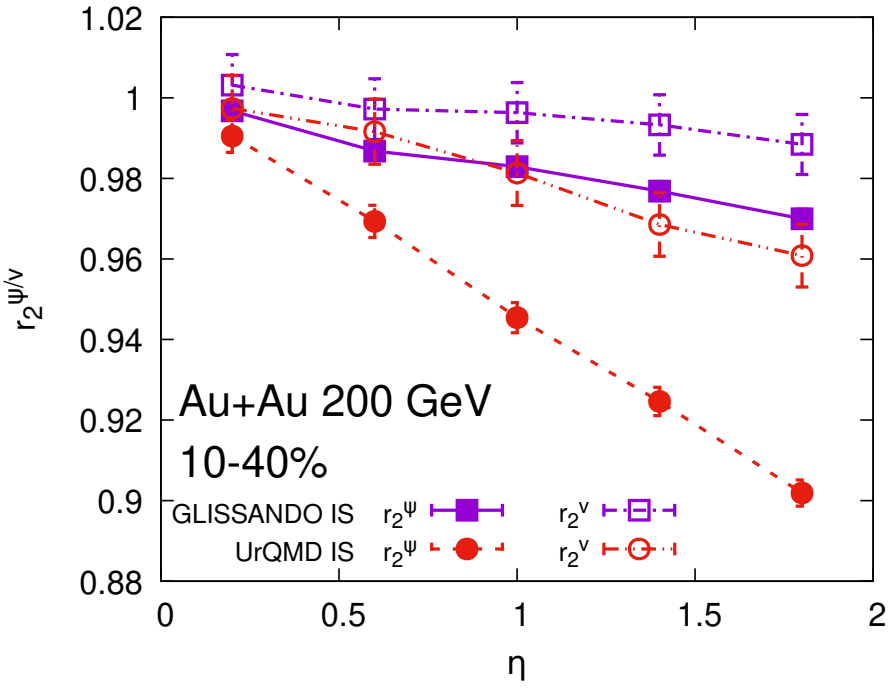

Figure 5.21: Same as Fig. 5.20, but for $\sqrt{s_{\rm NN}} = 200$ GeV Au+Au collisions.

dynamic evolution as in the case of correspondence between the initial-state eccentricity and the final-state flow coefficient [68].

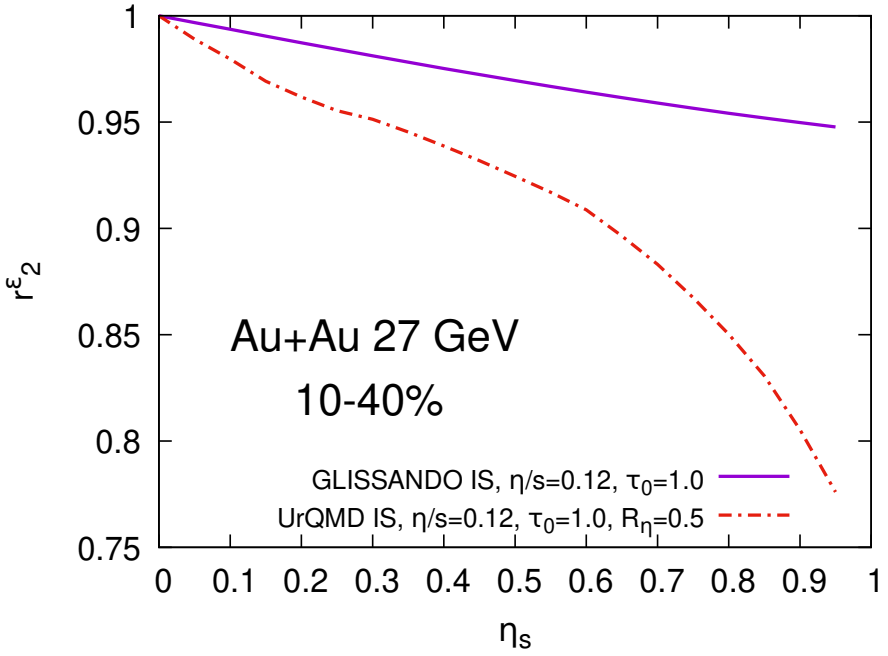

Figure 5.22: The longitudinal decorrelation of the initial-state eccentricity r_2^{ε} as a function of space-time rapidity in 10-40% central Au+Au collisions at $\sqrt{s_{\rm NN}} = 27$ GeV obtained from hybrid model `vHLLE+UrQMD` with `GLISSANDO` and `UrQMD` IS.

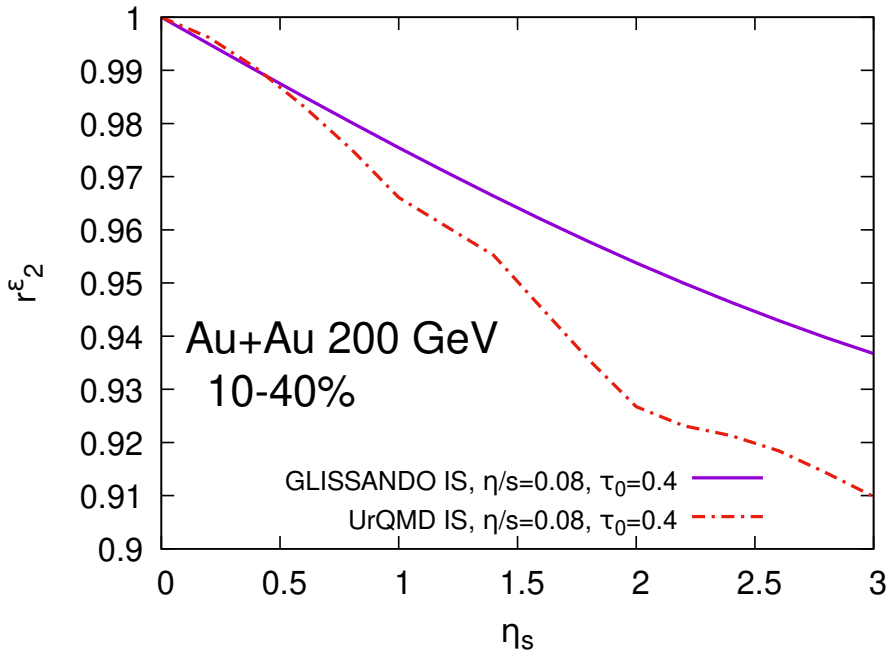

Figure 5.23: Same as Fig. 5.22, but for $\sqrt{s_{\mathrm{NN}}} = 200$ GeV Au+Au collisions.

5.6 Predictions for Experiment AFTER@LHC

There is a proposal for A Fixed Target Experiment at LHC (AFTER@LHC) [144–146], which should start in CERN in the near future. Since it is a fixed-target experiment, it will cover far backward rapidity of the collision, and thus it is very useful to study the longitudinal structure of various observables. Therefore, we computed predictions of Pb beam colliding with W, Ti, and C targets at $\sqrt{s_{\mathrm{NN}}} = 72$ GeV, which is the energy at which the experiment will work. We started by calculating the prediction of the pseudorapidity distribution of charged hadrons with `UrQMD` and `GLISSANDO` IS models, which is shown in Fig. 5.24.

Figure 5.25 shows the prediction of the elliptic flow calculated using the EP method for the Pb+W, Pb+Ti and Pb+C collisions. For Pb+W collisions, both IS models predict almost identical elliptic flow, whereas for more asymmetric collisions the predictions differ. The `UrQMD` IS predicts even lower elliptic flow in Pb+Ti collisions than in Pb+C collisions at backward rapidity, which means that there is a non-monotonic behaviour.

We also calculated the prediction of the longitudinal decorrelation for the experiment AFTER@LHC. However, these collisions are asymmetric and, therefore, we use the symmetric factorization ratio defined in [77] as:

$$\sqrt{r_n(\eta,\eta_{\mathrm{ref}})r_n(-\eta,-\eta_{\mathrm{ref}})} = \sqrt{\frac{\langle q_n(-\eta)q_n^*(\eta_{\mathrm{ref}})\rangle}{\langle q_n(\eta)q_n^*(\eta_{\mathrm{ref}})\rangle}\frac{\langle q_n(\eta)q_n^*(-\eta_{\mathrm{ref}})\rangle}{\langle q_n(-\eta)q_n^*(-\eta_{\mathrm{ref}})\rangle}}. \tag{5.32}$$

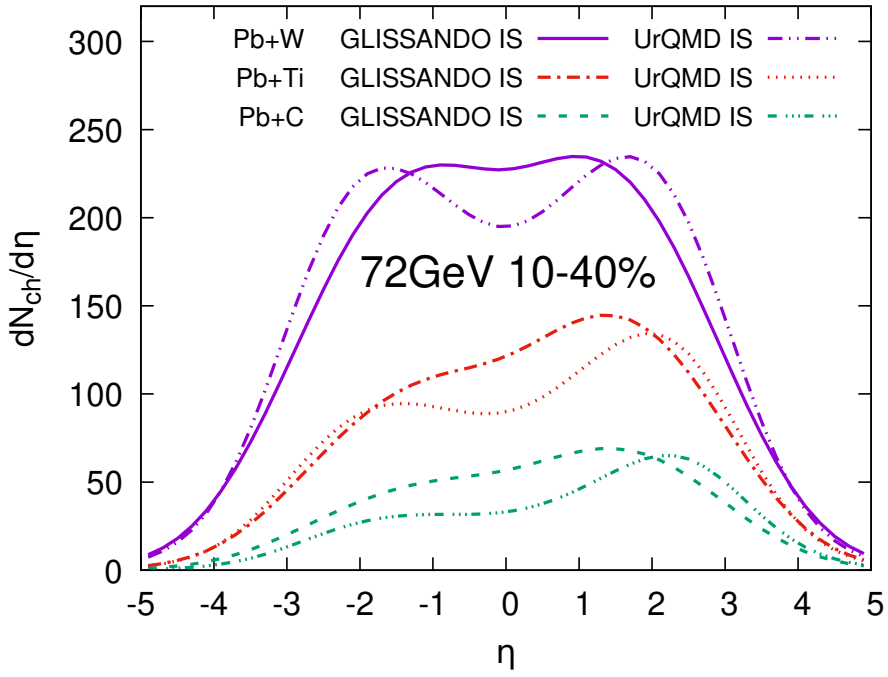

Figure 5.24: Prediction of pseudorapidity distribution of charged hadrons for 10-40% Pb+W, Pb+Ti and Pb+C collisions at $\sqrt{s_{\mathrm{NN}}} = 72$ GeV obtained from hybrid model `vHLLE+UrQMD` with `GLISSANDO` and `UrQMD` IS.

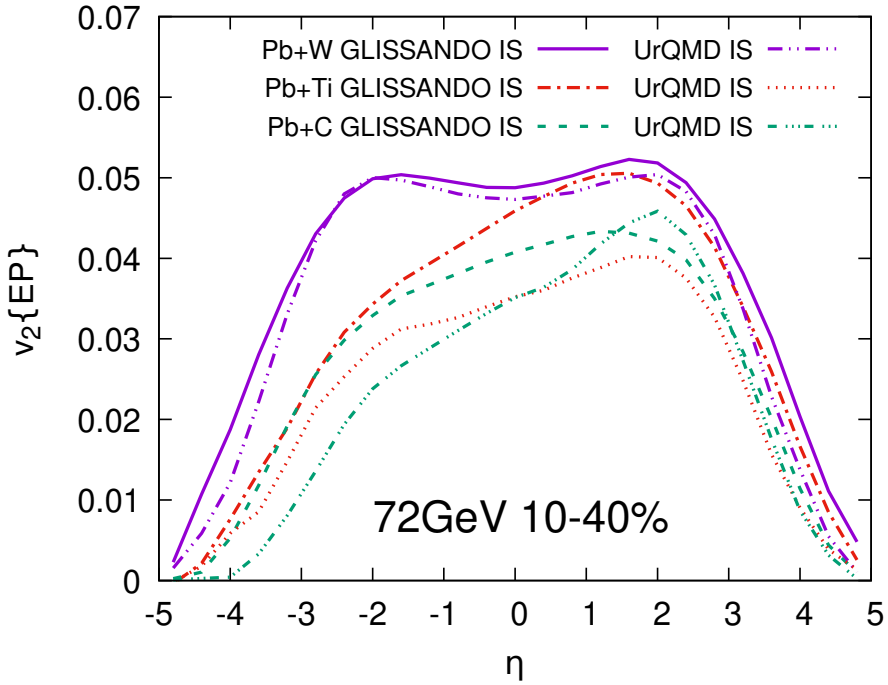

Figure 5.25: Prediction of elliptic flow as a function of pseudorapidity for 10-40% Pb+W, Pb+Ti and Pb+C collisions at $\sqrt{s_{\mathrm{NN}}} = 72$ GeV obtained from hybrid model `vHLLE+UrQMD` with `GLISSANDO` and `UrQMD` IS.

Figure 5.26 shows the prediction of the symmetric factorization ratio as a function of pseudorapidity for all three collision systems. For this calculation, we used the pseudorapidity reference bin $2.1 < \eta_{\text{ref}} < 5.1$ and p_T cut $0.4 < p_T < 4.0$ GeV. Consistent with the results of the previous section, the UrQMD IS predicts a much stronger decorrelation for the three collision systems. Both IS models predict monotonic hierarchy between collision systems: weakest decorrelation in Pb+W collisions and strongest decorrelation in Pb+C collisions.

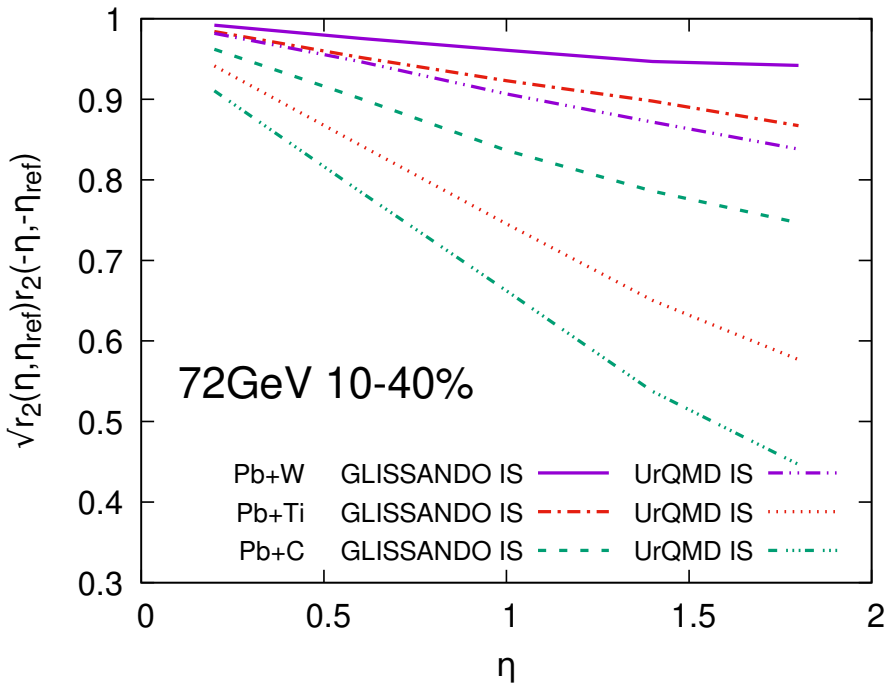

Figure 5.26: Prediction of the symmetric factorization ratio $\sqrt{r_2(\eta, \eta_{\text{ref}}) r_2(-\eta, -\eta_{\text{ref}})}$ as a function of pseudorapidity for 10-40% Pb+W, Pb+Ti and Pb+C collisions at $\sqrt{s_{\text{NN}}} = 72$ GeV obtained from hybrid model vHLLE+UrQMD with GLISSANDO and UrQMD IS.

Unfortunately, the experiment AFTER@LHC will not provide the full pseudorapidity region. The experiment is planned to have two acceptance windows: $-1.0 < \eta < -0.5$ and $-2.9 < \eta < -1.6$ in the center-of-mass frame. Therefore, we need to adjust the formula for the calculation of the longitudinal decorrelation. The first acceptance window can be used as a reference bin $-1.0 < \eta_{\text{ref}} < -0.5$ and the second acceptance window $-2.9 < \eta < -1.6$ can be used for the measurement itself, where we can calculate the decorrelation around the center of the window $\eta_C = -2.25$. The fixed-target factorization ratio can be calculated by

$$r_n^{\text{FT}}(\eta - \eta_C) = \frac{\langle q_n(-\eta + 2\eta_C) q_n^*(\eta_{\text{ref}}) \rangle}{\langle q_n(\eta) q_n^*(\eta_{\text{ref}}) \rangle} . \tag{5.33}$$

Figure 5.27 shows the prediction of the fixed-target factorization ratio as a func-

tion of $\eta - \eta_C$ for the three collision systems. In this prediction, both IS models predict similar results for Pb+W and Pb+Ti collisions, while for Pb+C collisions UrQMD IS predicts much stronger decorrelation. Moreover, in the case of GLISSANDO IS the monotonic hierarchy is broken as it predicts stronger decorrelation for Pb+Ti collisions than for Pb+C collisions.

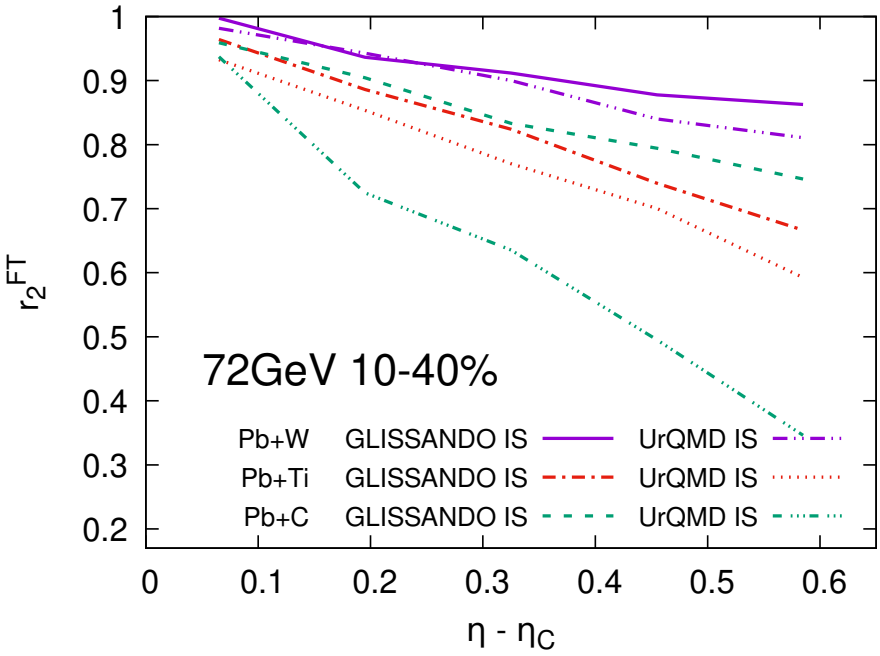

Figure 5.27: Prediction of the fixed-target factorization ratio r_2^{FT} as a function of $\eta - \eta_C$ for 10-40% Pb+W, Pb+Ti and Pb+C collisions at $\sqrt{s_{\mathrm{NN}}} = 72$ GeV obtained from hybrid model vHLLE+UrQMD with GLISSANDO and UrQMD IS.

Chapter 6

Three-Fluid Hydrodynamic Model

6.1 Motivation

The first part of the motivation are the current and future experiments operating at low energies, which aim to explore the QCD phase diagram and search for the CEP. There is the BES program running at RHIC. The first phase of the BES [147] ended in 2014 and covered the energies $\sqrt{s_{\mathrm{NN}}} = 7.7\,\mathrm{GeV}$, $11.5\,\mathrm{GeV}$, $14.5\,\mathrm{GeV}$, $19.6\,\mathrm{GeV}$, $27\,\mathrm{GeV}$, $39\,\mathrm{GeV}$, $62.4\,\mathrm{GeV}$, and $200\,\mathrm{GeV}$. The currently running second phase called BES Phase-II [148] focusses on energies from 7 to $20\,\mathrm{GeV}$ in collider mode and from 3 to $7\,\mathrm{GeV}$ in the fixed target regime. The other running experiment is the NA61/SHINE experiment [149] at the SPS at CERN, which performs system size and collision energy scan. This facility covers the range $\sqrt{s_{\mathrm{NN}}} = 5$ to $17\,\mathrm{GeV}$.

Furthermore, two experiments are under construction. The accelerator complex called Nuclotron-based Ion Collider fAcility (NICA) [150] is being built in Dubna. It will cover energies $\sqrt{s_{\mathrm{NN}}} = 4$ to $11\,\mathrm{GeV}$. The other experiment being built is the Compressed Baryonic Matter (CBM) [151] experiment at the international Facility for Antiproton and Ion Research (FAIR) in Darmstadt. The energy range of CBM should be in the range $\sqrt{s_{\mathrm{NN}}} = 2.7$ to $5\,\mathrm{GeV}$.

Another experiment is also planned at Japan Proton Accelerator Research Complex (J-PARC). The future heavy-ion program (J-PARC-HI) [152] should provide uranium beams with $\sqrt{s_{\mathrm{NN}}} = 1.9$ to $6.2\,\mathrm{GeV}$, however, the first beams are not expected before 2026.

The second part of the motivation is that most of the hydrodynamic models mentioned in Sect.4.3 are not suitable for energies lower than $\sqrt{s_{\mathrm{NN}}} \approx 10\,\mathrm{GeV}$. The hydrodynamic modeling of such low energies brings new challenges. Many models assume zero baryon density, which is acceptable for top RHIC and LHC energies, but it is necessary to assume finite baryon density for low energies.

Another challenge is to include the complex geometry of the initial state. At collision energies $\sqrt{s_{\mathrm{NN}}} = 200\,\mathrm{GeV}$ and higher, the Lorentz contraction of the incoming nuclei is strong enough so that a picture of "thin pancakes" applies. Namely, in the center-of-mass frame, two incoming nuclei can be approximated by infinitely thin pancakes which inter-penetrate each other. In the absence of a longitudinal scale, the resulting expansion of the produced medium can be represented by a scaling flow $v_z = z/t$. The latter results in a longitudinally boost-invariant distribution of produced secondary hadrons. As such, the pre-equilibrium and fluid dynamical modelling may be reduced from 3- to 2-dimensional, utilizing the symmetry in longitudinal direction. However, as the collision energy decreases, the Lorentz contraction becomes weaker and the picture of thin pancakes breaks down. There starts to be a finite inter-penetration time of the colliding nuclei, which may become comparable to the lifetime of the following fluid phase. This means that while some nucleons have already collided, contributing to the dense core of the system, other nucleons are still approaching the positions of their first scatterings. In addition, when the created medium passes close to the critical point on its thermodynamic trajectory during the expansion phase, the correlation length in the medium increases sharply. The increase in the correlation length can be pronounced by the emergence of non-hydrodynamic modes [12]. Furthermore, many of the existing codes assume a boost-invariant longitudinal expansion following the Bjorken model. However, that would lead to a longitudinally infinite fireball.

Chapter 5 shows that it is possible to adjust IS models built for higher energies to reproduce the experimental data at a few tens of GeV quite well; however, a complicated longitudinal parametrization with several free parameters was needed. Furthermore, at $\sqrt{s_{\mathrm{NN}}} = 27\,\mathrm{GeV}$ the values of the parameters change even with centrality.

Addressing the above-mentioned challenges is essential to construct a consistent fluid-dynamic model for simulations of heavy-ion collisions from a few to tens of GeV.

6.2 Initial Conditions

The initial state at low energies may last up to several fm/c. Thus, the transition from the initial state to the hydrodynamic phase must happen gradually. This may be treated in two ways: dynamical fluidization and/or three-fluid hydrodynamics [101]. In the former solution, once the primary nucleon-nucleon scattering occurs anywhere in the system, its products are transferred into the

fluid part and removed from the cascade. This approach allows us to separate the collision zone into a high-energy density part, called a core, and a peripheral smaller energy density part, called a corona. The core-corona separation [153] is especially important in peripheral collisions and at low energies.

The three-fluid hydrodynamic model treats the incoming nuclei as two baryon-rich fluids, and the newly produced matter as a time-delayed third baryon-free (i.e. with zero net baryonic charge) fluid. The third fluid is created by the friction of the two colliding fluids. In this way, it is possible to simulate the finite stopping power and particle production at BES energies. The three-fluid model is an extension of the two-fluid model with direct pion emission [154] and the (2+1)-fluid model [155].

The three-fluid model was used by its authors to describe various experimental observables, e.g., directed flow [156], elliptic flow [157], bulk properties [158] or light nuclei production [159]. Unfortunately, the existing version of the three-fluid hydrodynamic model has several shortcomings. First, it lacks viscous corrections. The hydrodynamic grid is defined in Cartesian coordinates, which is reasonable only for energies not larger than 30 GeV. The model has averaged initial conditions, which means that its odd harmonics of the flow are equal to 0. And the EoS is hard-coded, which is unfortunate if you are trying to find out which EoS works best near the CEP.

Our model uses the three-fluid approach. Therefore, the first step of the model is to generate nuclei before the collision. The initial state geometry is formulated in Milne coordinates instead of Cartesian, so the model will be valid for energies $\sqrt{s_{\mathrm{NN}}} > 100$ GeV as well as for lower energies.

To achieve event-by-event simulations, the positions of the nucleons are sampled according to the Woods-Saxon formula [160]

$$\rho(x, y, z) = \frac{\rho_0}{1 + \exp\left(\frac{\sqrt{x^2+y^2+z^2}-R}{a}\right)}, \tag{6.1}$$

where $a = 0.459$ fm is a diffuseness and R is the nuclear radius obtained by Eq. (5.4). In the code, the Cartesian coordinates x, y, and z are uniformly sampled from the interval $(-R-4\,\mathrm{fm}; R+4\,\mathrm{fm})$. After that, the nucleon is either accepted or discarded by comparing a random number from the interval $(0; \rho_0)$ with Eq. (6.1). The overlap of nucleons is not forbidden. This algorithm produces a spherical nucleus in Cartesian coordinates (Fig. 6.1). The next step is to contract the

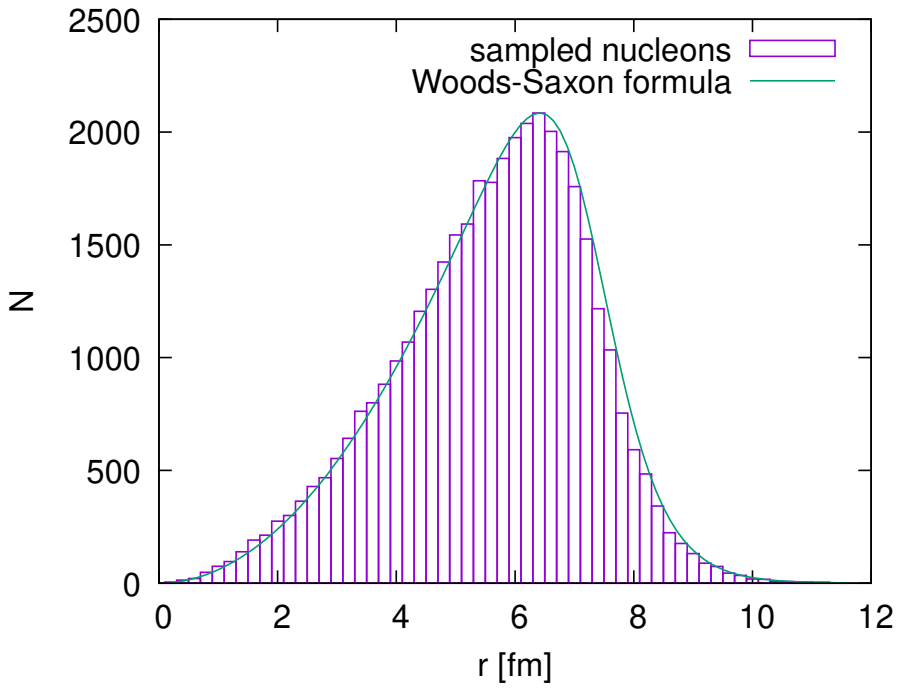

Figure 6.1: Radii of the generated nucleons compared to Woods-Saxon formula multiplied by Jacobian r^2.

longitudinal direction with the γ-factor obtained from the collision energy

$$v_{\text{coll}} = \sqrt{1 - \left(\frac{2m_N}{\sqrt{s_{\text{NN}}}}\right)^2}, \tag{6.2a}$$

$$\gamma = \frac{1}{\sqrt{1 - v_{\text{coll}}^2}}, \tag{6.2b}$$

where v_{coll} is the collision velocity. Then we move the longitudinal coordinate of the contracted projectile by $-2R/\gamma$ and the target by $+2R/\gamma$. One can argue that translation by $\pm R/\gamma$ should be enough; however, the Woods-Saxon formula has a tail, which causes the nuclei to overlap already at τ_0 in this case.

At this point, the nucleons are transformed to Milne coordinates and moved to the hypersurface $\tau = \tau_0$ (see Fig. 6.2). Here, τ_0 is simply a technical parameter that controls the curvature of the hypersurface (see Fig. 6.3). Now, consider a nucleon from the target nucleus at coordinate $x^\mu = (\tau_0, x, y, z)$, which is moving with velocity $-v_{\text{coll}}$. The following equation applies to the longitudinal coordinate at hypersurface $\tau = \tau_0$:

$$z - v_{\text{coll}}(t - \tau_0) = \tau_0 \sinh \eta_s,$$
$$z - v_{\text{coll}}\tau_0(\cosh \eta_s - 1) = \tau_0 \sinh \eta_s.$$

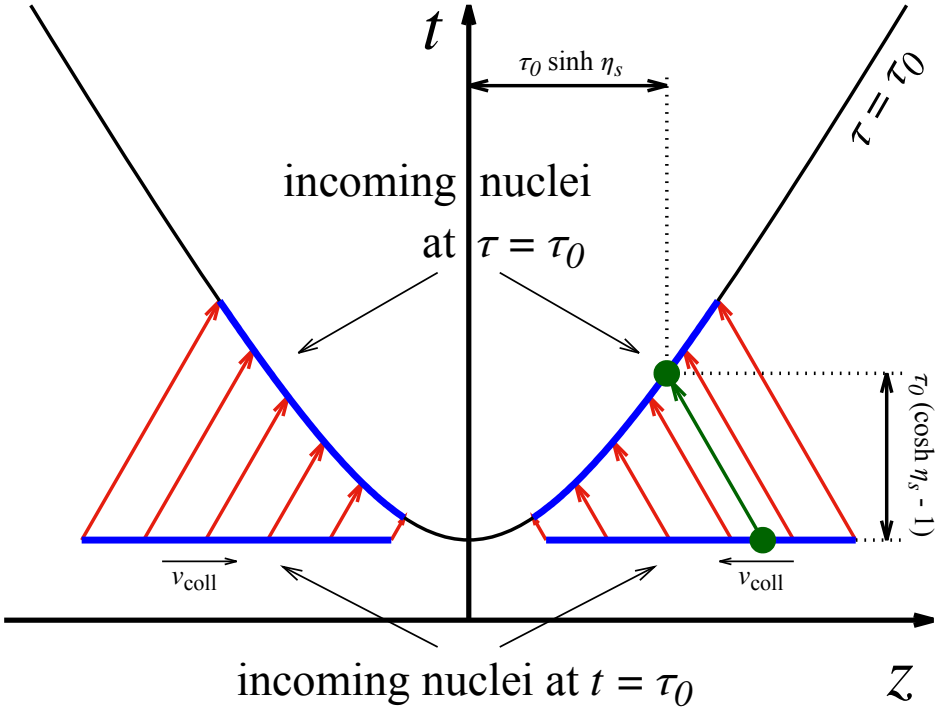

Figure 6.2: Sketch of the nuclei transformation from Cartesian to Milne coordinates at hypersurface $\tau = \tau_0$.

Now, using $v_{\text{coll}} = \tanh \text{y}$, the equation can be modified further:

$$\begin{aligned} z - \tau_0 \tanh \text{y} &= \tau_0(\sinh \eta_s + \tanh \text{y} \cosh \eta_s), \\ z \cosh \text{y} - \tau_0 \sinh \text{y} &= \tau_0 \sinh(\eta_s + \text{y}), \\ \eta_s &= \operatorname{asinh}\left(\frac{z}{\tau_0} \cosh \text{y} + \sinh \text{y}\right) - \text{y}. \end{aligned} \tag{6.3}$$

The equation for projectile nucleons can be derived analogously, resulting in the following:

$$\eta_s = \operatorname{asinh}\left(\frac{z}{\tau_0} \cosh \text{y} - \sinh \text{y}\right) + \text{y}. \tag{6.4}$$

6.2.1 Impact Parameter

The centrality of the events is controlled through the impact parameter. The user sets its minimum and maximum values. The impact parameter is then generated in the two-dimensional plane as the position of the second nucleus (the first is at coordinates $[0; 0]$) and if the size of the impact parameter lies between the minimal and maximum value, it is accepted. The projectile and target nuclei are then moved by $\pm b/2$ along the x-axis.

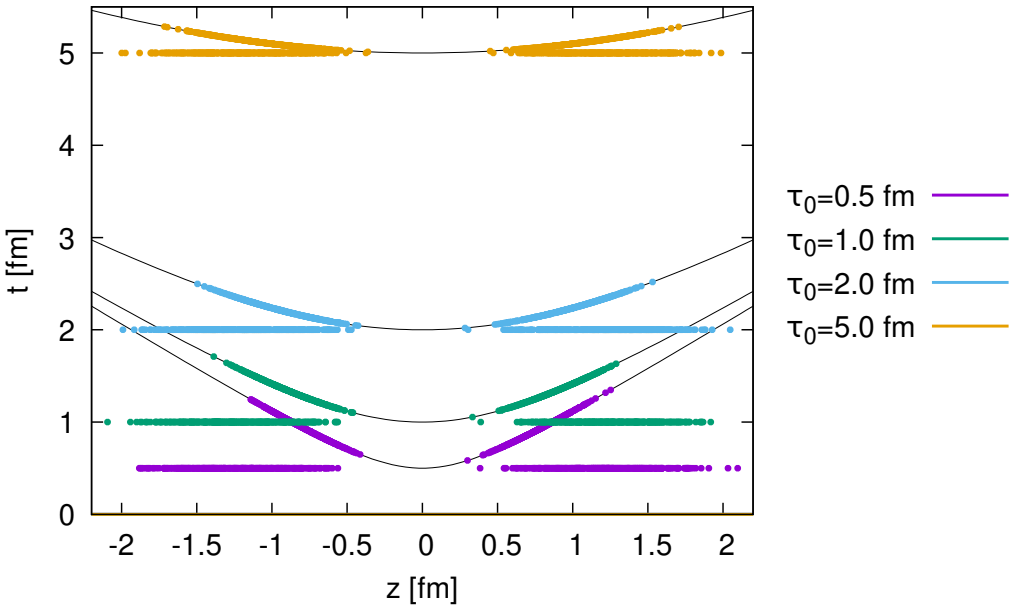

Figure 6.3: Transformation of sampled nucleons from $t = \tau_0$ (horizontal lines) to hypersurface $\tau = \tau_0$ (hyperbolic curves) for different values of parameter τ_0 in Cartesian coordinates. Black solid lines correspond to coordinates with constant τ.

6.2.2 Particles-to-Fluid Transition

Once the nucleons have been generated, they are transformed into fluids. To smoothly deposit four-momentum, baryon density, and electric charge into hydrodynamic cells the smoothing kernel is used [161]. In Cartesian coordinates and the rest frame of a particle, the kernel takes the form

$$K(\Delta\vec{r}_{\text{rest}}) = A \exp\left(-\frac{\Delta\vec{r}^{\,2}_{\text{rest}}}{2\sigma^2}\right), \tag{6.5}$$

where $\Delta\vec{r}$ is the distance between the hydrodynamic cell and the position of the nucleon, and A is a numerically computed normalization so that the total energy, the baryon number, and the electric charge are conserved. In a moving frame, this equation changes into

$$K(\Delta\vec{r}) = A \exp\left(-\frac{\Delta\vec{r}^{\,2} + (\Delta\vec{r}\cdot\vec{u})^2}{2\sigma^2}\right). \tag{6.6}$$

Since the nucleons move only along the longitudinal direction, the kernel can be further derived:

$$\begin{aligned} K(\Delta x, \Delta y, \Delta\eta_s) &= A \exp\left(-\frac{\Delta x^2 + \Delta y^2 + \Delta z^2(1 + (u^z)^2)}{2\sigma^2}\right) = \\ &= A \exp\left(-\frac{\Delta x^2 + \Delta y^2 + \Delta\eta_s^2\tau^2 \cosh^2\eta_s \cosh^2 \mathrm{y}}{2\sigma^2}\right). \end{aligned} \tag{6.7}$$

At this point, the hydro cells contain properly distributed energies, momenta, electric and baryon charges of the nucleons from the initial state, and the hydrodynamic evolution may start.

6.3 Hydrodynamic Evolution

At each timestep in our three-fluid approach, first, the evolution of individual fluids is performed, and then the interactions between fluids are computed. The hydrodynamics of individual fluids is calculated using the vHLLE code, which is described in detail in Sect. 5.1.2. Although the vHLLE algorithm can compute viscous hydrodynamics, the three-fluid model described in this chapter works only for perfect fluids so far.

6.3.1 CFL Criterion

In any hydrodynamic code, the timestep and grid sizes cannot have arbitrary values, but they must satisfy a Courant-Friedrichs-Lewy (CFL) condition [162]. In one dimension, the criterion is

$$\Delta x \geq c \cdot \Delta\tau, \tag{6.8}$$

where $\Delta\tau$ is the timestep and Δx is the grid spacing. This condition says that the time step has to be small enough so that the fastest signal, the speed of light, does not propagate across a cell within a single timestep. In Milne coordinates, the propagation speed in the longitudinal direction is multiplied by a factor $1/\tau$ and the criterion is

$$\tau\Delta\eta \geq c \cdot \Delta\tau. \tag{6.9}$$

In three dimensions, the CFL criterion must be satisfied in each direction.

Moreover, the model has to watch out for numerical diffusion as well. Therefore, it is recommended to set the timestep that meets the conditions

$$\Delta x \geq c\Delta\tau \geq 0.1\Delta x, \tag{6.10a}$$

$$\Delta y \geq c\Delta\tau \geq 0.1\Delta y, \tag{6.10b}$$

$$\tau\Delta\eta \geq c\Delta\tau \geq 0.1\tau\Delta\eta \tag{6.10c}$$

and optimally setting $\Delta\tau = 0.5\Delta x = 0.5\Delta y = 0.5\tau\Delta\eta$.

Since the code allows setting arbitrary grid parameters and timestep, it contains a check for the CFL criterion. In case any of the conditions in Eqs. (6.10) is violated, the respective grid spacing is resized to the optimal value.

Condition Eq. (6.10c) cannot be fulfilled with increasing time, and therefore the model resizes the grid as soon as the condition ceases to apply. At this point, the timestep and grid spacing in x and y directions is multiplied by 2. Thus, Eqs. (6.10a) and (6.10b) will not change, while Eq. (6.10c) again becomes satisfied.

6.3.2 Interaction between Fluids

The formulation of the three-fluid approximation is based on the non-equilibrium distribution functions of the projectile (p), target (t), and fireball (f). These distribution functions are coupled by a set of relativistic Boltzmann equations

$$p_\mu \partial_x^\mu f_\mathsf{p}(x,p) = C_\mathsf{p}(f_\mathsf{p}, f_\mathsf{t}) + C_\mathsf{p}(f_\mathsf{p}, f_\mathsf{f}), \tag{6.11a}$$

$$p_\mu \partial_x^\mu f_\mathsf{t}(x,p) = C_\mathsf{t}(f_\mathsf{p}, f_\mathsf{t}) + C_\mathsf{t}(f_\mathsf{t}, f_\mathsf{f}), \tag{6.11b}$$

$$p_\mu \partial_x^\mu f_\mathsf{f}(x,p) = C_\mathsf{f}(f_\mathsf{p}, f_\mathsf{t}) + C_\mathsf{f}(f_\mathsf{p}, f_\mathsf{f}) + C_\mathsf{f}(f_\mathsf{t}, f_\mathsf{f}). \tag{6.11c}$$

The coefficients C_α are the collision terms between the three fluids. The inter-fluid terms ($C_{\mathsf{p/t}}(f_\mathsf{p}, f_\mathsf{t})$, $C_{\mathsf{p/t}}(f_{\mathsf{p/t}}, f_\mathsf{f})$, $C_\mathsf{f}(f_{\mathsf{p/t}}, f_\mathsf{f})$) represent the friction between the fluids, and the term $C_\mathsf{f}(f_\mathsf{p}, f_\mathsf{t})$ is there for the production of particles from the colliding nuclei.

By integrating Eqs. (6.11a)-(6.11c) over momentum and summing over particle species, one obtains the equations of the energy-momentum exchange between the fluids

$$\partial_\mu T_\mathsf{p}^{\mu\nu}(x) = -F_\mathsf{p}^\nu(x) + F_\mathsf{fp}^\nu(x), \tag{6.12a}$$

$$\partial_\mu T_\mathsf{t}^{\mu\nu}(x) = -F_\mathsf{t}^\nu(x) + F_\mathsf{ft}^\nu(x), \tag{6.12b}$$

$$\partial_\mu T_\mathsf{f}^{\mu\nu}(x) = F_\mathsf{p}^\nu(x) + F_\mathsf{t}^\nu(x) - F_\mathsf{fp}^\nu(x) - F_\mathsf{ft}^\nu(x), \tag{6.12c}$$

where F_α^ν are the friction forces. From these equations it is obvious that the total energy-momentum is conserved

$$\partial_\mu (T_\mathsf{p}^{\mu\nu} + T_\mathsf{t}^{\mu\nu} + T_\mathsf{f}^{\mu\nu}) = 0. \tag{6.13}$$

Since the code works with tilded components, we may also define tilded source terms:

$$\tilde{F}_\alpha^\mu = \{F_\alpha^\tau, F_\alpha^x, F_\alpha^y, \tau F_\alpha^\eta\}. \tag{6.14}$$

The energy-momentum exchange then can be written as:

$$\tau\tilde{\partial}_\mu \tilde{T}_\mathsf{p}^{\mu\nu}(x) = -\tau\tilde{F}_\mathsf{p}^\nu(x) + \tau\tilde{F}_\mathsf{fp}^\nu(x), \tag{6.15a}$$

$$\tau\tilde{\partial}_\mu \tilde{T}_\mathsf{t}^{\mu\nu}(x) = -\tau\tilde{F}_\mathsf{t}^\nu(x) + \tau\tilde{F}_\mathsf{ft}^\nu(x), \tag{6.15b}$$

$$\tau\tilde{\partial}_\mu \tilde{T}_\mathsf{f}^{\mu\nu}(x) = \tau\tilde{F}_\mathsf{p}^\nu(x) + \tau\tilde{F}_\mathsf{t}^\nu(x) - \tau\tilde{F}_\mathsf{fp}^\nu(x) - \tau\tilde{F}_\mathsf{ft}^\nu(x). \tag{6.15c}$$

Projectile-Target Friction

In the original three-fluid hydrodynamic model [101], the friction forces between the projectile and the target fluids are given by

$$F_\alpha^\nu = \vartheta^2 \rho_{\mathsf{p}}^\xi \rho_{\mathsf{t}}^\xi m_N V_{\mathsf{rel}}^{\mathsf{pt}} \left[(u_\alpha^\nu - u_{\overline{\alpha}}^\nu)\sigma_P(s_{\mathsf{pt}}) + (u_{\mathsf{p}}^\nu + u_{\mathsf{t}}^\nu)\sigma_E(s_{\mathsf{pt}}) \right], \tag{6.16}$$

where ϑ is the overall factor associated with the unification of the projectile and the target fluids, $\alpha = \mathsf{p}$ or t, $\overline{\mathsf{p}} = \mathsf{t}$ and $\overline{\mathsf{t}} = \mathsf{p}$, ρ_α^ξ are scalar densities, m_N is the mass of the nucleon, $V_{\mathsf{rel}}^{\mathsf{pt}}$ is the mean relative velocity of baryon-rich fluids defined by

$$V_{\mathsf{rel}}^{\mathsf{pt}} = \frac{\sqrt{s_{\mathsf{pt}}(s_{\mathsf{pt}} - 4m_N^2)}}{2m_N^2}, \tag{6.17}$$

$s_{\mathsf{pt}} = m_N^2(u_{\mathsf{p}}^\nu + u_{\mathsf{t}}^\nu)^2$ is the square of the mean invariant energy of the colliding nucleons, and $\sigma_{P/E}$ are cross-sections defined as

$$\sigma_P(s_{\mathsf{pt}}) = \int_{\theta_{cm}<\pi/2} \mathsf{d}\sigma^{NN\to NX} \left(1 - \cos\theta_{cm} \frac{p_{out}}{p_{in}}\right), \tag{6.18a}$$

$$\sigma_E(s_{\mathsf{pt}}) = \int_{\theta_{cm}<\pi/2} \mathsf{d}\sigma^{NN\to NX} \left(1 - \frac{E_{out}}{E_{in}}\right). \tag{6.18b}$$

The scalar densities ρ_α^ξ contain switch between baryonic and quark matter:

$$\rho_\alpha^\xi(s_{\mathsf{pt}}) = \begin{cases} \rho_\alpha^b \xi_h(s_{\mathsf{pt}}) & \varepsilon_\alpha < 0.7\,\mathsf{GeV/fm^3}, \\ \frac{1}{3}\left(\rho_\alpha^q + \rho_\alpha^g\right)\xi_q(s_{\mathsf{pt}}) & \varepsilon_\alpha > 0.7\,\mathsf{GeV/fm^3}. \end{cases} \tag{6.19}$$

Here, ρ_α^b, ρ_α^q and ρ_α^g are scalar densities of net baryons, quarks, and gluons, respectively, and ξ_h and ξ_q are tuning parameters. The scaling factor $1/3$ is there to compensate for the number of valence quarks in baryons. Since the code evolves only the baryon density, the quark and gluon densities are approximated for zero quark mass following [163]:

$$\rho_\alpha^q = \frac{18\zeta(3)}{\pi^2} T^3 + 2\mu_q^3, \tag{6.20a}$$

$$\rho_\alpha^g = \frac{16\zeta(3)}{\pi^2} T^3. \tag{6.20b}$$

Here, ζ is Riemann zeta function and μ_q is quark chemical potential.

Friction between Fireball and Baryon-Rich Fluids

The interaction between baryon-rich and fireball fluids is dominated by the absorption of a fireball pion by a nucleon with the formation of a resonance. The corresponding friction force between the two fluids is given by

$$F_{\mathsf{f}\alpha}^\nu(x) = \rho_\alpha^b \xi_{\mathsf{f}\alpha}(s_{\mathsf{f}\alpha}) V_{\mathsf{rel}}^{\mathsf{f}\alpha} \frac{T_{\mathsf{f}(eq)}^{0\nu}}{u_{\mathsf{f}}^0} \sigma_{tot}^{N\pi\to R}(s_{\mathsf{f}\alpha}), \tag{6.21}$$

where $\xi_{\mathsf{f}\alpha}(s_{\mathsf{f}\alpha})$ is the tuning parameter, $s_{\mathsf{f}\alpha} = (m_\pi u_{\mathsf{f}} + m_M u_\alpha)^2$ and $V_{\mathsf{rel}}^{\mathsf{f}\alpha}$ is the mean invariant relative velocity between baryon-rich and fireball fluids defined as

$$V_{\mathsf{rel}}^{\mathsf{f}\alpha} = \frac{\sqrt{(s_{\mathsf{f}\alpha} - m_N^2 - m_\pi^2)^2 - 4m_N^2 m_\pi^2}}{2m_N m_\pi}. \tag{6.22}$$

6.4 Equation of State

The challenge of obtaining the EoS at high baryon density and temperature is one of the objectives these days. Unlike at the top RHIC and LHC energies, where it is sufficient to assume zero baryon density, and hence it is possible to use the results of lattice QCD [50, 164], the low-energy collisions call for high baryon density. The high baryon density EoS must agree with the available results at zero baryon density. Currently, there are several developed families of the EoS parametrizations. Parotto et al. created an EoS family [165] by combining the Taylor expansion of the pressure around $\mu_B = 0$ and the 3D Ising model, which should be able to describe the singular behaviour at and around the CEP. The non-critical Taylor expansion valid at small μ_B is defined by

$$P(T, \mu_B) = T^4 \sum_n c_{2n}(T) \left(\frac{\mu_B}{T}\right)^{2n}. \tag{6.23}$$

The Taylor coefficients can be written as the susceptibilities of the baryon number

$$c_n(T) = \frac{1}{n!} \frac{\partial^n P/T^4}{\partial(\mu_B/T)^n}\bigg|_{\mu_B=0} = \frac{1}{n!}\chi_n(T). \tag{6.24}$$

The full pressure is then completed by adding the critical contribution from the Ising model

$$P(T, \mu_B) = T^4 \sum_n c_{2n}^{\mathsf{Non-Ising}}(T) \left(\frac{\mu_B}{T}\right)^{2n} + T_C^4 P^{\mathsf{Ising}}(T, \mu_B). \tag{6.25}$$

This EoS is visualized in Figure 6.4, for the critical baryonic chemical potential chosen as $\mu_{BC} = 350\,\mathsf{MeV}$ and the corresponding critical temperature $T_C \approx 143.2\,\mathsf{MeV}$.

Ma et al. [166] started with a quasi-particle QGP (qQGP) model [167]. Quasi-particles correspond to gluons and u, d, and s quarks. The model has the pressure defined as

$$\frac{PV}{T} = \mp \sum_{k=0}^{\infty} \mathsf{ln}(1 \mp z e^{-\beta\epsilon_k}) + \int \mathsf{d}\beta\beta \frac{\partial m}{\partial \beta} \left\langle \frac{\partial E_r}{\partial m} \right\rangle. \tag{6.26}$$

Here, the upper sign is for fermions and the lower sign is for bosons, $\beta = 1/T$, m is the mass, $z = e^{\mu/T}$ is called fugacity, and ϵ_k are single particle energy levels.

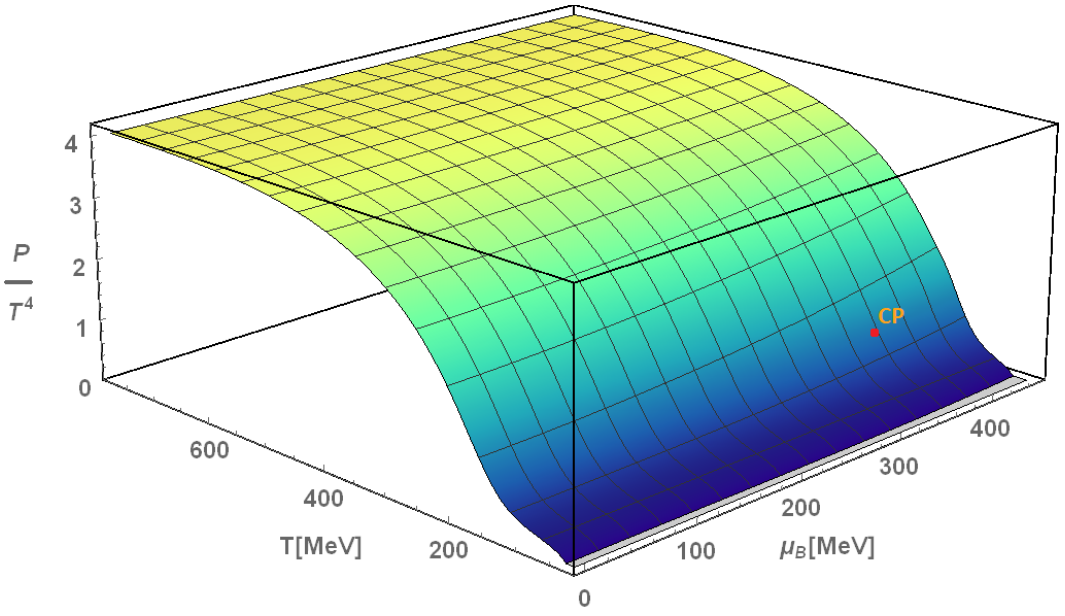

Figure 6.4: The EoS obtained by combining Taylor expansion around $\mu_B = 0$ and 3D Ising model. Taken from [165].

The critical point is then added to this model phenomenologically according to the scheme

$$(P - P_Q)(P - P_H) = \delta(\mu_B, T), \tag{6.27}$$

where P_Q is the pressure given by the MIT bag model and P_H is the pressure given by the Hadronic Resonance Gas (HRG) model [168]. The function $\delta(\mu_B, T)$ is defined as

$$\delta(\mu, T) = \delta_0(T) \exp\left[-\left(\frac{\mu_B}{\mu_{BC}}\right)^4\right]. \tag{6.28}$$

The function $\delta_0(T)$ is chosen as

$$\delta_0(T) = \begin{cases} \delta_0 e^{-c(T-T_p)^2}, & T \leq T_p \\ \delta_0, & T_p < T \leq T_p + 0.02 \\ \delta_0 e^{-c(T-T_p-0.02)^2}. & T > T_p + 0.02 \end{cases} \tag{6.29}$$

Their results with $\mu_{BC} = 300$ MeV are shown in Figure 6.5.

Another method to obtain the EoS at high baryon density is to use an imaginary chemical potential to avoid the sign problem [170].

To begin with, we chose an effective chiral hadron-quark EoS model [124] that includes the correct asymptotic degrees of freedom. Figure 6.6 shows their results at the vanishing net baryon density compared to lattice QCD data. This EoS is used in hydrodynamic evolution; however, we switch to the SMASH Hadronic Resonance Gas EoS model described in [171] to compute the temperature and chemical potentials at the hypersurface of fluid-to-particle transition. This is

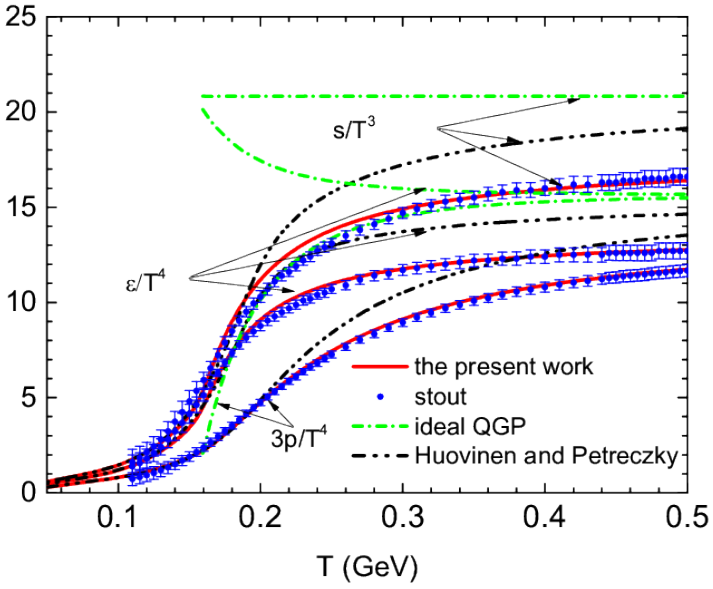

Figure 6.5: The pressure, entropy and energy density obtained by combining quasi-particle QGP model and phenomenological critical point (red lines). The model is compared with lattice QCD data (blue points), Huovinen and Petreczky [169] (black lines) and MIT bag model (green lines). The figure shows pressure, entropy and energy density. Taken from [166].

necessary for the conservation of the quantum number in the particlization process, where the thermodynamic properties of the fluid in the hypersurface cells have to correspond to those in the afterburner evolution.

6.5 Particlization and Fluid-to-Particle Transition

The fluid-to-particle transition in 3-fluid hydrodynamics is more complicated than in the 1-fluid hydro. In a 1-fluid hydrodynamic model, the freeze-out happens at a point, when the energy density drops below some critical value

$$\varepsilon < \varepsilon_{\text{crit}}. \tag{6.30}$$

In the case of three fluids, the most intuitive way to manage the freeze-out is to sum the energy-momentum tensors of all three fluids, diagonalize the result, and then check analogously when the resulting value drops below $\varepsilon_{\text{crit}} = 0.5\,\text{GeV}/\text{fm}^3$. The diagonalization of the energy-momentum tensor can be written as

$$T^{\mu}_{\nu} u^{\nu} = \varepsilon u^{\mu}. \tag{6.31}$$

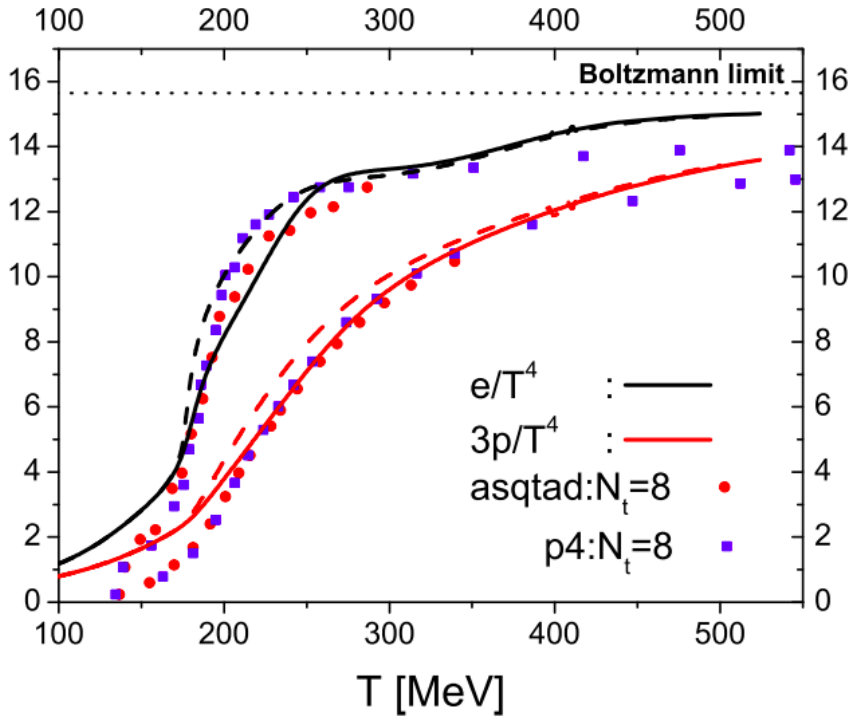

Figure 6.6: The EoS obtained by effective chiral hadron-quark model. The model is compared with lattice QCD data. The figure shows pressure and energy density over T^4. Taken from [124].

The diagonalization results in four eigenvalues and eigenvectors. Compared to T^μ_ν in the local rest frame

$$T^\mu_\nu = (\varepsilon + P)u^\mu u_\nu - P\delta^\mu_\nu = \begin{pmatrix} \varepsilon & 0 & 0 & 0 \\ 0 & -P & 0 & 0 \\ 0 & 0 & -P & 0 \\ 0 & 0 & 0 & -P \end{pmatrix}, \tag{6.32}$$

one of the eigenvalues will be the total energy density, and it will be the one with the corresponding eigenvector satisfying $u^\mu u_\mu > 0$, that is, the property of four-velocity.

Once the total energy density is obtained, the freeze-out hypersurface can be reconstructed. For this, the Cornelius subroutine [125] is used. It takes four-dimensional cubes with energy densities of neighbouring hydrodynamic cells in the corners of the cubes as input. Using interpolation, it finds out if and where the critical energy density lies, connects those points, and reconstructs the surface element.

The next step of the model is to sample hadrons using the Cooper-Frye prescription defined by Eq. (5.28). Now, the problem arises: there is only one hy-

persurface, but three fluids with three velocities that are generally different, and one velocity obtained from the diagonalization procedure that "washes out" the absence of equilibrium between the fluids which co-exist in the same space-time domain. Therefore, the model generates three freeze-out hypersurfaces, one for each fluid, with the same hypersurface elements, but different velocities, temperatures, and chemical potentials.

Another thing that is different in three-fluid hydrodynamics is that at τ_0 the nuclei just start to collide, and thus the energy density is below $\varepsilon_{\mathrm{crit}}$ everywhere. Therefore, the reconstructed freeze-out hypersurface is fully closed (see Fig. 6.7). In such a case, there should be total net energy flow through the hypersurface, which is given via:

$$\varepsilon_{\mathrm{totSurf}} = \sum_{\alpha} (\varepsilon_\alpha + P_\alpha) \left(\cosh \eta_s u_\alpha^\tau + \sinh \eta_s \tau u_\alpha^\eta\right) u^\nu \mathrm{d}\Sigma_\nu - \\ - P_\alpha \left(\cosh \eta_s \mathrm{d}\Sigma_\tau - \sinh \eta_s \frac{1}{\tau} \mathrm{d}\Sigma_\eta\right), \tag{6.33}$$

equal to zero. This works as a simple test of the freeze-out procedure.

The multi-fluid dynamics brings up one more issue. There could be particles moving inward through the hypersurface, and thus would end up with negative Cooper-Frye contributions. This model uses a simple algorithm (Fig. 6.8) to disregard such cells. This algorithm is run for each fluid separately. Figure 6.9 shows elements of the freeze-out hypersurface of individual fluids that pass this algorithm and are sent to the next phase of the model. It can be seen that, at an early time, elements at forward space-time rapidity will produce particles only from the projectile fluid because it moves from negative to positive space-time rapidity and, therefore, its velocity at negative space-time rapidity is heading inside the QGP. For the same reason, elements at backward space-time rapidity will produce particles only from the target fluid.

Although the algorithm rejects many problematic elements, the Cooper-Frye formula contains the term $\mathrm{d}\Sigma_\mu(x)p^\mu$, which may still be negative. Since p^μ is the momentum of the particle to be sampled, we cannot reject these elements during the hydrodynamic phase, in which the freeze-out hypersurface is reconstructed. As a test of how much these negative contributions affect the resulting spectra, we calculated direct Cooper-Frye integrals from the hypersurface cells (Fig. 6.10). This figure, plotted for $\sqrt{s_{\mathrm{NN}}} = 7.7$ GeV, shows that negative contributions affect mainly low-p_T up to 10%, while the slope of the spectrum is not affected. At higher collision energies, this effect is even smaller. In conclusion, one does not have to worry about the negative Cooper-Frye contributions in our model.

To better reproduce the experimental setup, it is practical to sample the

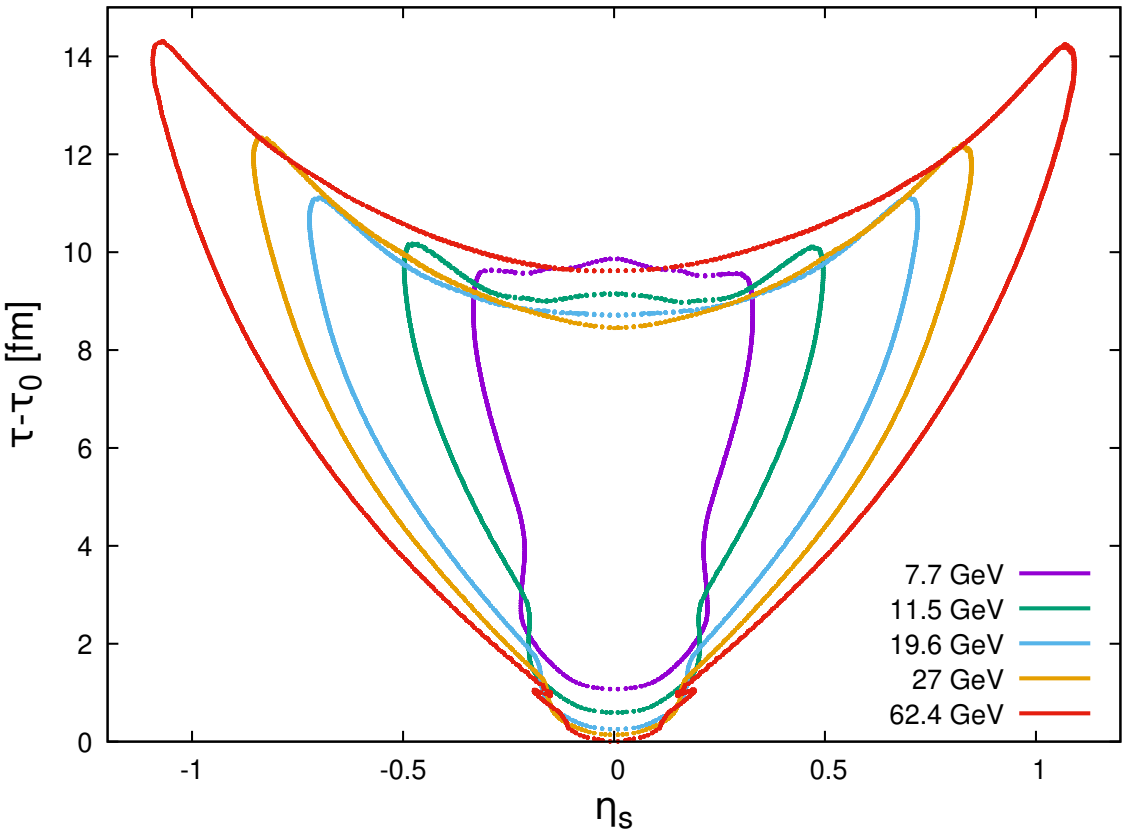

Figure 6.7: Time evolution of elements of the freeze-out hypersurface along longitudinal direction (within $\sqrt{x^2+y^2} < 0.4$ fm) at different BES energies with impact parameter $b = 0$.

produced particles using a Monte Carlo procedure instead of calculating the Cooper-Frye integrals directly once the freeze-out hypersurface is reconstructed. DRoplet and hAdron Generator for Nuclear collisions (DRAGON) [172, 173] is such a tool. It is based on the Blast-wave (BW) model [174]. In addition, it can decay resonance cascades. Unfortunately, DRAGON assumes that the freeze-out happens at the constant proper time, which is contrary to the results of hydrodynamics. Another similar tool, which can take any shape of the freeze-out hypersurface as input, is called THERMINATOR2 [112]. However, both codes lack the viscous corrections in the Cooper-Frye formula. Therefore, our model uses SMASH hadron sampler [175] based on the algorithm described in Sec. 5.1.3.

6.6 Final-State Interactions

Finally, our model is coupled with the newly developed microscopic transport model SMASH [176]. This code includes many possible processes, which can

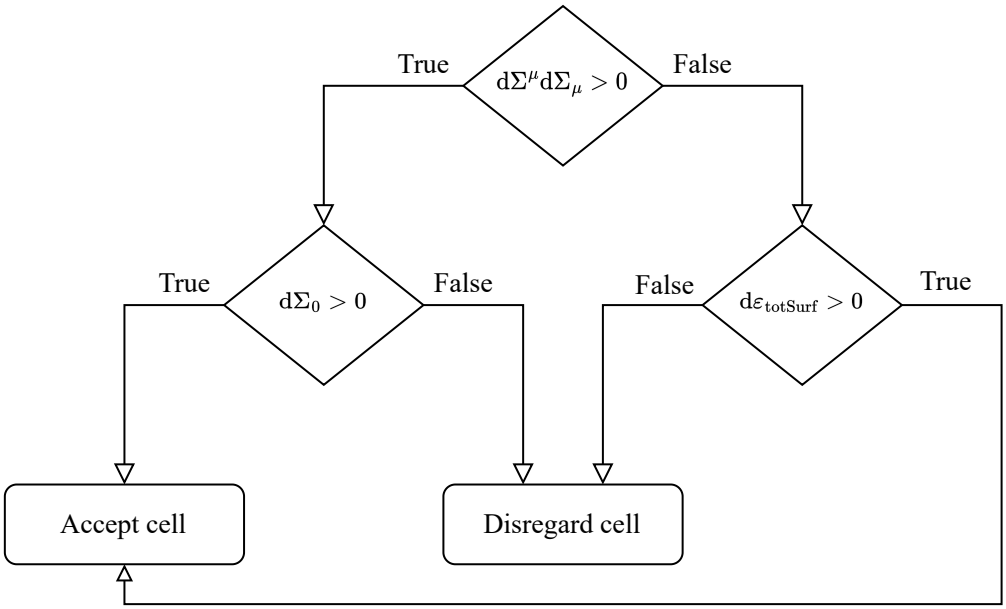

Figure 6.8: Diagram of the algorithm accepting and rejecting cells of freeze-out hypersurface.

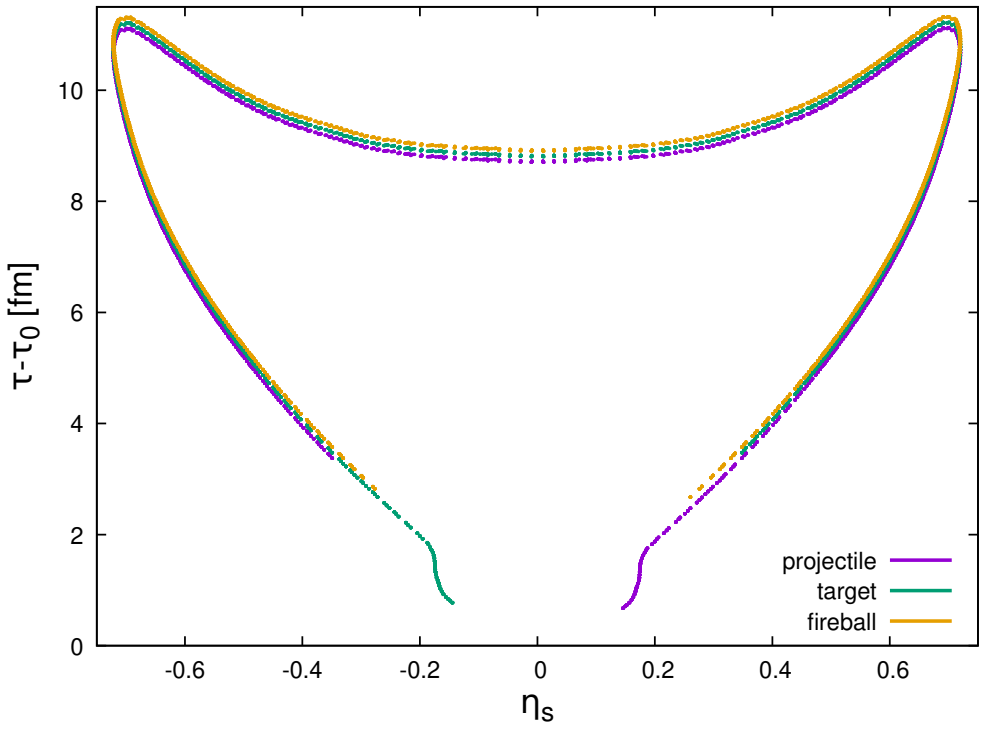

Figure 6.9: Elements of freeze-out hypersurface of individual fluids at $\sqrt{s_{\mathrm{NN}}} = 19.6$ GeV after passing through the algorithm presented in Fig. 6.8. Points are slightly shifted in the vertical direction, so they can be plotted on a single graph.

happen after the particlization, e.g. resonance decays, 2 particles inelastic and elastic scatterings, and resonance excitations.

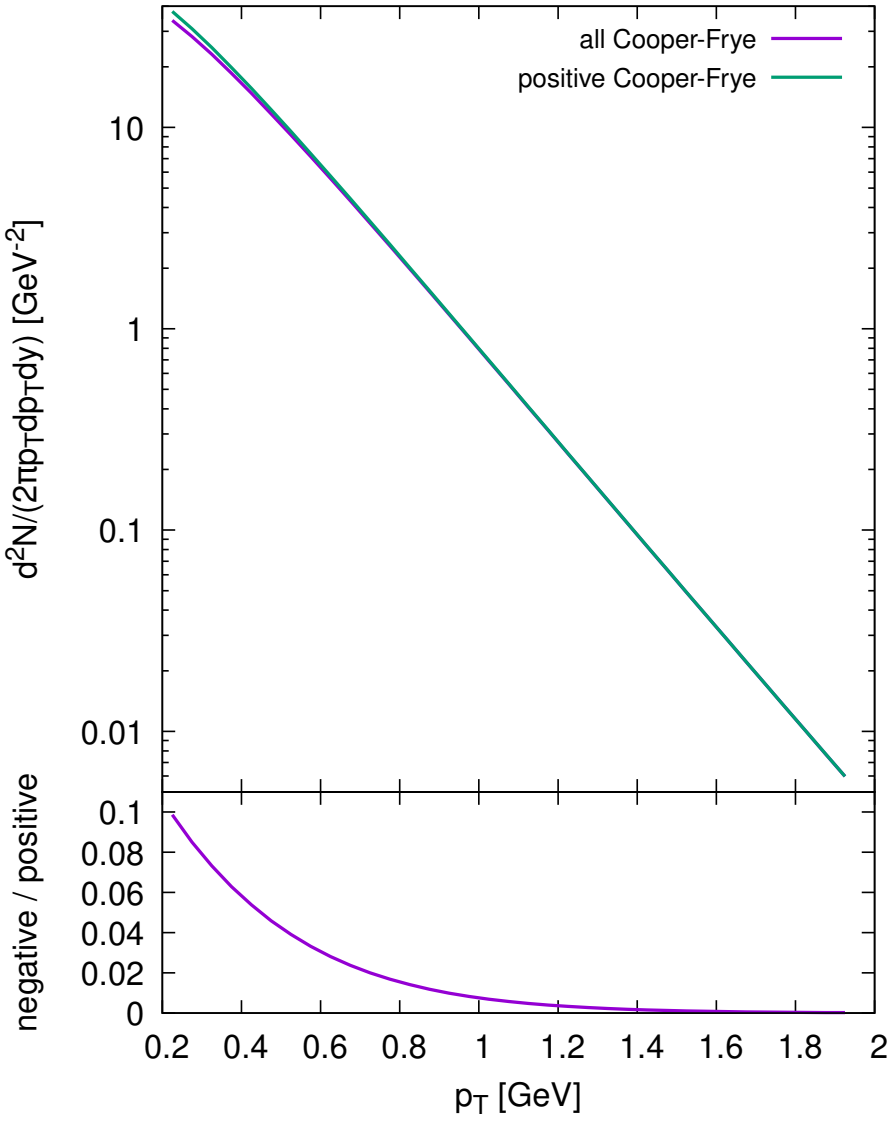

Figure 6.10: Transverse momentum spectrum calculated using Cooper-Frye integrals from the freeze-out hypersurface at $\sqrt{s_{\mathrm{NN}}} = 7.7\,\mathrm{GeV}$. The bottom plot shows ratio of negative to positive contributions to the spectrum.

Chapter 7

Results

In this chapter, we present the first results of our state-of-the-art 3-Fluid Hydrodynamic (3FH) model with event-by-event fluctuating initial conditions and the perfect-fluid hydrodynamics. We simulated Au+Au collisions at 6 BES energies: $\sqrt{s_{\mathsf{NN}}} = 7.7$, 11.5, 19.6, 27, 39, and 62.4 GeV. For each energy we have run 3000 hydrodynamic simulations, and from each simulation we produced 500 final-state events, resulting in $1.5 \cdot 10^6$ events per energy.

7.1 Fine Tuning

To reproduce the experimental data, the friction terms need to be fine-tuned through parameters ξ_h, ξ_q, and $\xi_{\mathsf{f}\alpha}$. These parameters were tuned on p_T spectra of pions, kaons, and protons at energies $\sqrt{s_{\mathsf{NN}}} = 7.7$ - 62.4 GeV [58, 59] and on rapidity distributions of net-protons at $\sqrt{s_{\mathsf{NN}}} = 17.2$ and 62.4 GeV [126, 127]. Since 3-fluid hydrodynamics has three times higher consumption of CPU time and memory, we again adjusted the parameters based on the visual correspondence with the data rather than calculating the χ^2 distribution. The tuning process indicated that the parameters should have different values for different collision energies. However, elements of the two fluids that collide in one cell have only information about their current mean invariant colliding energy and not about the initial collision energy. Therefore, instead, we made the parameters ξ dependent on the invariant energy of the fluid elements. We have tried several polynomial dependences on the invariant energy to best describe the amount of energy transferred through friction at different collision energies. As a result of the tuning process, the best combined reproduction of experimental data was obtained with the following parameter values:

$$\xi_h = 1.8\sqrt{\frac{2m_N}{\sqrt{s_{\mathsf{pt}}}}}, \quad \xi_q = 30\sqrt{\frac{2m_N}{\sqrt{s_{\mathsf{pt}}}}}, \quad \xi_{\mathsf{f}\alpha} = 0.15\frac{m_N^2}{s_{\mathsf{f}\alpha}}. \tag{7.1}$$

These values were used to produce the results for this chapter.

7.2 Centrality Determination

In STAR experiment, centrality bins are determined from the total raw number of charged particles inside $|\eta| < 0.5$ [177] rather than from the impact parameter, as it cannot be measured directly in the experiment. To better reproduce the experimental setup, we used the same quantity to determine the centrality bins. Since the borders of $\mathrm{d}N_{\mathrm{ch}}/\mathrm{d}\eta$ used for the determination of centrality in the experiment STAR are not published, we followed their procedure [178] to obtain them. This procedure is described in the following paragraphs.

Since the precision of our model in the most peripheral collisions has not yet been studied, we simulated events with an impact parameter in the range $(0; 12)$ fm. This corresponds to the centrality of ca $0 - 60$%. However, from such data, it is impossible to determine the centrality classes. Therefore, we used a two-component model [179] that only works with the early collisions of the incident nucleons to reproduce the multiplicity distribution from our model. This model assumes that the multiplicity in nuclear collisions has two contributions: the "soft" part, which is proportional to the mean number of participants $\langle N_{\mathrm{part}} \rangle$, and the "hard" part, which is proportional to the mean number of binary collisions $\langle N_{\mathrm{coll}} \rangle$. The number of charged particles per unit of pseudorapidity is then calculated as follows:

$$\frac{\mathrm{d}N_{\mathrm{ch}}}{\mathrm{d}\eta} = n_{pp} \left[(1-x) \frac{\langle N_{\mathrm{part}} \rangle}{2} + x \langle N_{\mathrm{coll}} \rangle \right]. \tag{7.2}$$

Here, n_{pp} is the average multiplicity in minimum-bias $p+p$ collisions, and x is the fraction of the hard component. However, we don't know yet the mean numbers of participants and binary collisions. Therefore, we simulated event-by-event N_{part} and N_{coll} using the Glauber Monte Carlo (GMC) model [180]. From these, we calculated the estimated number of charged particles N:

$$N = n_{pp} \left[(1-x) \frac{N_{\mathrm{part}}}{2} + x N_{\mathrm{coll}} \right]. \tag{7.3}$$

Finally, we used convolution of Negative Binomial Distributions (NBD) N-times producing the final multiplicity in each GMC event used to make the multiplicity distribution

$$P_{\mathrm{NBD}}(n_{pp}, k; n) = \frac{\Gamma(n+k)}{\Gamma(n+1)\Gamma(k)} \frac{(n_{pp}/k)^n}{(n_{pp}/k+1)^{n+k}}, \tag{7.4}$$

where Γ is the Gamma function and k is a distribution parameter. The two-component GMC model produces a multiplicity distribution that perfectly reproduces the distribution shape of the 3FH model.

The next step was to fine-tune the multiplicity distribution from the 3FH model with the GMC model. For this, we used the values $k = 2.1$ and $x = 0.11$ from [178], and n_{pp} was the tuning parameter to fit the distribution of the most central collisions. The values of n_{pp} obtained from the fits for different BES energies are listed in Table 7.1.

$\sqrt{s_{\mathsf{NN}}}$ [GeV]	σ_{NN} [mb]	n_{pp}
7.7	30.6	0.89
11.5	31.28	0.99
19.6	32.3	1.11
27	33.1	1.16
39	34.2	1.23
62.4	35.9	1.36

Table 7.1: Parameters of the 2-component Glauber Monte Carlo model, inelastic nucleon-nucleon cross-section σ_{NN} and the average multiplicity in minimum bias $p + p$ collisions n_{pp}, for BES energies.

Finally, there is a significant difference between the number of events per number of charged particles as a result of not simulating minimum-bias events. To correct for this effect, the ratio of the GMC simulation to the 3-fluid simulation of events with $N_{\mathsf{ch}} > 50$ was used as a scaling factor. The resulting multiplicity distributions with Glauber fits and marked centrality bins are shown in Fig. 7.1 and the borders of the centrality bins are listed in Table 7.2. The table also lists the impact parameter, the mean number of participants $\langle N_{\mathsf{part}} \rangle$, and the mean number of binary collisions $\langle N_{\mathsf{coll}} \rangle$ extracted from the GMC model. These values are just informative and do not play any role in determining centrality bins.

7.3 Rapidity Distributions

We start with pseudorapidity distributions of charged hadrons. Although there are experimental data only for $\sqrt{s_{\mathsf{NN}}} = 19.6$ and 62.4 GeV [57], we show the pseudorapidity distributions for all studied energies. To reproduce the experimental analysis, we excluded weak contributions for these calculations. Figures 7.2-7.7 show the pseudorapidity distributions at energies $\sqrt{s_{\mathsf{NN}}} = 7.7$, 11.5, 19.6, 27, 39, and 62.4 GeV, respectively. From these figures it can be seen that at larger energies the rapidity distribution develops a two-peak structure, which can also be observed in simulations by the hybrid model with `UrQMD` IS presented in Fig. 5.3. Comparison with experimental data shows an underestima-

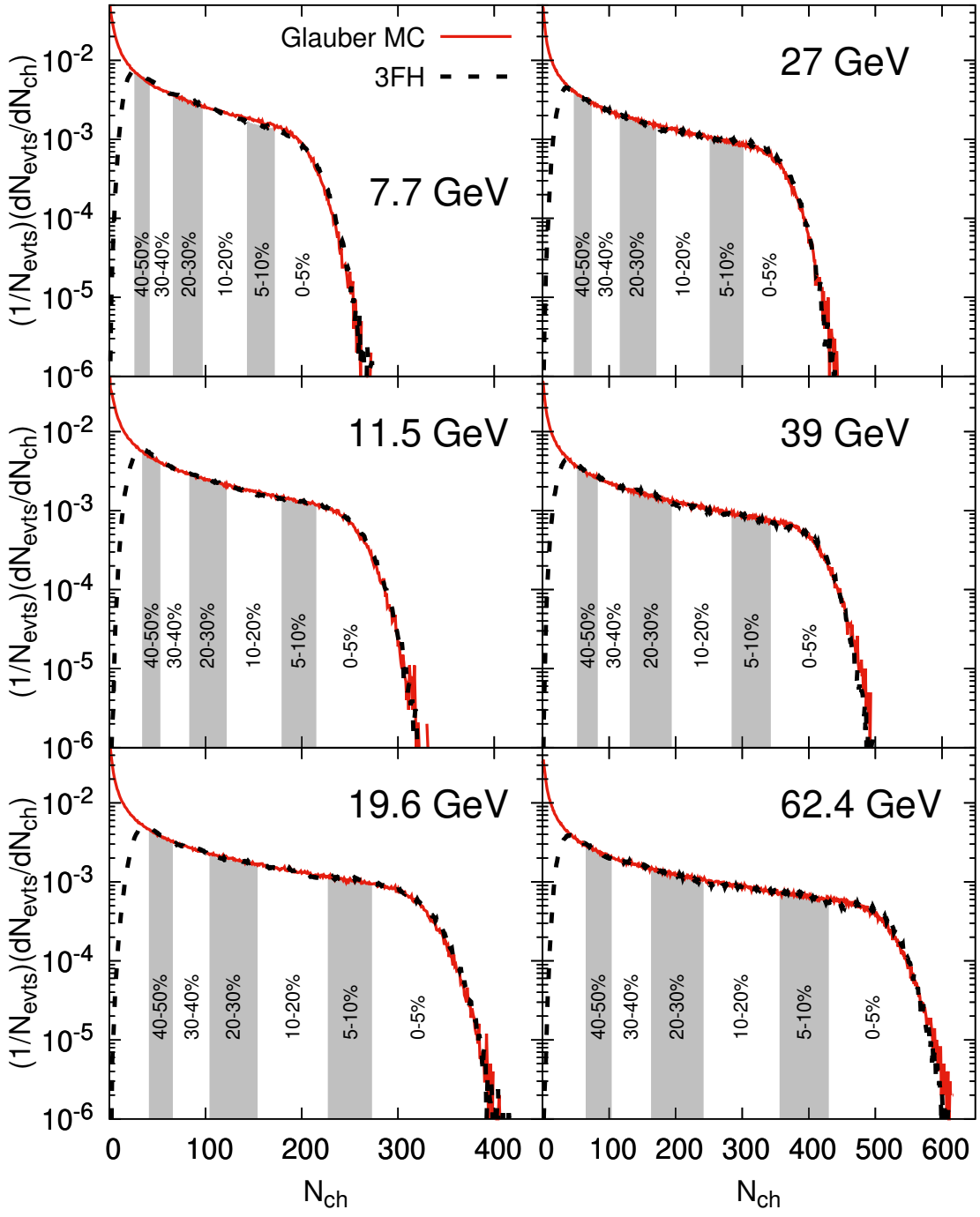

Figure 7.1: Multiplicity distributions for BES energies $\sqrt{s_{\mathrm{NN}}} = 7.7$, 11.5, 19.6, 27, 39, and 62.4 GeV obtained from the 3-fluid hydrodynamic model (black curves) compared with GMC model (red curves). This comparison is used to determine centrality classes in our model, and they are illustrated with grey and white areas.

	Centrality	$\mathrm{d}N_{\mathrm{ch}}/\mathrm{d}\eta$	b [fm]	$\langle N_{\mathrm{part}} \rangle$	$\langle N_{\mathrm{coll}} \rangle$
Au+Au 7.7 GeV	$0-5\%$	≥ 172	$0.00-3.17$	336.7	774.7
	$5-10\%$	$142-171$	$3.17-4.54$	287.8	626.6
	$10-20\%$	$97-141$	$4.54-6.46$	223.9	450.1
	$20-30\%$	$65-96$	$6.46-7.93$	157.9	283.1
	$30-40\%$	$42-64$	$7.93-9.16$	108.6	171.5
	$40-50\%$	$25-41$	$9.16-10.31$	70.6	96.5
Au+Au 11.5 GeV	$0-5\%$	≥ 214	$0.00-3.20$	338.2	793.6
	$5-10\%$	$177-213$	$3.20-4.56$	288.3	638.6
	$10-20\%$	$121-176$	$4.56-6.47$	224.6	458.9
	$20-30\%$	$81-120$	$6.47-7.94$	158.4	288.0
	$30-40\%$	$52-80$	$7.94-9.19$	108.7	173.6
	$40-50\%$	$32-51$	$9.19-10.26$	71.5	99.0
Au+Au 19.6 GeV	$0-5\%$	≥ 273	$0.00-3.20$	340.3	821.7
	$5-10\%$	$226-272$	$3.20-4.57$	290.1	660.1
	$10-20\%$	$154-225$	$4.57-6.48$	225.9	473.2
	$20-30\%$	$103-153$	$6.48-7.95$	159.2	296.0
	$30-40\%$	$66-102$	$7.95-9.20$	109.1	177.6
	$40-50\%$	$40-65$	$9.20-10.32$	71.3	100.0
Au+Au 27 GeV	$0-5\%$	≥ 301	$0.00-3.21$	341.3	842.2
	$5-10\%$	$249-300$	$3.21-4.59$	290.7	674.3
	$10-20\%$	$170-248$	$4.59-6.49$	226.7	483.9
	$20-30\%$	$114-169$	$6.49-7.95$	160.5	303.6
	$30-40\%$	$73-113$	$7.95-9.20$	110.0	182.0
	$40-50\%$	$45-72$	$9.20-10.28$	72.4	103.2
Au+Au 39 GeV	$0-5\%$	≥ 343	$0.00-3.22$	342.8	870.6
	$5-10\%$	$283-342$	$3.22-4.62$	291.4	694.5
	$10-20\%$	$194-282$	$4.62-6.49$	227.7	498.0
	$20-30\%$	$130-193$	$6.49-7.96$	161.3	312.4
	$30-40\%$	$83-129$	$7.96-9.22$	110.7	187.1
	$40-50\%$	$51-82$	$9.22-10.30$	72.9	105.7
Au+Au 62.4 GeV	$0-5\%$	≥ 429	$0.00-3.23$	344.9	915.1
	$5-10\%$	$354-428$	$3.23-4.63$	293.7	728.5
	$10-20\%$	$241-353$	$4.63-6.53$	229.1	520.4
	$20-30\%$	$161-240$	$6.53-8.00$	162.0	323.9
	$30-40\%$	$103-160$	$8.00-9.25$	111.4	193.8
	$40-50\%$	$63-102$	$9.25-10.34$	73.3	108.6

Table 7.2: Borders of multiplicities N_{ch} within $|\eta| < 0.5$ used for centrality determination, and impact parameter range, $\langle N_{\mathrm{part}} \rangle$, and $\langle N_{\mathrm{coll}} \rangle$ extracted from GMC model for BES energies and centralities $0-50\%$.

tion of the multiplicity at $\sqrt{s_{\mathrm{NN}}} = 19.6\,\mathrm{GeV}$. At $\sqrt{s_{\mathrm{NN}}} = 62.4\,\mathrm{GeV}$, the experimental data do not have such a strong two-peak structure as in the 3FH model, but the midrapidity values fit perfectly with the data.

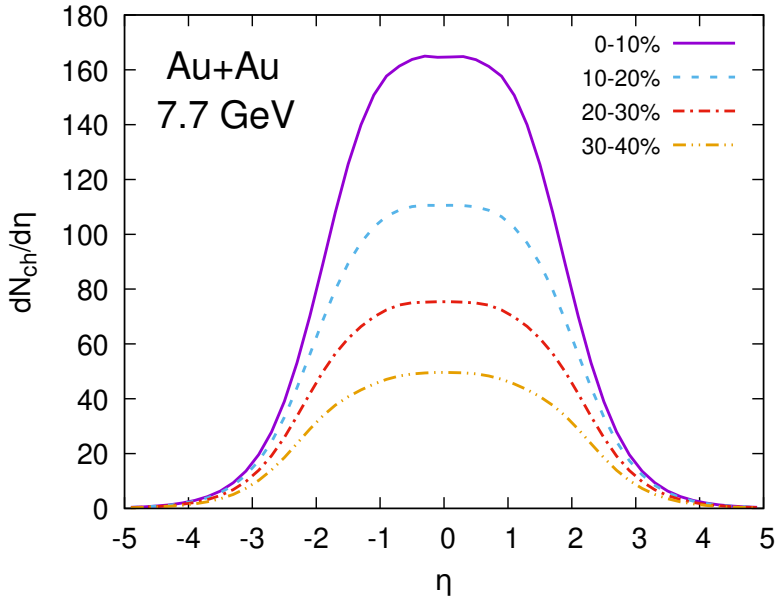

Figure 7.2: Pseudorapidity distributions of charged hadrons in Au+Au collisions at $\sqrt{s_{\mathrm{NN}}} = 7.7\,\mathrm{GeV}$ for various centralities obtained from 3-fluid hydrodynamic model.

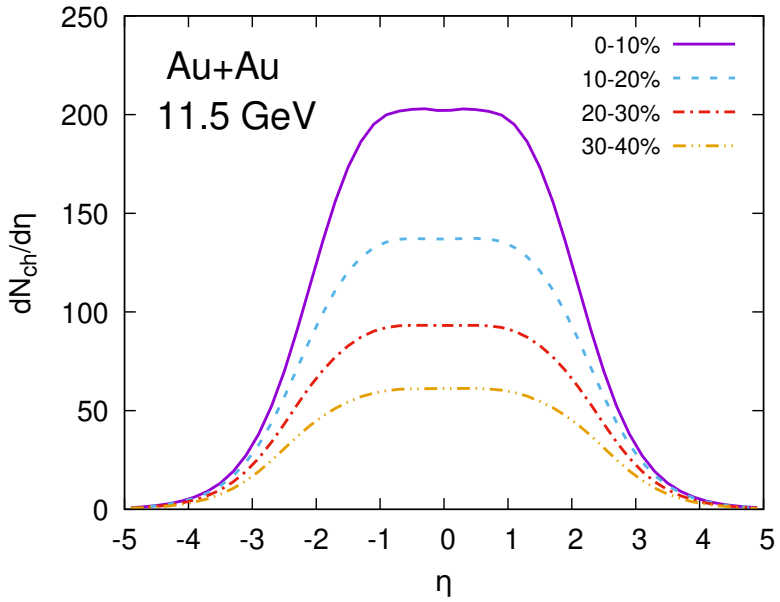

Figure 7.3: Same as Fig. 7.2, but for $\sqrt{s_{\mathrm{NN}}} = 11.5\,\mathrm{GeV}$ Au+Au collisions.

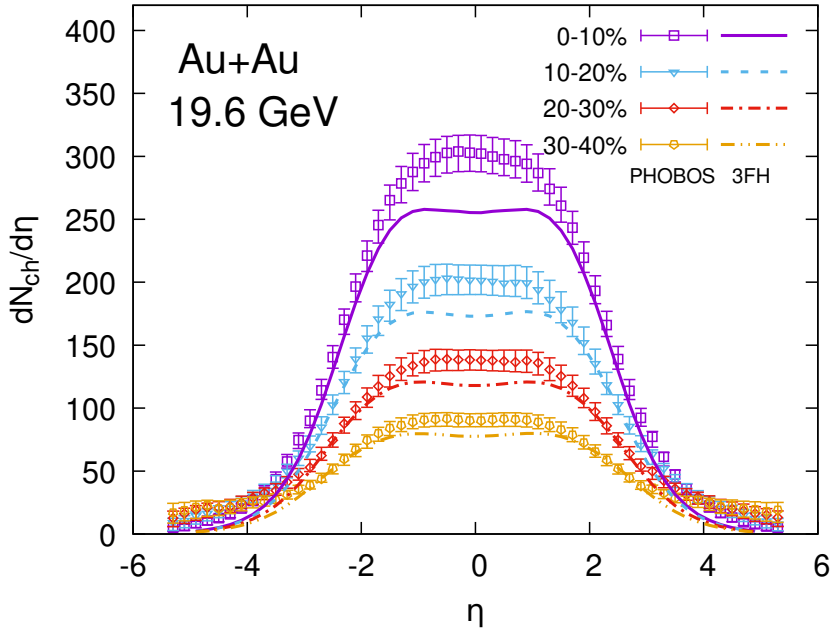

Figure 7.4: Same as Fig. 7.2, but for $\sqrt{s_{\mathrm{NN}}} = 19.6$ GeV Au+Au collisions. At this energy, the results of the 3FH model are compared to the experimental data from PHOBOS collaboration [57].

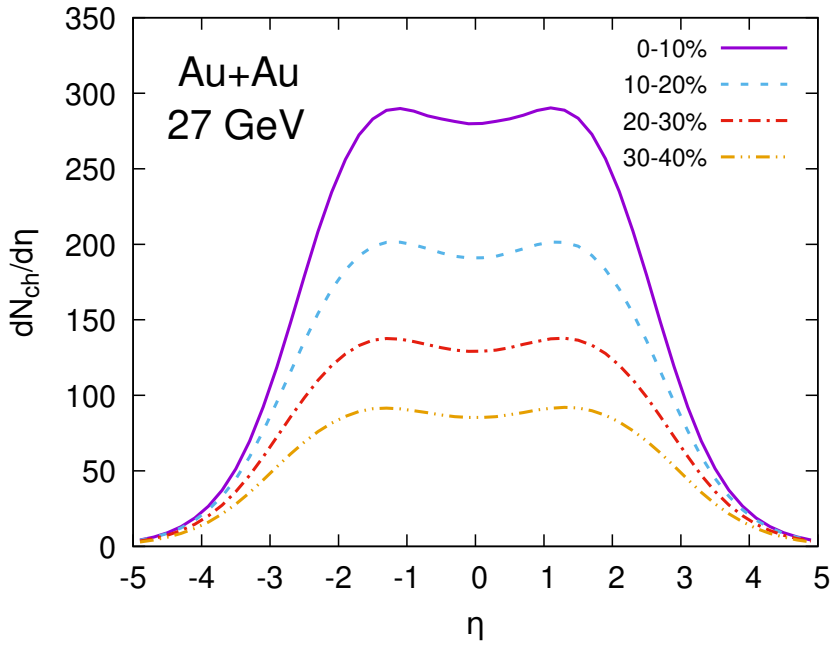

Figure 7.5: Same as Fig. 7.2, but for $\sqrt{s_{\mathrm{NN}}} = 27$ GeV Au+Au collisions.

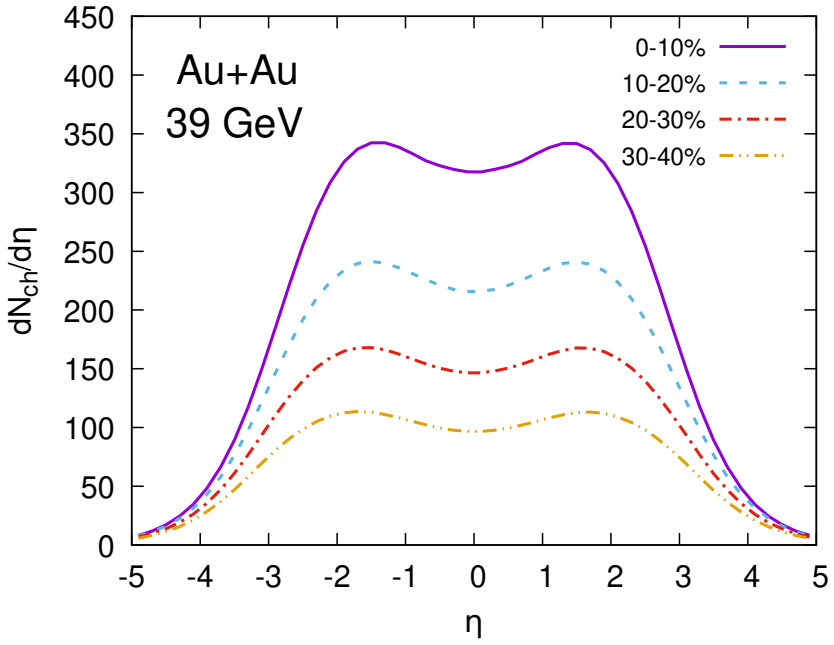

Figure 7.6: Same as Fig. 7.2, but for $\sqrt{s_{\mathrm{NN}}} = 39$ GeV Au+Au collisions.

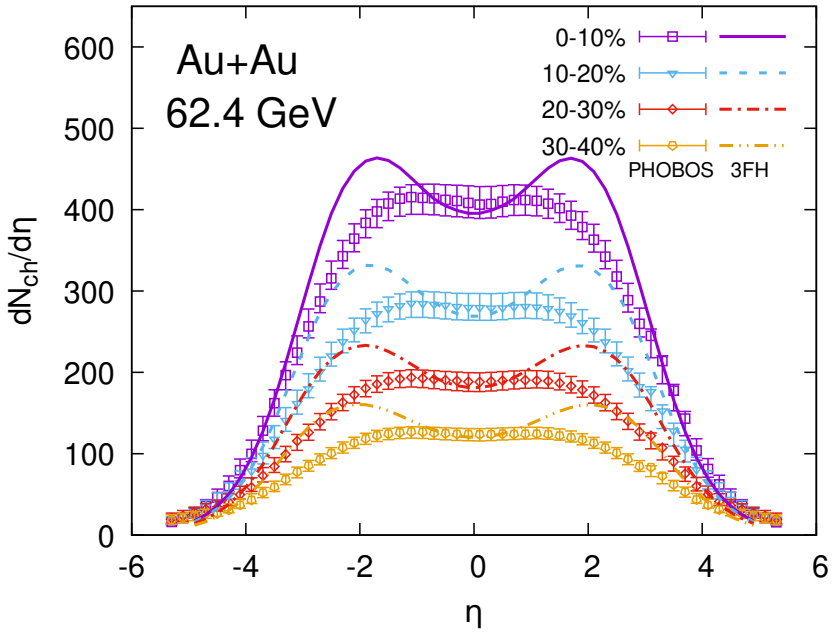

Figure 7.7: Same as Fig. 7.2, but for $\sqrt{s_{\mathrm{NN}}} = 62.4$ GeV Au+Au collisions. At this energy, the results of the 3FH model are compared to the experimental data from PHOBOS collaboration [57].

Figures 7.8 and 7.9 show a rapidity distribution of net protons compared to the experimental data from NA49 and BRAHMS. At $\sqrt{s_{\mathrm{NN}}} = 19.6\,\mathrm{GeV}$ there are no experimental data; therefore, we compared the results from the 3FH model with the experimental data from Pb+Pb collisions at $\sqrt{s_{\mathrm{NN}}} = 17.2\,\mathrm{GeV}$. The 3FH model slightly underestimates the experimental data, which is partially caused by the lower baryon number in the nuclei (197 in Au, 208 in Pb). At $\sqrt{s_{\mathrm{NN}}} = 62.4\,\mathrm{GeV}$ we compare the results from the 3FH model with the experimental data from the same collision setup. Although there are only four experimental data points, the 3FH describes the shape of the rapidity distribution quite well. The correspondence of the rapidity distributions of net protons means that the baryon stopping works well in the 3FH model.

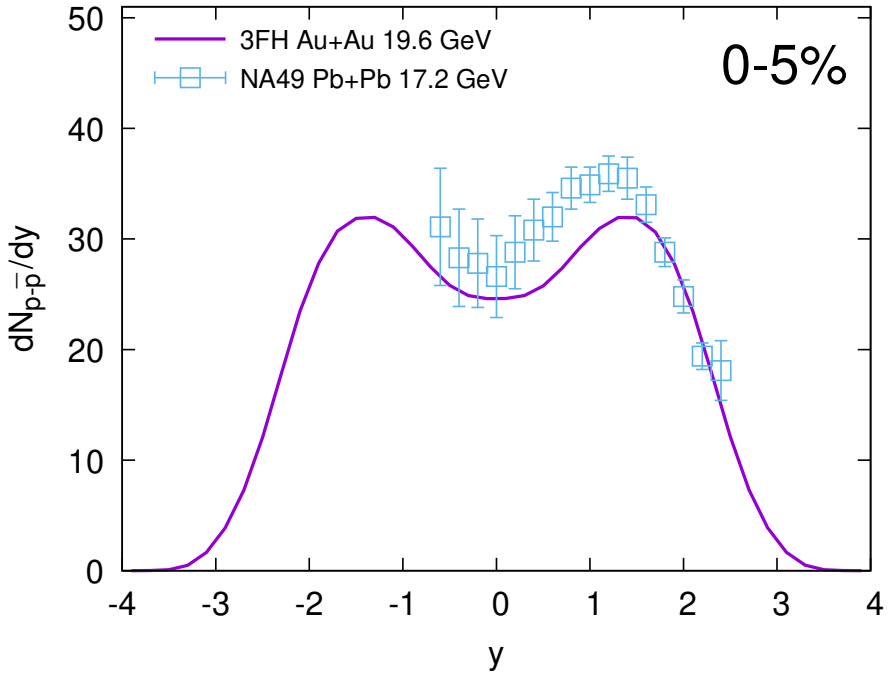

Figure 7.8: Rapidity distribution of net protons in $0-5\%$ central Au+Au collisions at $\sqrt{s_{\mathrm{NN}}} = 19.6\,\mathrm{GeV}$ obtained from 3-fluid hydrodynamic model. Since there are no experimental data at $\sqrt{s_{\mathrm{NN}}} = 19.6\,\mathrm{GeV}$, we compared our results to experimental data of Pb+Pb collisions at $\sqrt{s_{\mathrm{NN}}} = 17.2\,\mathrm{GeV}$. The experimental data points are from NA49 collaboration [126].

The comparison of pseudorapidity distributions with experimental data at both energy indicates that the friction could be slightly stronger, which would bring more energy to midrapidity, increasing the distribution and removing the two-peak structure. However, that would also result in stronger transverse expansion. Moreover, a stronger friction would brake the projectile and target nuclei more, and since only these fluids contain non-zero baryon number, it would

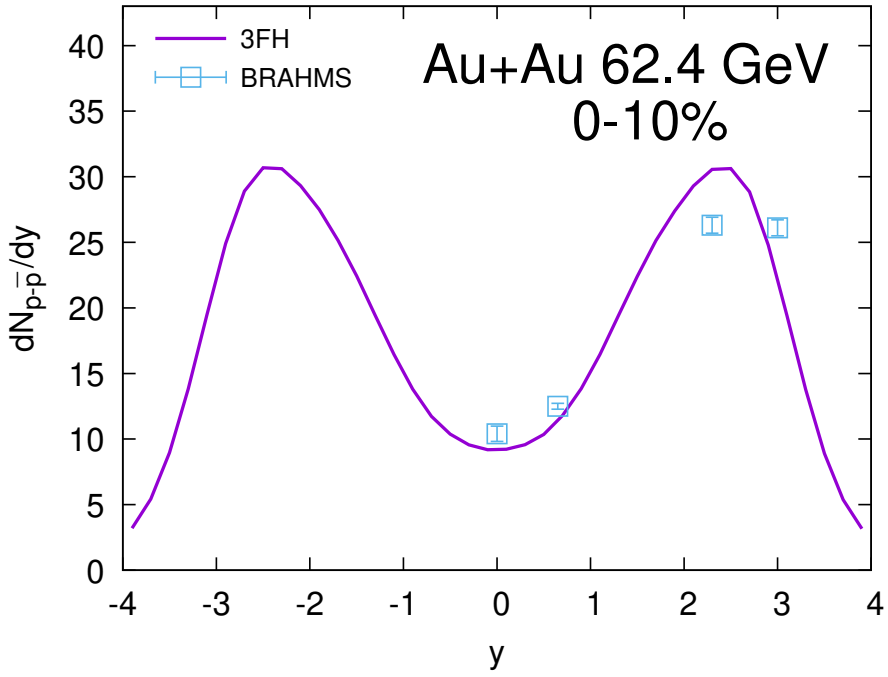

Figure 7.9: Same as Fig. 7.8, but for $0-10$% central Au+Au collisions at $\sqrt{s_{\mathrm{NN}}} = 62.4$ GeV. The experimental data points are from BRAHMS collaboration [127].

bring the two peaks in rapidity distributions of net-protons closer together, resulting in much worse baryon stopping in the model.

7.4 Transverse Momentum Spectra

Next, we show the transverse momentum spectra of π^+, K^+, protons, and antiprotons for all studied energies (Figs. 7.10-7.15). To calculate the p_T-spectra, we used the rapidity cut $|\mathrm{y}| < 0.1$, included weak decay products for proton and antiproton spectra and excluded them for pion spectra. These are the same settings that were used for the analysis of the experimental data. Although not all calculated spectra reproduce the experimental data perfectly, at least the slope of the spectra is generally quite well reproduced. This means that the 3FH model yields correct strength of the transverse expansion.

At $\sqrt{s_{\mathrm{NN}}} = 7.7$ GeV (Fig. 7.10), the pion and kaon spectra agree with the data. The proton spectra are slightly underestimated, mainly in non-central collisions, while antiprotons are quite overestimated. Since the fireball fluid produces protons and antiprotons in pairs due to its zero baryon density, while projectile and target fluids produce more protons than antiprotons, this disagreement with the experimental data suggests that there should be more energy transferred from nuclei fluids to fireball fluid. This would require stronger friction, but as

was mentioned earlier, that would result in stronger transverse expansion and baryon stopping. At $\sqrt{s_{\mathrm{NN}}} = 11.5\,\mathrm{GeV}$ (Fig. 7.11), the results are very similar except for the antiproton spectra, which are closer to the experimental data at this energy. At $\sqrt{s_{\mathrm{NN}}} = 19.6\,\mathrm{GeV}$ (Fig. 7.12), the pion spectra at high p_T start to be underestimated. This may be due to hard processes (e.g., minijets) that have an impact on spectra at high p_T. Proton spectra at this energy are closer to the experimental data, especially in central collisions, where the simulations are within errorbars of the data from STAR. Antiproton spectra are well reproduced for $p_T > 1\,\mathrm{GeV}$. At $\sqrt{s_{\mathrm{NN}}} = 27\,\mathrm{GeV}$ (Fig. 7.13), the pion spectra at high p_T are even more underestimated. The antiproton spectra are even closer to the data, and for mid-central collisions they agree perfectly with the experiment. The results at $\sqrt{s_{\mathrm{NN}}} = 39\,\mathrm{GeV}$ (Fig. 7.14) confirm the tendencies from the lower energies. At $\sqrt{s_{\mathrm{NN}}} = 62.4\,\mathrm{GeV}$ (Fig. 7.15), the published experimental data are only for low p_T. Nevertheless, they correspond to the results of the 3FH model for pions and kaons. Both proton and antiproton spectra are underestimated at this energy.

7.5 Elliptic Flow

In this section, we present the elliptic flow calculated using the cumulant method. Following the STAR paper [73], we use the pseudorapidity cut $|\eta| < 1$. Figure 7.16 shows the elliptic flow as a function of transverse momentum for $20 - 30\%$ mid-central collisions at all studied energies. At low energies, the 3FH model overestimates the experimental data from the experiment STAR quite a lot. However, the results of simulations are closer to the experimental data at higher collision energies. Unfortunately, there are no published data for $\sqrt{s_{\mathrm{NN}}} = 62.4\,\mathrm{GeV}$, but already at $\sqrt{s_{\mathrm{NN}}} = 39\,\mathrm{GeV}$, the elliptic flow agrees with experimental data for $p_T < 1.5\,\mathrm{GeV}$. At higher p_T, it again starts to overestimate the flow.

When looking at the centrality-dependent elliptic flow integrated over $0.2 < p_T < 2.0\,\mathrm{GeV}$ (Fig. 7.17), one may notice a similar hierarchy that can be seen in p_T-dependent elliptic flow, that the flow obtained from the 3FH model is closer to the experimental data with increasing energy. Another observation is that the data are best reproduced for the most central collisions, while with increasing centrality the 3FH model starts to produce an overestimated elliptic flow (especially at low $\sqrt{s_{\mathrm{NN}}}$).

Ivanov was able to reproduce the elliptic flow with the original 3-fluid hydrodynamic model [157]. However, he uses underestimated values of the impact parameter with respect to the centrality classes to which the simulations are compared. This leads to a lower elliptic flow, which means that his model actu-

ally also overestimates v_2.

The overestimated elliptic flow gives space for the shear viscosity, which decreases the flow. Moreover, studies such as [7] suggest that the effective ratio of shear viscosity to entropy density grows towards lower collision energies, which means that the flow will be suppressed more strongly at lower energies. This also corresponds to the results of the ideal 3FH model. We plan to add viscosity to the model as the next step of the project.

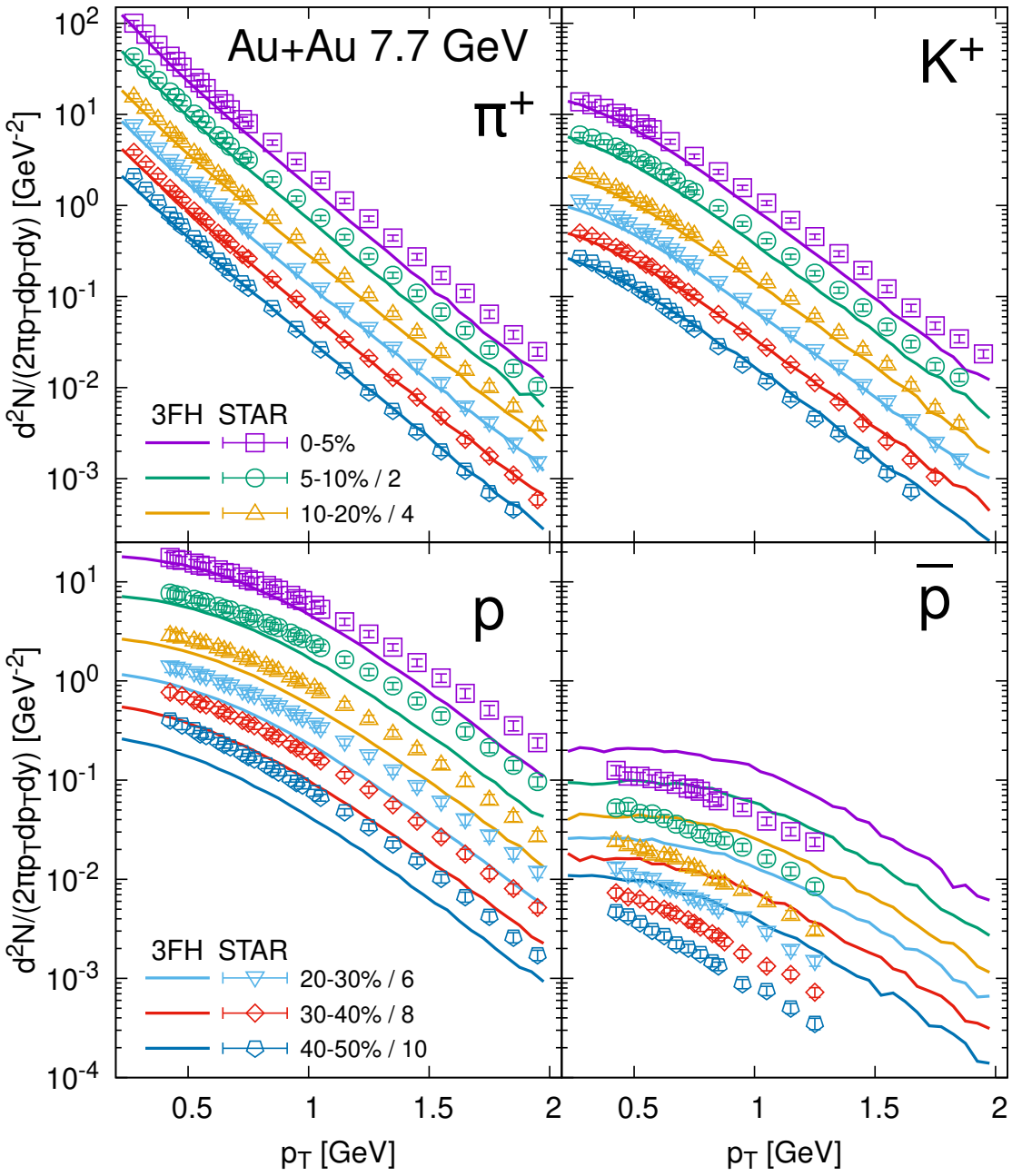

Figure 7.10: Transverse momentum spectra of positively charged pions (upper left), kaons (upper right), protons (lower left) and antiprotons (lower right) in Au+Au collisions at $\sqrt{s_{\mathrm{NN}}} = 7.7$ GeV for various centralities obtained from 3-fluid hydrodynamic model. The experimental data points are from STAR collaboration [58].

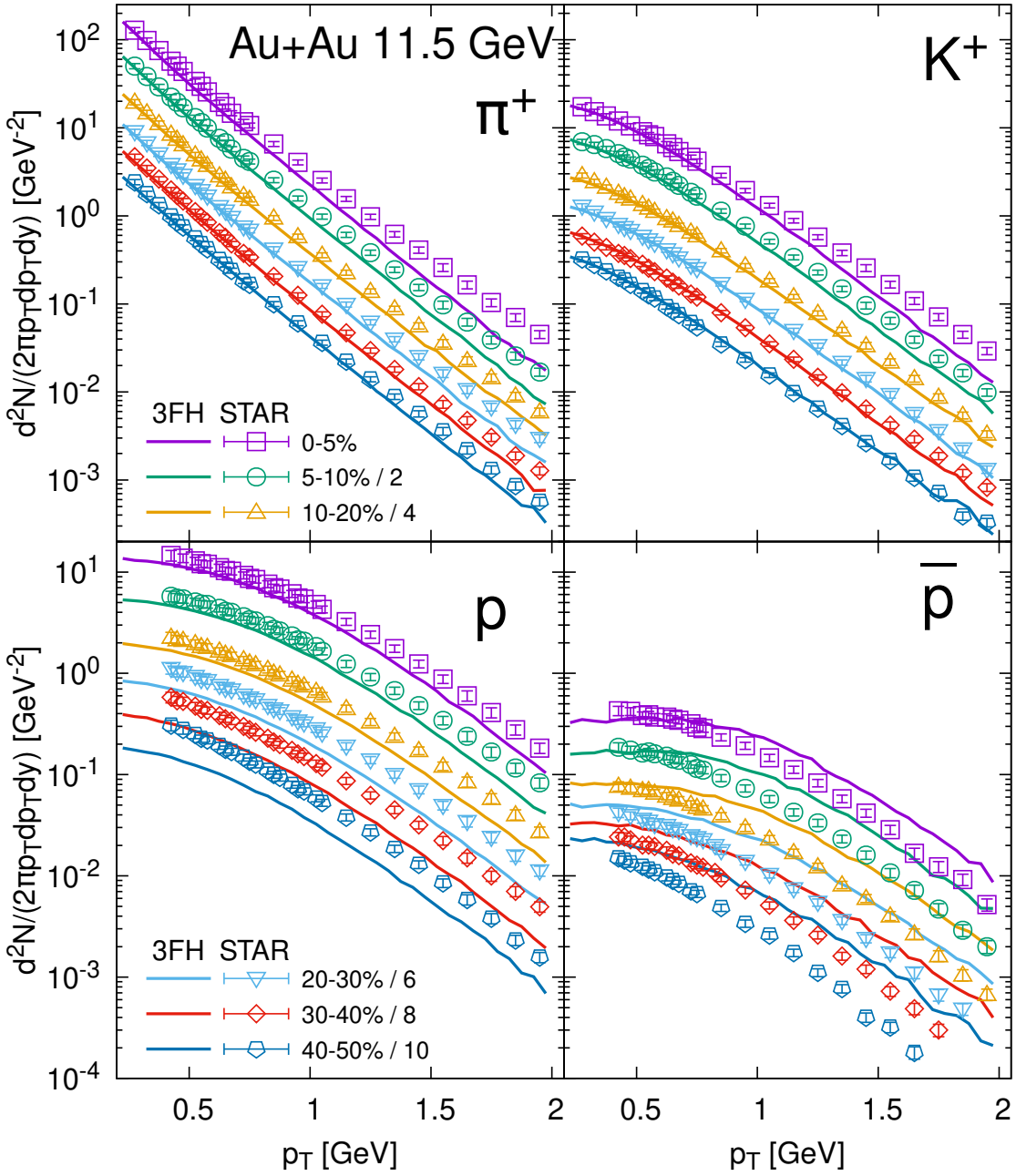

Figure 7.11: Same as Fig. 7.10, but for $\sqrt{s_{\mathrm{NN}}} = 11.5$ GeV Au+Au collisions. The experimental data points are from STAR collaboration [58].

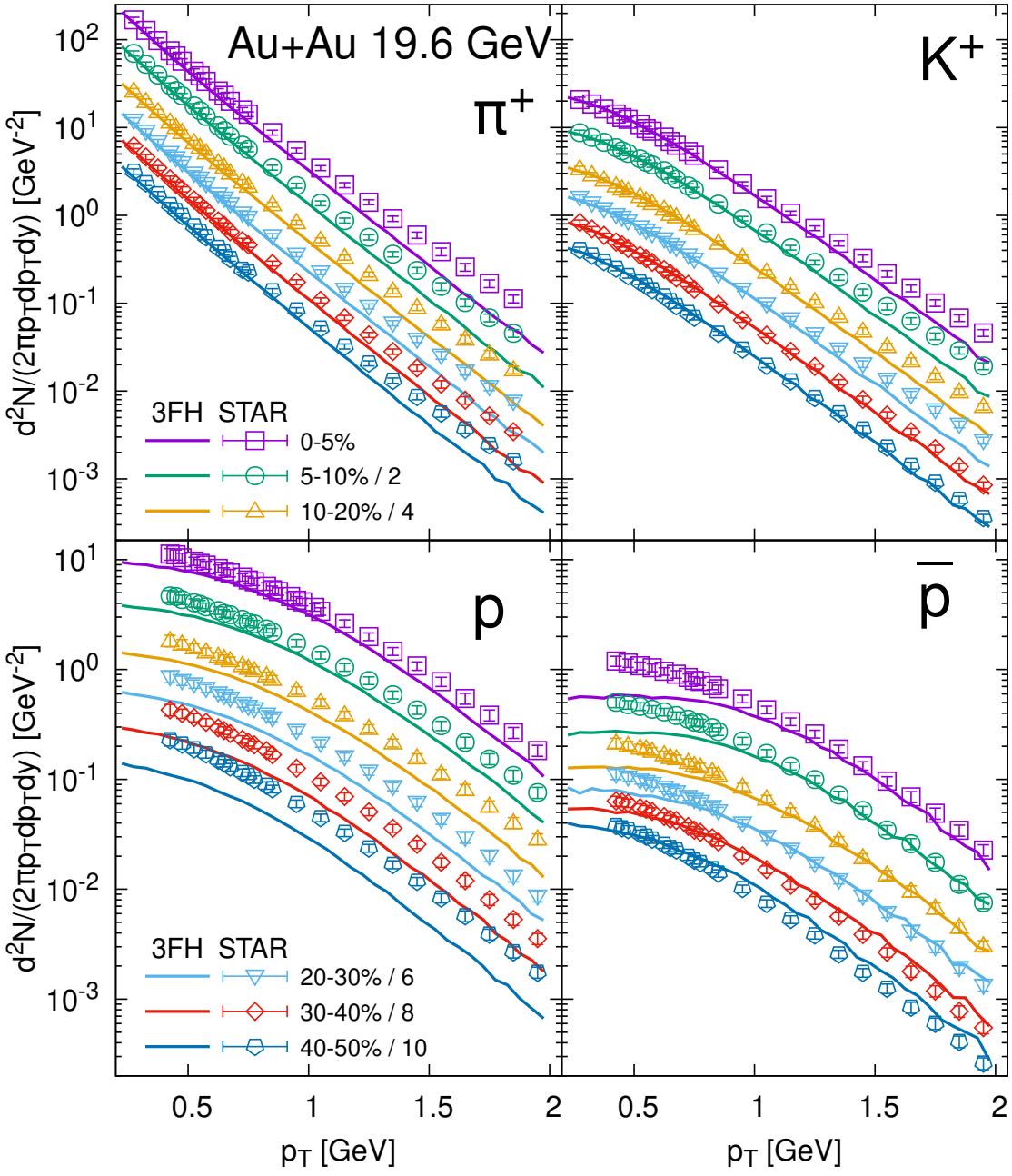

Figure 7.12: Same as Fig. 7.10, but for $\sqrt{s_{\rm NN}} = 19.6$ GeV Au+Au collisions. The experimental data points are from STAR collaboration [58].

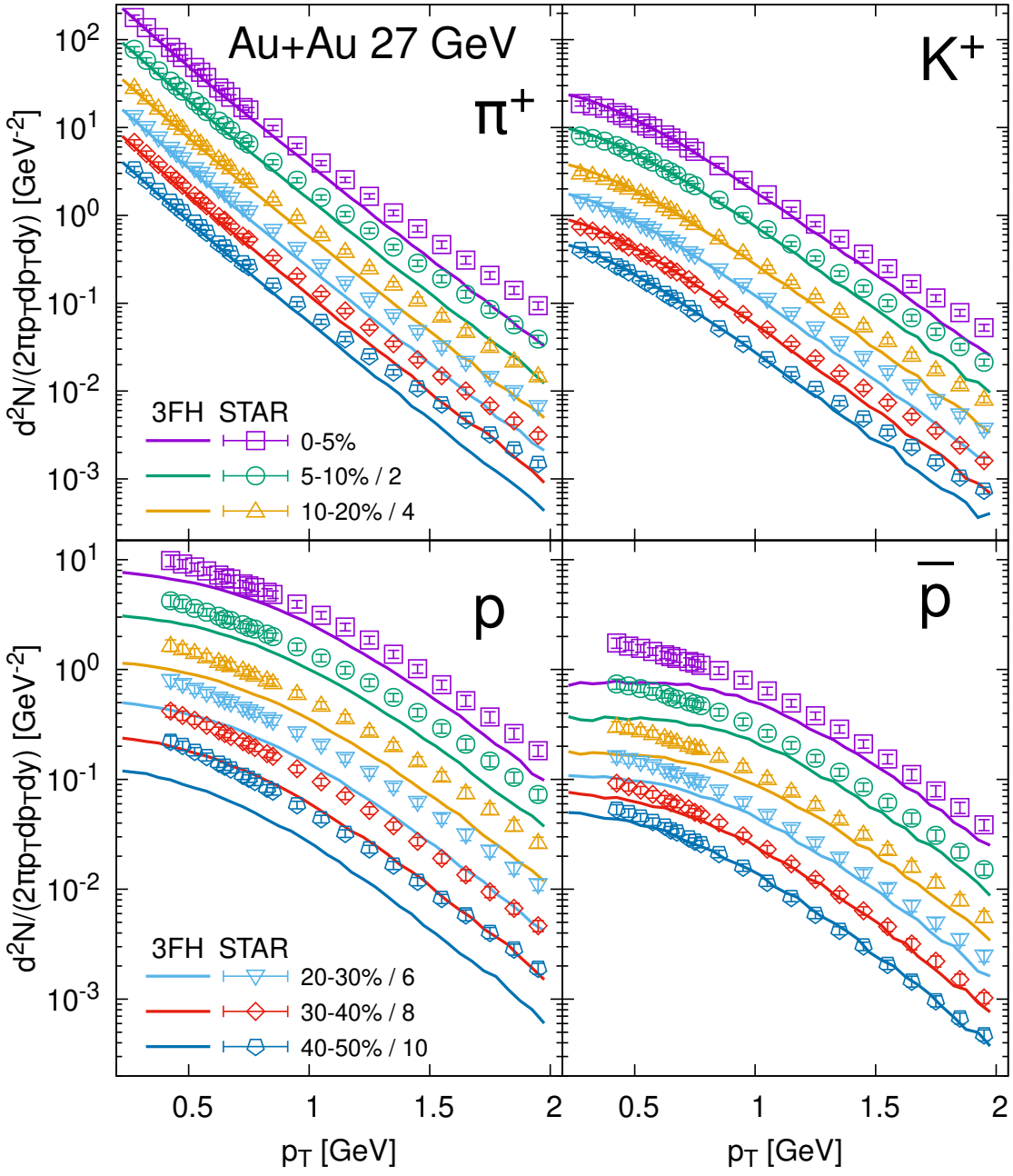

Figure 7.13: Same as Fig. 7.10, but for $\sqrt{s_{\mathrm{NN}}} = 27$ GeV Au+Au collisions. The experimental data points are from STAR collaboration [58].

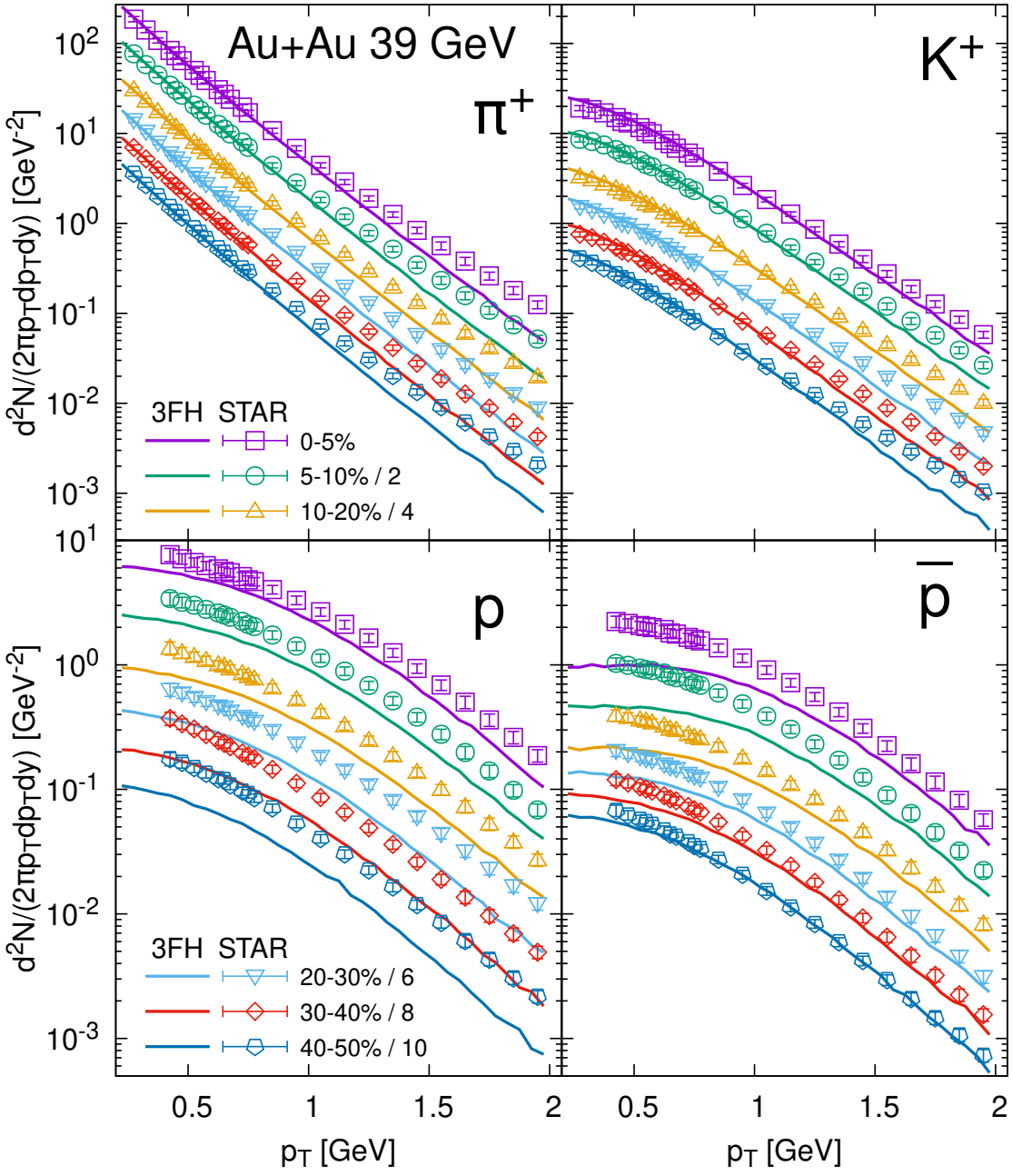

Figure 7.14: Same as Fig. 7.10, but for $\sqrt{s_{\mathrm{NN}}} = 39$ GeV Au+Au collisions. The experimental data points are from STAR collaboration [58].

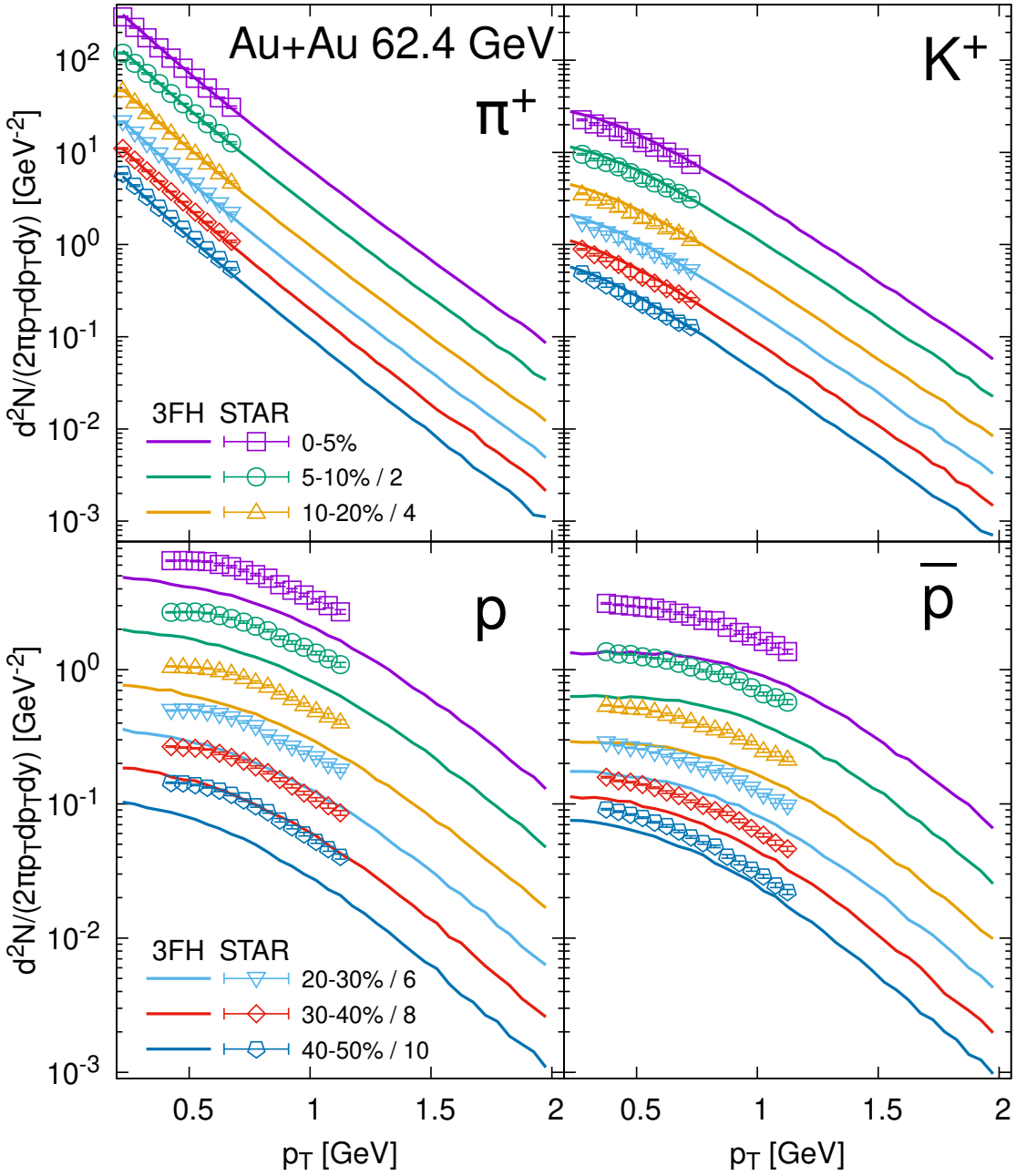

Figure 7.15: Same as Fig. 7.10, but for $\sqrt{s_{\mathrm{NN}}} = 62.4$ GeV Au+Au collisions. The experimental data points are from STAR collaboration [59].

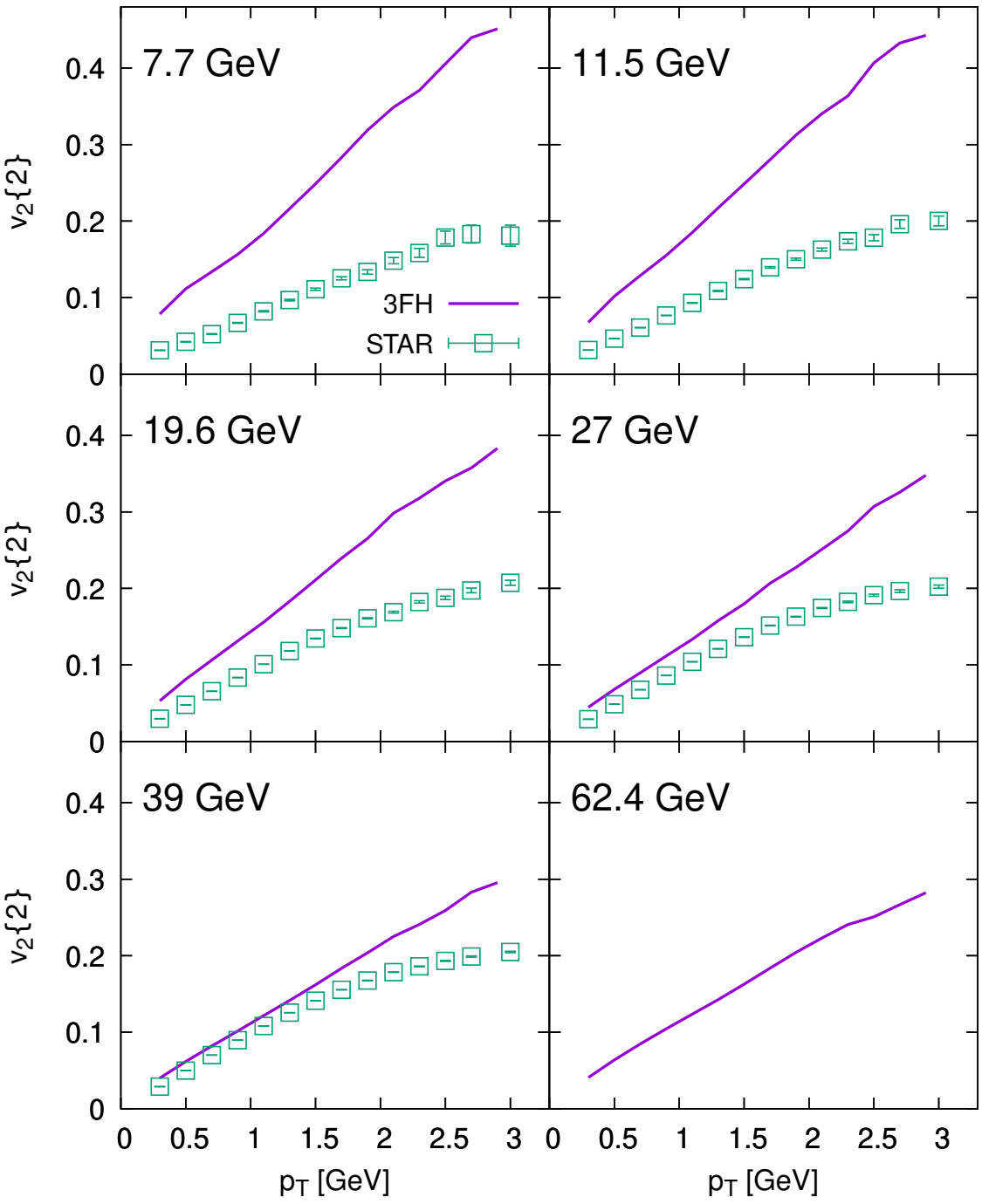

Figure 7.16: Elliptic flow as a function of transverse momentum p_T in $20-30$% central Au+Au collisions at energies $\sqrt{s_{\mathrm{NN}}} = 7.7 - 62.4$ GeV obtained from 3-fluid hydrodynamic model. The experimental data points are from STAR collaboration [73].

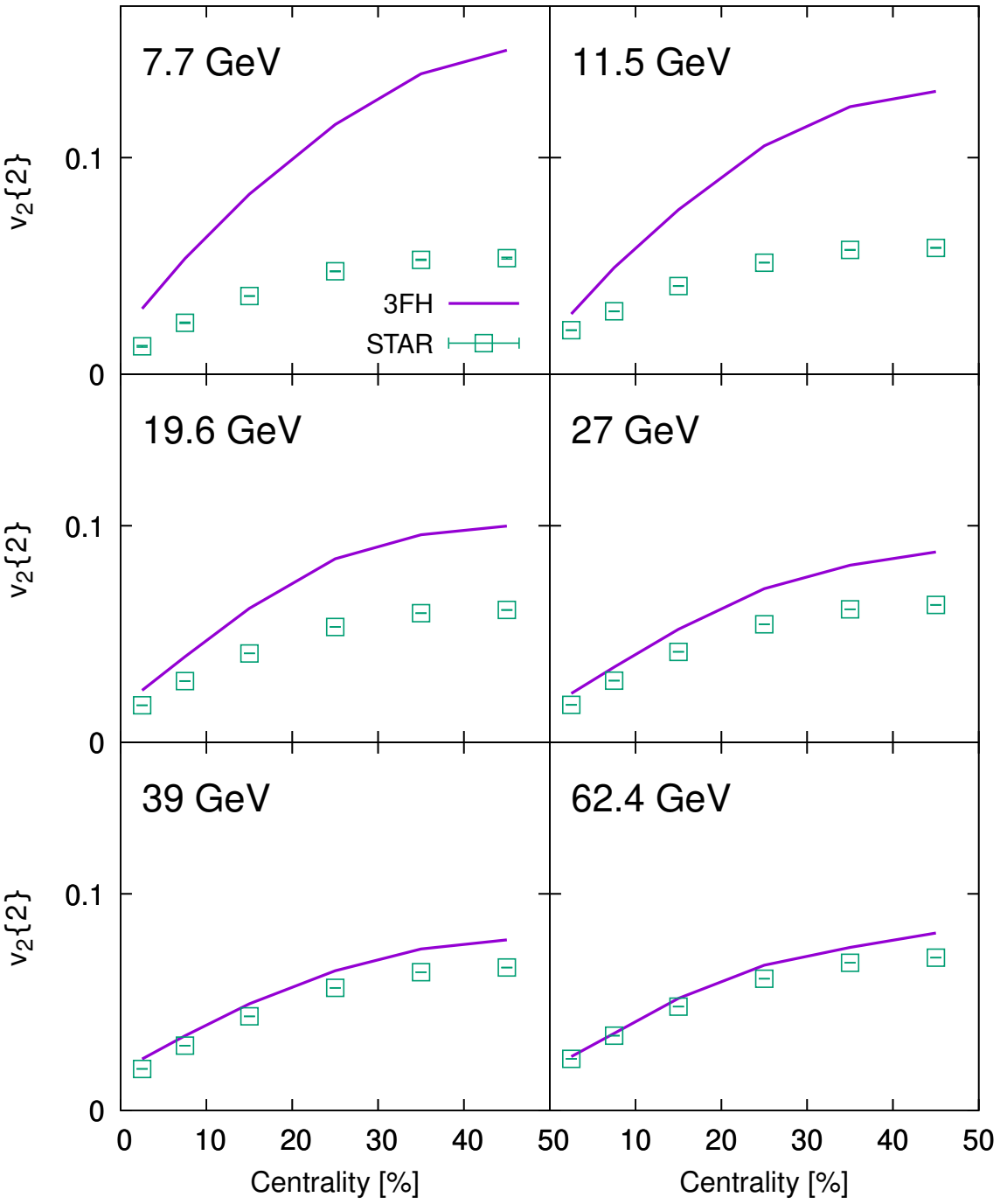

Figure 7.17: Elliptic flow as a function of centrality in Au+Au collisions at energies $\sqrt{s_{\mathrm{NN}}} = 7.7 - 62.4$ GeV obtained from 3-fluid hydrodynamic model. The experimental data points are from STAR collaboration [73, 129].

Chapter 8

Conclusions

This work presents a study of hydrodynamic simulations of heavy-ion collisions at energies from a few to tens of GeV. Such simulations have to deal with complex initial-state geometry, caused by weak relativistic contraction of nuclei, or finite baryon number. However, simulations at these energies are interesting from the point of view of physics, as they operate in the region around the critical point of the QCD.

For this study, we chose two approaches. In the first part of the work, we used the existing hydrodynamic model vHLLE together with the initial-state models UrQMD, GLISSANDO, and T_RENTo, and the UrQMD cascade for final-state interactions. We extended the initial-state models GLISSANDO and T_RENTo to have a three-dimensional structure using a Gaussian ansatz. These simulations produced a quite good description of the experimental data for rapidity distributions, transverse momentum spectra, and elliptic flow. Surprisingly, the best correspondence with the data was obtained with the T_RENTo initial state, which was originally developed for much higher energies. Among other observables, we also studied the longitudinal decorrelation of the elliptic flow. We found that the decorrelation originates in the initial-state eccentricity and is transformed into the final-state momentum decorrelation as a result of hydrodynamic evolution. However, the longitudinal structure of the initial state required tuning of several parameters, which depend on collision energy and even on centrality.

In the second part of this work, we constructed a novel hybrid model designed for these energies. The model is based on the 3-fluid hydrodynamic model created by Ivanov. The core of the model is the hydrodynamic algorithm from vHLLE. Unlike Ivanov's model, our 3FH model has fluctuating initial conditions that sample nucleons according to the Woods-Saxon formula. Necessitated by the event-by-event initial conditions, the model includes particles-to-fluid transition via the smoothing kernel, and also includes particlization via

the Cooper-Frye formula, and transport model for final-state rescatterings. The model has a space for fine tuning in friction terms that control the amount of energy transformed from the nuclei fluids to the fireball fluid. We chose to set the tuning parameters to be independent of the collision energy, and we were able to find a set of parameters that were able to reproduce the rapidity distribution and transverse momentum spectra along the studied energies ($\sqrt{s_{\mathrm{NN}}} = 7.7 - 62.4\,\mathrm{GeV}$). Therefore, our model can accurately make predictions for NICA and FAIR.

Despite the basic 1-fluid code having shear and bulk viscosities included, a consistent inclusion of viscous corrections in the multi-fluid evolution is left for a future study. Therefore, we keep the viscous corrections switched off in the present version of the 3-fluid model. Because of that, our model overestimates the elliptic flow, and the overestimation grows with decreasing collision energy. We plan to add viscous corrections as the next step of the project in the near future.

Acknowledgements

I would like to express my gratitude and appreciation to my supervisor Prof. Dr. Boris Tomášik for his guidance, mentoring, support, and motivation during the almost eight years of our collaboration. Without him, this work would never have been created. Second, I would like to thank my supervisor specialist Iurii Karpenko, Ph.D., who always gladly helped me solve any problem that occurred during our study. I also thank Barbara Trzeciak, Ph.D., and Prof. Pasi Huovinen for consultations leading to the successful completion of this dissertation.

I also would like to thank my colleagues and friends Radka Vozábová, Lukáš Holub, and Martin Adamec, who accompanied me throughout the university. We formed a strong bond and created wonderful memories.

Finally, I would like to thank my family for supporting me throughout the Ph.D. study. To my loving wife Lucka, who is always my support, especially in difficult times. To my son Lukáš, who made writing this thesis much more complicated, but nevertheless brings me a lot of joy. And to my mom, who raised me to be the person I am today.

This work was supported by the project Centre of Advanced Applied Sciences, No. CZ.02.1.01/0.0/0.0/16-019/0000778, co-financed by the European Union, and by the grant GA22-25026S of the Czech Science Foundation (GAČR). Computational resources were supplied by the project "e-Infrastruktura CZ" (e-INFRA CZ LM2018140) supported by the Ministry of Education, Youth and Sports of the Czech Republic.

List of Publications

1. Tomášik, B., Melo, I. & Cimerman, J. Generation of random deviates for relativistic quantum-statistical distributions. *Communications - Scientific Letters of the University of Zilina* **19,** 66–70. arXiv: 1602.08233 [physics.comp-ph] (2017).
2. Cimerman, J., Tomášik, B., Csanád, M. & Lökös, S. Higher-order anisotropies in the Blast-Wave Model - disentangling flow and density field anisotropies. *Eur. Phys. J. A* **53,** 161. arXiv: 1702.01735 [nucl-th] (2017).
3. Tomášik, B. & Cimerman, J. Event by event fluctuations of the source shape: implications for the Levy shape, and Event Shape Sorting. *Acta Phys. Pol. B Proc. Suppl.* **12,** 229. arXiv: 1810.01157 [nucl-th] (2019).
4. Tomášik, B., Cimerman, J., Kopečná, R. & Schulc, M. Fluctuating shapes of the fireballs in heavy-ion collisions. *EPJ Web Conf.* **204** (eds Bondarenko, S., Burov, V. & Malakhov, A.) 03011. arXiv: 1811.10349 [nucl-th] (2019).
5. Cimerman, J. & Tomášik, B. Event Shape Sorting: prospects and femtoscopy applications. *PoS* **CORFU2018** (eds Anagnostopoulos, K. *et al.*) 194. arXiv: 1902.08973 [nucl-th] (2019).
6. Tomášik, B., Cimerman, J. & Plumberg, C. Averaging and the Shape of the Correlation Function. *Universe* **5,** 148 (2019).
7. Cimerman, J., Tomášik, B. & Plumberg, C. The Shape of the Correlation Function. *Phys. Part. Nucl.* **51,** 3. arXiv: 1909.00278 [nucl-th] (2020).
8. Cimerman, J., Plumberg, C. & Tomášik, B. The Shape of the Correlation Function. arXiv: 1909.07998 [nucl-th].
9. Tomášik, B. & Cimerman, J. Prospects of Event Shape Sorting. *Phys. Part. Nucl.* **51,** 232–237. arXiv: 1910.14183 [nucl-th] (2020).
10. Cimerman, J., Plumberg, C. & Tomášik, B. The Shape of the Correlation Function. *PoS* **ICHEP2020,** 538. arXiv: 2012.04412 [nucl-th] (2021).

11. Cimerman, J., Karpenko, I., Tomášik, B. & Trzeciak, B. A. A benchmark of initial state models for heavy-ion collisions at $\sqrt{s_{\mathrm{NN}}} = 27$ and 62 GeV. *Phys. Rev. C* **103,** 034902. arXiv: 2012.10266 [nucl-th] (2021).

12. Cimerman, J., Karpenko, I., Tomášik, B. & Trzeciak, B. A. Anisotropic flow decorrelation in heavy-ion collisions with event-by-event viscous hydrodynamics. *Phys. Rev. C* **104,** 014904. arXiv: 2104.08022 [nucl-th] (2021).

13. Cimerman, J., Karpenko, I., Tomášik, B. & Trzeciak, B. A. Anisotropic flow decorrelation in heavy-ion collisions at RHIC-BES energies with 3D event-by-event viscous hydrodynamics. *PoS* **EPS-HEP2021,** 312. arXiv: 2110.05578 [nucl-th] (2022).

14. Cimerman, J., Karpenko, I., Tomasik, B. & Trzeciak, B. A. Flow decorrelation in heavy-ion collisions at $\sqrt{s_{\mathrm{NN}}}$=27 and 200 GeV with 3D event-by-event viscous hydrodynamics. *SciPost Phys. Proc.* **10,** 031. arXiv: 2110.14783 [nucl-th] (2022).

Bibliography

1. Landau, L. On the multiparticle production in high-energy collisions. *Izv. Akad. Nauk Ser. Fiz.* **17,** 51–64 (1953).
2. Bjorken, J. Highly Relativistic Nucleus-Nucleus Collisions: The Central Rapidity Region. *Phys. Rev. D* **27,** 140–151 (1983).
3. Song, H., Bass, S. A., Heinz, U., Hirano, T. & Shen, C. 200 A GeV Au+Au collisions serve a nearly perfect quark-gluon liquid. *Phys. Rev. Lett.* **106.** [Erratum: Phys.Rev.Lett. 109, 139904 (2012)], 192301. arXiv: 1011.2783 [nucl-th] (2011).
4. Schenke, B., Jeon, S. & Gale, C. (3+1)D hydrodynamic simulation of relativistic heavy-ion collisions. *Phys. Rev. C* **82,** 014903. arXiv: 1004.1408 [hep-ph] (2010).
5. Shen, C. *et al.* The iEBE-VISHNU code package for relativistic heavy-ion collisions. *Comput. Phys. Commun.* **199,** 61–85. arXiv: 1409.8164 [nucl-th] (2016).
6. Pang, L.-G., Petersen, H. & Wang, X.-N. Pseudorapidity distribution and decorrelation of anisotropic flow within the open-computing-language implementation CLVisc hydrodynamics. *Phys. Rev. C* **97,** 064918. arXiv: 1802.04449 [nucl-th] (2018).
7. Karpenko, I., Huovinen, P., Petersen, H. & Bleicher, M. Estimation of the shear viscosity at finite net-baryon density from $A + A$ collision data at $\sqrt{s_{\mathrm{NN}}} = 7.7 - 200$ GeV. *Phys. Rev. C* **91,** 064901. arXiv: 1502.01978 [nucl-th] (2015).
8. Noronha-Hostler, J., Denicol, G. S., Noronha, J., Andrade, R. P. G. & Grassi, F. Bulk Viscosity Effects in Event-by-Event Relativistic Hydrodynamics. *Phys. Rev. C* **88,** 044916. arXiv: 1305.1981 [nucl-th] (2013).
9. Andrade, R., Grassi, F., Hama, Y., Kodama, T. & Socolowski O., J. On the necessity to include event-by-event fluctuations in experimental evaluation of elliptical flow. *Phys. Rev. Lett.* **97,** 202302. arXiv: nucl-th/0608067 (2006).

10. Bozek, P. Flow and interferometry in 3+1 dimensional viscous hydrodynamics. *Phys. Rev. C* **85,** 034901. arXiv: 1110.6742 [nucl-th] (2012).

11. Werner, K., Karpenko, I., Pierog, T., Bleicher, M. & Mikhailov, K. Event-by-Event Simulation of the Three-Dimensional Hydrodynamic Evolution from Flux Tube Initial Conditions in Ultrarelativistic Heavy Ion Collisions. *Phys. Rev. C* **82,** 044904. arXiv: 1004.0805 [nucl-th] (2010).

12. Stephanov, M. & Yin, Y. Hydrodynamics with parametric slowing down and fluctuations near the critical point. *Phys. Rev. D* **98,** 036006. arXiv: 1712.10305 [nucl-th] (2018).

13. Becquerel, H. On the rays emitted by phosphorescence. *Compt. Rend. Hebd. Seances Acad. Sci.* **122,** 420–421 (1896).

14. Thomson, J. J. Cathode rays. *Phil. Mag. Ser. 5* **44,** 293–316 (1897).

15. Thomson, J. J. On the structure of the atom: an investigation of the stability and periods of oscillation of a number of corpuscles arranged at equal intervals around the circumference of a circle; with application of the results to the theory of atomic structure. *Phil. Mag. Ser. 6* **7,** 237–265 (1904).

16. Rutherford, E. The scattering of alpha and beta particles by matter and the structure of the atom. *Phil. Mag. Ser. 6* **21,** 669–688 (1911).

17. Rutherford, E. Collision of α particles with light atoms. IV. An anomalous effect in nitrogen. *Phil. Mag. Ser. 6* **37,** 581–587 (1919).

18. Chadwick, J. Possible Existence of a Neutron. *Nature* **129,** 312 (1932).

19. Gell-Mann, M. The Eightfold Way: A Theory of strong interaction symmetry (1961).

20. Gell-Mann, M. A Schematic Model of Baryons and Mesons. *Phys. Lett.* **8,** 214–215 (1964).

21. Zweig, G. An SU(3) model for strong interaction symmetry and its breaking. Version 1 (Jan. 1964).

22. Zweig, G. in *DEVELOPMENTS IN THE QUARK THEORY OF HADRONS. VOL. 1. 1964 - 1978* 22–101 (Feb. 1964).

23. Bjorken, J. D. & Glashow, S. L. Elementary Particles and SU(4). *Phys. Lett.* **11,** 255–257 (1964).

24. Glashow, S. L., Iliopoulos, J. & Maiani, L. Weak Interactions with Lepton-Hadron Symmetry. *Phys. Rev. D* **2,** 1285–1292 (1970).

25. Kobayashi, M. & Maskawa, T. CP Violation in the Renormalizable Theory of Weak Interaction. *Prog. Theor. Phys.* **49,** 652–657 (1973).

26. Bloom, E. D. *et al.* High-Energy Inelastic e p Scattering at 6-Degrees and 10-Degrees. *Phys. Rev. Lett.* **23,** 930–934 (1969).

27. Breidenbach, M. *et al.* Observed Behavior of Highly Inelastic electron-Proton Scattering. *Phys. Rev. Lett.* **23,** 935–939 (1969).

28. Greenberg, O. W. Spin and Unitary Spin Independence in a Paraquark Model of Baryons and Mesons. *Phys. Rev. Lett.* **13,** 598–602 (1964).

29. Nambu, Y. in Preludes in Theoretical Physics (eds A. de-Shalit, H. F. & van Hove, L.) 133. https://ci.nii.ac.jp/naid/10010433043/en/ (1966).

30. Fritzsch, H., Gell-Mann, M. & Leutwyler, H. Advantages of the Color Octet Gluon Picture. *Phys. Lett. B* **47,** 365–368 (1973).

31. Berger, C. *et al.* Jet Analysis of the Υ (9.46) Decay Into Charged Hadrons. *Phys. Lett. B* **82,** 449–455 (1979).

32. Aad, G. *et al.* Observation of a new particle in the search for the Standard Model Higgs boson with the ATLAS detector at the LHC. *Phys. Lett. B* **716,** 1–29. arXiv: 1207.7214 [hep-ex] (2012).

33. *Standard Model.* Accessed 16 May 2022. https://en.wikipedia.org/wiki/Standard_Model.

34. Collins, J. C. & Perry, M. J. Superdense Matter: Neutrons Or Asymptotically Free Quarks? *Phys. Rev. Lett.* **34,** 1353 (1975).

35. Cabibbo, N. & Parisi, G. Exponential Hadronic Spectrum and Quark Liberation. *Phys. Lett. B* **59,** 67–69 (1975).

36. *New State of Matter created at CERN.* Accessed 25 June 2020. https://home.cern/news/press-release/cern/new-state-matter-created-cern.

37. Weller, R. D. & Romatschke, P. One fluid to rule them all: viscous hydrodynamic description of event-by-event central p+p, p+Pb and Pb+Pb collisions at $\sqrt{s} = 5.02$ TeV. *Phys. Lett. B* **774,** 351–356. arXiv: 1701.07145 [nucl-th] (2017).

38. Zhou, Y., Zhao, W., Murase, K. & Song, H. One fluid might not rule them all. *Nucl. Phys. A* **1005** (eds Liu, F., Wang, E., Wang, X.-N., Xu, N. & Zhang, B.-W.) 121908. arXiv: 2005.02684 [nucl-th] (2021).

39. Adams, J. *et al.* Evidence from d + Au measurements for final state suppression of high p(T) hadrons in Au+Au collisions at RHIC. *Phys. Rev. Lett.* **91,** 072304. arXiv: nucl-ex/0306024 (2003).

40. Zyla, P. *et al.* Review of Particle Physics. *PTEP* **2020.** and 2021 update, 083C01 (2020).

41. Gross, D. J. & Wilczek, F. Ultraviolet Behavior of Nonabelian Gauge Theories. *Phys. Rev. Lett.* **30** (ed Taylor, J. C.) 1343–1346 (1973).

42. Politzer, H. D. Reliable Perturbative Results for Strong Interactions? *Phys. Rev. Lett.* **30** (ed Taylor, J. C.) 1346–1349 (1973).

43. *Sketch of relativistic heavy-ion collisions.* Accessed 6 July 2020. https://u.osu.edu/vishnu/2014/08/06/sketch-of-relativistic-heavy-ion-collisions/.

44. Abachi, S. *et al.* Observation of the top quark. *Phys. Rev. Lett.* **74,** 2632–2637. arXiv: hep-ex/9503003 (1995).

45. Aprahamian, A. *et al.* Reaching for the horizon: The 2015 long range plan for nuclear science (Oct. 2015).

46. Bazavov, A. *et al.* The chiral and deconfinement aspects of the QCD transition. *Phys. Rev. D* **85,** 054503. arXiv: 1111.1710 [hep-lat] (2012).

47. Troyer, M. & Wiese, U.-J. Computational complexity and fundamental limitations to fermionic quantum Monte Carlo simulations. *Phys. Rev. Lett.* **94,** 170201. arXiv: cond-mat/0408370 (2005).

48. Allton, C. R. *et al.* The QCD thermal phase transition in the presence of a small chemical potential. *Phys. Rev. D* **66,** 074507. arXiv: hep-lat/0204010 (2002).

49. De Forcrand, P. & Philipsen, O. The QCD phase diagram for small densities from imaginary chemical potential. *Nucl. Phys. B* **642,** 290–306. arXiv: hep-lat/0205016 (2002).

50. Borsanyi, S. *et al.* Full result for the QCD equation of state with 2+1 flavors. *Phys. Lett. B* **730,** 99–104. arXiv: 1309.5258 [hep-lat] (2014).

51. Bazavov, A. *et al.* Equation of state in (2+1)-flavor QCD. *Phys. Rev. D* **90,** 094503. arXiv: 1407.6387 [hep-lat] (2014).

52. Ratti, C. Lattice QCD and heavy ion collisions: a review of recent progress. *Rept. Prog. Phys.* **81,** 084301. arXiv: 1804.07810 [hep-lat] (2018).

53. Kurkela, A., Fraga, E. S., Schaffner-Bielich, J. & Vuorinen, A. Constraining neutron star matter with Quantum Chromodynamics. *Astrophys. J.* **789,** 127. arXiv: 1402.6618 [astro-ph.HE] (2014).

54. Bauswein, A. *et al.* Identifying a first-order phase transition in neutron star mergers through gravitational waves. *Phys. Rev. Lett.* **122,** 061102. arXiv: 1809.01116 [astro-ph.HE] (2019).

55. Stephanov, M. A., Rajagopal, K. & Shuryak, E. V. Signatures of the tricritical point in QCD. *Phys. Rev. Lett.* **81,** 4816–4819. arXiv: hep-ph/9806219 (1998).

56. Florkowski, W. *Phenomenology of Ultra-Relativistic Heavy-Ion Collisions* ISBN: 978-981-4280-66-2 (Mar. 2010).

57. Alver, B. *et al.* Phobos results on charged particle multiplicity and pseudorapidity distributions in Au+Au, Cu+Cu, d+Au, and p+p collisions at ultra-relativistic energies. *Phys. Rev. C* **83,** 024913. arXiv: 1011.1940 [nucl-ex] (2011).

58. Adamczyk, L. *et al.* Bulk Properties of the Medium Produced in Relativistic Heavy-Ion Collisions from the Beam Energy Scan Program. *Phys. Rev. C* **96,** 044904. arXiv: 1701.07065 [nucl-ex] (2017).

59. Abelev, B. I. *et al.* Systematic Measurements of Identified Particle Spectra in pp, d^+ Au and Au+Au Collisions from STAR. *Phys. Rev. C* **79,** 034909. arXiv: 0808.2041 [nucl-ex] (2009).

60. Adams, J. *et al.* Identified particle distributions in pp and Au+Au collisions at s(NN)**(1/2) = 200 GeV. *Phys. Rev. Lett.* **92,** 112301. arXiv: nucl-ex/0310004 (2004).

61. Adler, C. *et al.* Kaon production and kaon to pion ratio in Au+Au collisions at s(NN)**1/2 = 130-GeV. *Phys. Lett. B* **595,** 143–150. arXiv: nucl-ex/0206008 (2004).

62. Adler, C. *et al.* Measurement of inclusive anti-protons from Au+Au collisions at (s(NN))**(1/2) = 130-GeV. *Phys. Rev. Lett.* **87,** 262302. arXiv: nucl-ex/0110009 (2001).

63. Ollitrault, J.-Y. Anisotropy as a signature of transverse collective flow. *Phys. Rev. D* **46,** 229–245 (1992).

64. Rapp, R. & van Hees, H. Heavy Quark Diffusion as a Probe of the Quark-Gluon Plasma. arXiv: 0803.0901 [hep-ph] (Mar. 2008).

65. Abelev, B. I. *et al.* System-size independence of directed flow at the Relativistic Heavy-Ion Collider. *Phys. Rev. Lett.* **101,** 252301. arXiv: 0807.1518 [nucl-ex] (2008).

66. Adler, C. *et al.* Elliptic flow from two and four particle correlations in Au+Au collisions at s(NN)**(1/2) = 130-GeV. *Phys. Rev. C* **66,** 034904. arXiv: nucl-ex/0206001 (2002).

67. Alver, B. & Roland, G. Collision geometry fluctuations and triangular flow in heavy-ion collisions. *Phys. Rev. C* **81.** [Erratum: Phys.Rev.C 82, 039903 (2010)], 054905. arXiv: 1003.0194 [nucl-th] (2010).

68. Niemi, H., Denicol, G. S., Holopainen, H. & Huovinen, P. Event-by-event distributions of azimuthal asymmetries in ultrarelativistic heavy-ion collisions. *Phys. Rev. C* **87,** 054901. arXiv: 1212.1008 [nucl-th] (2013).

69. Poskanzer, A. M. & Voloshin, S. Methods for analyzing anisotropic flow in relativistic nuclear collisions. *Phys. Rev. C* **58,** 1671–1678. arXiv: nucl-ex/9805001 (1998).

70. Danielewicz, P. & Odyniec, G. Transverse Momentum Analysis of Collective Motion in Relativistic Nuclear Collisions. *Phys. Lett. B* **157,** 146–150. arXiv: 2109.05308 [nucl-th] (1985).

71. Bilandzic, A., Snellings, R. & Voloshin, S. Flow analysis with cumulants: Direct calculations. *Phys. Rev. C* **83,** 044913. arXiv: 1010.0233 [nucl-ex] (2011).

72. Borghini, N., Dinh, P. M. & Ollitrault, J.-Y. A New method for measuring azimuthal distributions in nucleus-nucleus collisions. *Phys. Rev. C* **63,** 054906. arXiv: nucl-th/0007063 (2001).

73. Adamczyk, L. *et al.* Inclusive charged hadron elliptic flow in Au + Au collisions at $\sqrt{s_{NN}}$ = 7.7 - 39 GeV. *Phys. Rev. C* **86,** 054908. arXiv: 1206.5528 [nucl-ex] (2012).

74. Hanbury Brown, R. & Twiss, R. Q. A New type of interferometer for use in radio astronomy. *Phil. Mag. Ser. 7* **45,** 663–682 (1954).

75. Hanbury Brown, R. & Twiss, R. Q. A Test of a new type of stellar interferometer on Sirius. *Nature* **178,** 1046–1048 (1956).

76. Wu, X.-Y., Pang, L.-G., Qin, G.-Y. & Wang, X.-N. Longitudinal fluctuations and decorrelations of anisotropic flows at energies available at the CERN Large Hadron Collider and at the BNL Relativistic Heavy Ion Collider. *Phys. Rev. C* **98,** 024913. arXiv: 1805.03762 [nucl-th] (2018).

77. Khachatryan, V. *et al.* Evidence for transverse momentum and pseudorapidity dependent event plane fluctuations in PbPb and pPb collisions. *Phys. Rev. C* **92,** 034911. arXiv: 1503.01692 [nucl-ex] (2015).

78. Jia, J. & Huo, P. A method for studying the rapidity fluctuation and decorrelation of harmonic flow in heavy-ion collisions. *Phys. Rev. C* **90,** 034905. arXiv: 1402.6680 [nucl-th] (2014).

79. Aaboud, M. *et al.* Measurement of longitudinal flow decorrelations in Pb+Pb collisions at $\sqrt{s_{\mathrm{NN}}} = 2.76$ and 5.02 TeV with the ATLAS detector. *Eur. Phys. J. C* **78,** 142. arXiv: 1709.02301 [nucl-ex] (2018).

80. Aad, G. *et al.* Longitudinal Flow Decorrelations in Xe+Xe Collisions at $\sqrt{s_{\mathrm{NN}}} = 5.44$ TeV with the ATLAS Detector. *Phys. Rev. Lett.* **126,** 122301. arXiv: 2001.04201 [nucl-ex] (2021).

81. Nie, M. Energy dependence of longitudinal flow decorrelation from STAR. *Nucl. Phys. A* **1005** (eds Liu, F., Wang, E., Wang, X.-N., Xu, N. & Zhang, B.-W.) 121783. arXiv: 2005.03252 [nucl-ex] (2021).

82. Nie, M. Measurement of longitudinal decorrelation of anisotropic flow V 2 and V 3 in 200 GeV Au+Au collisions at STAR. *Nucl. Phys. A* **982** (eds Antinori, F. *et al.*) 403–406 (2019).

83. Fermi, E. High-energy nuclear events. *Prog. Theor. Phys.* **5,** 570–583 (1950).

84. Fermi, E. Angular Distribution of the Pions Produced in High Energy Nuclear Collisions. *Phys. Rev.* **81,** 683–687 (1951).

85. Muller, I. Zum Paradoxon der Warmeleitungstheorie. *Z. Phys.* **198,** 329–344 (1967).

86. Israel, W. Nonstationary irreversible thermodynamics: A Causal relativistic theory. *Annals Phys.* **100,** 310–331 (1976).

87. Israel, W. & Stewart, J. Transient relativistic thermodynamics and kinetic theory. *Annals Phys.* **118,** 341–372 (1979).

88. Heinz, U. W., Song, H. & Chaudhuri, A. K. Dissipative hydrodynamics for viscous relativistic fluids. *Phys. Rev. C* **73,** 034904. arXiv: nucl-th/0510014 (2006).

89. Kovtun, P., Son, D. T. & Starinets, A. O. Viscosity in strongly interacting quantum field theories from black hole physics. *Phys. Rev. Lett.* **94,** 111601. arXiv: hep-th/0405231 (2005).

90. Schäfer, T. & Teaney, D. Nearly Perfect Fluidity: From Cold Atomic Gases to Hot Quark Gluon Plasmas. *Rept. Prog. Phys.* **72,** 126001. arXiv: 0904.3107 [hep-ph] (2009).

91. Bernhard, J. E., Moreland, J. S., Bass, S. A., Liu, J. & Heinz, U. Applying Bayesian parameter estimation to relativistic heavy-ion collisions: simultaneous characterization of the initial state and quark-gluon plasma medium. *Phys. Rev. C* **94,** 024907. arXiv: 1605.03954 [nucl-th] (2016).

92. Everett, D. *et al.* Phenomenological constraints on the transport properties of QCD matter with data-driven model averaging. *Phys. Rev. Lett.* **126,** 242301. arXiv: 2010.03928 [hep-ph] (2021).

93. Shen, C. & Heinz, U. The road to precision: Extraction of the specific shear viscosity of the quark-gluon plasma. *Nucl. Phys. News* **25,** 6–11. arXiv: 1507.01558 [nucl-th] (2015).

94. Kolb, P. F., Sollfrank, J. & Heinz, U. W. Anisotropic transverse flow and the quark hadron phase transition. *Phys. Rev. C* **62,** 054909. arXiv: hep-ph/0006129 (2000).

95. Rischke, D. H., Bernard, S. & Maruhn, J. A. Relativistic hydrodynamics for heavy ion collisions. 1. General aspects and expansion into vacuum. *Nucl. Phys. A* **595,** 346–382. arXiv: nucl-th/9504018 (1995).

96. Rischke, D. H., Pursun, Y. & Maruhn, J. A. Relativistic hydrodynamics for heavy ion collisions. 2. Compression of nuclear matter and the phase transition to the quark - gluon plasma. *Nucl. Phys. A* **595.** [Erratum: Nucl.Phys.A 596, 717–717 (1996)], 383–408. arXiv: nucl-th/9504021 (1995).

97. Hirano, T. Is early thermalization achieved only near mid-rapidity at RHIC? *Phys. Rev. C* **65,** 011901. arXiv: nucl-th/0108004 (2002).

98. Hirano, T., Tsuda, K. & Kajimoto, K. Hydrodynamic analysis of noncentral Pb + Pb collisions at 158-A-GeV. arXiv: nucl-th/0011087 (Nov. 2000).

99. Nonaka, C., Honda, E. & Muroya, S. (3+1)-dimensional relativistic hydrodynamical expansion of hot and dense matter in ultrarelativistic nuclear collision. *Eur. Phys. J. C* **17,** 663–673. arXiv: hep-ph/0007187 (2000).

100. Drescher, H., Ostapchenko, S., Pierog, T. & Werner, K. Initial condition for QGP evolution from NEXUS. *Phys. Rev. C* **65,** 054902. arXiv: hep-ph/0011219 (2002).

101. Ivanov, Y., Russkikh, V. & Toneev, V. Relativistic heavy-ion collisions within 3-fluid hydrodynamics: Hadronic scenario. *Phys. Rev. C* **73,** 044904. arXiv: nucl-th/0503088 (2006).

102. Schenke, B., Jeon, S. & Gale, C. Elliptic and triangular flow in event-by-event (3+1)D viscous hydrodynamics. *Phys. Rev. Lett.* **106,** 042301. arXiv: 1009.3244 [hep-ph] (2011).

103. Baier, R., Romatschke, P. & Wiedemann, U. A. Dissipative hydrodynamics and heavy ion collisions. *Phys. Rev. C* **73,** 064903. arXiv: hep-ph/0602249 (2006).

104. Song, H. & Heinz, U. W. Causal viscous hydrodynamics in 2+1 dimensions for relativistic heavy-ion collisions. *Phys. Rev. C* **77,** 064901. arXiv: 0712.3715 [nucl-th] (2008).

105. Lin, Z.-W., Ko, C. M., Li, B.-A., Zhang, B. & Pal, S. A Multi-phase transport model for relativistic heavy ion collisions. *Phys. Rev. C* **72,** 064901. arXiv: nucl-th/0411110 (2005).

106. Aguiar, C., Kodama, T., Osada, T. & Hama, Y. Smoothed particle hydrodynamics for relativistic heavy ion collisions. *J. Phys. G* **27,** 75–94. arXiv: hep-ph/0006239 (2001).

107. Cooper, F. & Frye, G. Comment on the Single Particle Distribution in the Hydrodynamic and Statistical Thermodynamic Models of Multiparticle Production. *Phys. Rev. D* **10,** 186 (1974).

108. Bass, S. *et al.* Microscopic models for ultrarelativistic heavy ion collisions. *Prog. Part. Nucl. Phys.* **41,** 255–369. arXiv: nucl-th/9803035 (1998).

109. Bleicher, M. *et al.* Relativistic hadron hadron collisions in the ultrarelativistic quantum molecular dynamics model. *J. Phys. G* **25,** 1859–1896. arXiv: hep-ph/9909407 (1999).

110. Karpenko, I., Huovinen, P. & Bleicher, M. A 3+1 dimensional viscous hydrodynamic code for relativistic heavy ion collisions. *Comput. Phys. Commun.* **185,** 3016–3027. arXiv: 1312.4160 [nucl-th] (2014).

111. Broniowski, W., Rybczynski, M. & Bozek, P. GLISSANDO: Glauber initial-state simulation and more.. *Comput. Phys. Commun.* **180,** 69–83. arXiv: 0710.5731 [nucl-th] (2009).

112. Chojnacki, M., Kisiel, A., Florkowski, W. & Broniowski, W. THERMINATOR 2: THERMal heavy IoN generATOR 2. *Comput. Phys. Commun.* **183,** 746–773. arXiv: 1102.0273 [nucl-th] (2012).

113. Akkelin, S., Hama, Y., Karpenko, I. & Sinyukov, Y. Hydro-kinetic approach to relativistic heavy ion collisions. *Phys. Rev. C* **78,** 034906. arXiv: 0804.4104 [nucl-th] (2008).

114. Karpenko, I. & Sinyukov, Y. Energy dependence of pion interferometry scales in ultra-relativistic heavy ion collisions. *Phys. Lett. B* **688,** 50–54. arXiv: 0912.3457 [nucl-th] (2010).

115. Sjostrand, T., Mrenna, S. & Skands, P. Z. PYTHIA 6.4 Physics and Manual. *JHEP* **05,** 026. arXiv: hep-ph/0603175 (2006).

116. Rybczynski, M., Stefanek, G., Broniowski, W. & Bozek, P. GLISSANDO 2 : GLauber Initial-State Simulation AND mOre..., ver. 2. *Comput. Phys. Commun.* **185,** 1759–1772. arXiv: 1310.5475 [nucl-th] (2014).

117. Glauber, R. J. *High Energy Collision Theory* in *Lectures in Theoretical Physics* (eds Brittin, W. E. & Dunham, L. G.) **1** (1959), 315.

118. Dudek, J. *et al.* Parameters of the deformed Woods-Saxon potential outside A=110-210 nuclei. *J. Phys. G* **5,** 1359–1381 (1979).

119. Moller, P., Nix, J. R., Myers, W. D. & Swiatecki, W. J. Nuclear ground state masses and deformations. *Atom. Data Nucl. Data Tabl.* **59,** 185–381. arXiv: nucl-th/9308022 (1995).

120. Bozek, P. & Broniowski, W. Transverse-momentum fluctuations in relativistic heavy-ion collisions from event-by-event viscous hydrodynamics. *Phys. Rev. C* **85,** 044910. arXiv: 1203.1810 [nucl-th] (2012).

121. Bożek, P., Broniowski, W. & Olszewski, A. Hydrodynamic modeling of pseudorapidity flow correlations in relativistic heavy-ion collisions and the torque effect. *Phys. Rev. C* **91,** 054912. arXiv: 1503.07425 [nucl-th] (2015).

122. Moreland, J. S., Bernhard, J. E. & Bass, S. A. Alternative ansatz to wounded nucleon and binary collision scaling in high-energy nuclear collisions. *Phys. Rev. C* **92,** 011901. arXiv: 1412.4708 [nucl-th] (2015).

123. Schenke, B., Tribedy, P. & Venugopalan, R. Fluctuating Glasma initial conditions and flow in heavy ion collisions. *Phys. Rev. Lett.* **108,** 252301. arXiv: 1202.6646 [nucl-th] (2012).

124. Steinheimer, J., Schramm, S. & Stocker, H. An Effective chiral Hadron-Quark Equation of State. *J. Phys. G* **38,** 035001. arXiv: 1009.5239 [hep-ph] (2011).

125. Huovinen, P. & Petersen, H. Particlization in hybrid models. *Eur. Phys. J. A* **48,** 171. arXiv: 1206.3371 [nucl-th] (2012).

126. Appelshauser, H. *et al.* Baryon stopping and charged particle distributions in central Pb + Pb collisions at 158-GeV per nucleon. *Phys. Rev. Lett.* **82,** 2471–2475. arXiv: nucl-ex/9810014 (1999).

127. Arsene, I. C. *et al.* Nuclear stopping and rapidity loss in Au+Au collisions at s(NN)**(1/2) = 62.4-GeV. *Phys. Lett. B* **677,** 267–271. arXiv: 0901.0872 [nucl-ex] (2009).

128. Adamczyk, L. *et al.* Third Harmonic Flow of Charged Particles in Au+Au Collisions at sqrtsNN = 200 GeV. *Phys. Rev. C* **88,** 014904. arXiv: 1301.2187 [nucl-ex] (2013).

129. Adamczyk, L. *et al.* Harmonic decomposition of three-particle azimuthal correlations at energies available at the BNL Relativistic Heavy Ion Collider. *Phys. Rev. C* **98,** 034918. arXiv: 1701.06496 [nucl-ex] (2018).

130. Petersen, H., Bhattacharya, V., Bass, S. A. & Greiner, C. Longitudinal correlation of the triangular flow event plane in a hybrid approach with hadron and parton cascade initial conditions. *Phys. Rev. C* **84,** 054908. arXiv: 1105.0340 [nucl-th] (2011).

131. Pang, L., Wang, Q. & Wang, X.-N. Effects of initial flow velocity fluctuation in event-by-event (3+1)D hydrodynamics. *Phys. Rev. C* **86,** 024911. arXiv: 1205.5019 [nucl-th] (2012).

132. Adil, A., Gyulassy, M. & Hirano, T. 3D jet tomography of the twisted color glass condensate. *Phys. Rev. D* **73,** 074006. arXiv: nucl-th/0509064 (2006).

133. Adil, A. & Gyulassy, M. 3D jet tomography of twisted strongly coupled quark gluon plasmas. *Phys. Rev. C* **72,** 034907. arXiv: nucl-th/0505004 (2005).

134. Bozek, P., Broniowski, W. & Moreira, J. Torqued fireballs in relativistic heavy-ion collisions. *Phys. Rev. C* **83,** 034911. arXiv: 1011.3354 [nucl-th] (2011).

135. Pang, L.-G., Qin, G.-Y., Roy, V., Wang, X.-N. & Ma, G.-L. Longitudinal decorrelation of anisotropic flows in heavy-ion collisions at the CERN Large Hadron Collider. *Phys. Rev. C* **91,** 044904. arXiv: 1410.8690 [nucl-th] (2015).

136. Pang, L.-G., Petersen, H., Qin, G.-Y., Roy, V. & Wang, X.-N. Decorrelation of anisotropic flow along the longitudinal direction. *Eur. Phys. J. A* **52,** 97. arXiv: 1511.04131 [nucl-th] (2016).

137. Bozek, P. & Broniowski, W. The torque effect and fluctuations of entropy deposition in rapidity in ultra-relativistic nuclear collisions. *Phys. Lett. B* **752,** 206–211. arXiv: 1506.02817 [nucl-th] (2016).

138. Chatterjee, S. & Bozek, P. Pseudorapidity profile of transverse momentum fluctuations in heavy ion collisions. *Phys. Rev. C* **96,** 014906. arXiv: 1704.02777 [nucl-th] (2017).

139. Bozek, P. & Broniowski, W. Longitudinal decorrelation measures of flow magnitude and event-plane angles in ultrarelativistic nuclear collisions. *Phys. Rev. C* **97,** 034913. arXiv: 1711.03325 [nucl-th] (2018).

140. He, Y. & Lin, Z.-W. Particle productions and anisotropic flows from the AMPT model for Cu+Au collisions at $\sqrt{s_{NN}} = 200$ GeV. *Eur. Phys. J. A* **56,** 123. arXiv: 2004.06385 [hep-ph] (2020).

141. Xu, Z. *et al.* Flow-plane decorrelations in heavy-ion collisions with multiple-plane cumulants. *Phys. Rev. C* **105,** 024902. arXiv: 2012.06689 [nucl-ex] (2022).

142. Back, B. B. *et al.* Centrality and pseudorapidity dependence of elliptic flow for charged hadrons in Au+Au collisions at s(NN)**(1/2) = 200-GeV. *Phys. Rev. C* **72,** 051901. arXiv: nucl-ex/0407012 (2005).

143. Abelev, B. I. *et al.* Centrality dependence of charged hadron and strange hadron elliptic flow from s(NN)**(1/2) = 200-GeV Au + Au collisions. *Phys. Rev. C* **77,** 054901. arXiv: 0801.3466 [nucl-ex] (2008).

144. Brodsky, S. J., Fleuret, F., Hadjidakis, C. & Lansberg, J. P. Physics Opportunities of a Fixed-Target Experiment using the LHC Beams. *Phys. Rept.* **522,** 239–255. arXiv: 1202.6585 [hep-ph] (2013).

145. Massacrier, L. *et al.* Feasibility studies for quarkonium production at a fixed-target experiment using the LHC proton and lead beams (AFTER@LHC). *Adv. High Energy Phys.* **2015,** 986348. arXiv: 1504.05145 [hep-ex] (2015).

146. Hadjidakis, C. *et al.* A fixed-target programme at the LHC: Physics case and projected performances for heavy-ion, hadron, spin and astroparticle studies. *Phys. Rept.* **911,** 1–83. arXiv: 1807.00603 [hep-ex] (2021).

147. Aggarwal, M. *et al.* An Experimental Exploration of the QCD Phase Diagram: The Search for the Critical Point and the Onset of De-confinement. arXiv: 1007.2613 [nucl-ex] (July 2010).

148. Studying the Phase Diagram of QCD Matter at RHIC. *Star Note* **0598** (2014).

149. Abgrall, N. *et al.* NA61/SHINE facility at the CERN SPS: beams and detector system. *JINST* **9,** P06005. arXiv: 1401.4699 [physics.ins-det] (2014).

150. Kekelidze, V. NICA project at JINR: status and prospects. *JINST* **12** (ed Shekhtman, L.) C06012 (2017).

151. Senger, P. Status of the Compressed Baryonic Matter experiment at FAIR. *Int. J. Mod. Phys. E* **29,** 2030001. arXiv: 2004.11762 [physics.ins-det] (2020).

152. Sakaguchi, T. High density matter physics at J-PARC-HI. *PoS* **CORFU2018** (eds Anagnostopoulos, K. *et al.*) 189. arXiv: 1904.12821 [nucl-ex] (2019).

153. Werner, K. Core-corona separation in ultra-relativistic heavy ion collisions. *Phys. Rev. Lett.* **98,** 152301. arXiv: 0704.1270 [nucl-th] (2007).

154. Mishustin, I., Russkikh, V. & Satarov, L. Ultrarelativistic Heavy Ion Collisions Within Two Fluid Model With Pion Emission. *Nucl. Phys. A* **494,** 595–619 (1989).

155. Katscher, U. *et al.* The Three-dimensional (2+1) fluid model for relativistic nuclear collisions. *Z. Phys. A* **346,** 209–216 (1993).

156. Ivanov, Y. & Soldatov, A. What can we learn from the directed flow in heavy-ion collisions at BES RHIC energies? *Eur. Phys. J. A* **52,** 10. arXiv: 1601.03902 [nucl-th] (2016).

157. Ivanov, Y. B. & Soldatov, A. A. Elliptic Flow in Heavy-Ion Collisions at Energies $\sqrt{s_{NN}} = 2.7$-39 GeV. *Phys. Rev. C* **91,** 024914. arXiv: 1401.2265 [nucl-th] (2015).

158. Ivanov, Y. B. & Soldatov, A. Bulk Properties of the Matter Produced at Energies of the Beam Energy Scan Program. *Phys. Rev. C* **97,** 024908. arXiv: 1801.01764 [nucl-th] (2018).

159. Kozhevnikova, M., Ivanov, Y. B., Karpenko, I., Blaschke, D. & Rogachevsky, O. Update of the Three-fluid Hydrodynamics-based Event Simulator: light-nuclei production in heavy-ion collisions. *Phys. Rev. C* **103,** 044905. arXiv: 2012.11438 [nucl-th] (2021).

160. Woods, R. D. & Saxon, D. S. Diffuse Surface Optical Model for Nucleon-Nuclei Scattering. *Phys. Rev.* **95,** 577–578 (1954).

161. Oliinychenko, D. & Petersen, H. Deviations of the Energy-Momentum Tensor from Equilibrium in the Initial State for Hydrodynamics from Transport Approaches. *Phys. Rev. C* **93,** 034905. arXiv: 1508.04378 [nucl-th] (2016).

162. Courant, R., Friedrichs, K. & Lewy, H. Über die partiellen Differenzengleichungen der mathematischen Physik. *Math. Ann.* **100,** 32–74 (1928).

163. Vogt, R. *Ultrarelativistic heavy-ion collisions* ISBN: 978-0-444-52196-5 (Elsevier, Amsterdam, 2007).

164. Borsanyi, S. *et al.* Calculation of the axion mass based on high-temperature lattice quantum chromodynamics. *Nature* **539,** 69–71. arXiv: 1606.07494 [hep-lat] (2016).

165. Parotto, P. *et al.* QCD equation of state matched to lattice data and exhibiting a critical point singularity. *Phys. Rev. C* **101,** 034901. arXiv: 1805.05249 [hep-ph] (2020).

166. Ma, H.-H. *et al.* A quasi-particle model with a phenomenological critical point. arXiv: 1804.06797 [nucl-th] (Apr. 2018).

167. Bannur, V. M. Comments on quasiparticle models of quark-gluon plasma. *Phys. Lett. B* **647,** 271–274. arXiv: hep-ph/0608232 (2007).

168. Rischke, D. H., Gorenstein, M. I., Stoecker, H. & Greiner, W. Excluded volume effect for the nuclear matter equation of state. *Z. Phys. C* **51,** 485–490 (1991).

169. Huovinen, P. & Petreczky, P. QCD Equation of State and Hadron Resonance Gas. *Nucl. Phys. A* **837,** 26–53. arXiv: 0912.2541 [hep-ph] (2010).

170. Vovchenko, V., Pasztor, A., Fodor, Z., Katz, S. D. & Stoecker, H. Repulsive baryonic interactions and lattice QCD observables at imaginary chemical potential. *Phys. Lett. B* **775,** 71–78. arXiv: 1708.02852 [hep-ph] (2017).

171. Schäfer, A., Karpenko, I. & Elfner, H. Conservation laws in a novel hybrid approach. *PoS* **CPOD2021,** 046. arXiv: 2109.08578 [hep-ph] (2022).

172. Tomášik, B. DRAGON: Monte Carlo generator of particle production from a fragmented fireball in ultrarelativistic nuclear collisions. *Comput. Phys. Commun.* **180,** 1642–1653. arXiv: 0806.4770 [nucl-th] (2009).

173. Tomášik, B. DRoplet and hAdron generator for nuclear collisions: An update. *Comput. Phys. Commun.* **207,** 545–546 (2016).

174. Retiere, F. & Lisa, M. A. Observable implications of geometrical and dynamical aspects of freeze out in heavy ion collisions. *Phys. Rev. C* **70,** 044907. arXiv: nucl-th/0312024 (2004).

175. Schäfer, A., Karpenko, I., Wu, X.-Y., Hammelmann, J. & Elfner, H. Particle production in a hybrid approach for a beam energy scan of Au+Au/Pb+Pb collisions between $\sqrt{s_{\mathrm{NN}}}$ = 4.3 GeV and $\sqrt{s_{\mathrm{NN}}}$ = 200.0 GeV. arXiv: 2112.08724 [hep-ph] (Dec. 2021).

176. Weil, J. *et al.* Particle production and equilibrium properties within a new hadron transport approach for heavy-ion collisions. *Phys. Rev. C* **94,** 054905. arXiv: 1606.06642 [nucl-th] (2016).

177. Adamczyk, L. *et al.* Elliptic flow of identified hadrons in Au+Au collisions at $\sqrt{s_{NN}} = 7.7$-62.4 GeV. *Phys. Rev. C* **88,** 014902. arXiv: 1301.2348 [nucl-ex] (2013).

178. Abelev, B. I. *et al.* Identified particle production, azimuthal anisotropy, and interferometry measurements in Au+Au collisions at s(NN)**(1/2) = 9.2-GeV. *Phys. Rev. C* **81,** 024911. arXiv: 0909.4131 [nucl-ex] (2010).

179. Kharzeev, D. & Nardi, M. Hadron production in nuclear collisions at RHIC and high density QCD. *Phys. Lett. B* **507,** 121–128. arXiv: nucl-th/0012025 (2001).

180. Loizides, C., Kamin, J. & d'Enterria, D. Improved Monte Carlo Glauber predictions at present and future nuclear colliders. *Phys. Rev. C* **97.** [Erratum: Phys.Rev.C 99, 019901 (2019)], 054910. arXiv: 1710.07098 [nucl-ex] (2018).

181. Gale, C., Jeon, S. & Schenke, B. Hydrodynamic Modeling of Heavy-Ion Collisions. *Int. J. Mod. Phys. A* **28,** 1340011. arXiv: 1301.5893 [nucl-th] (2013).

182. Oliinychenko, D. & Koch, V. Microcanonical Particlization with Local Conservation Laws. *Phys. Rev. Lett.* **123,** 182302. arXiv: 1902.09775 [hep-ph] (2019).